THEORETICAL AND SPECTROSCOPIC INVESTIGATIONS ON IONOGELS

Safna Hussan KP and Mohamed Shahin Thayyil

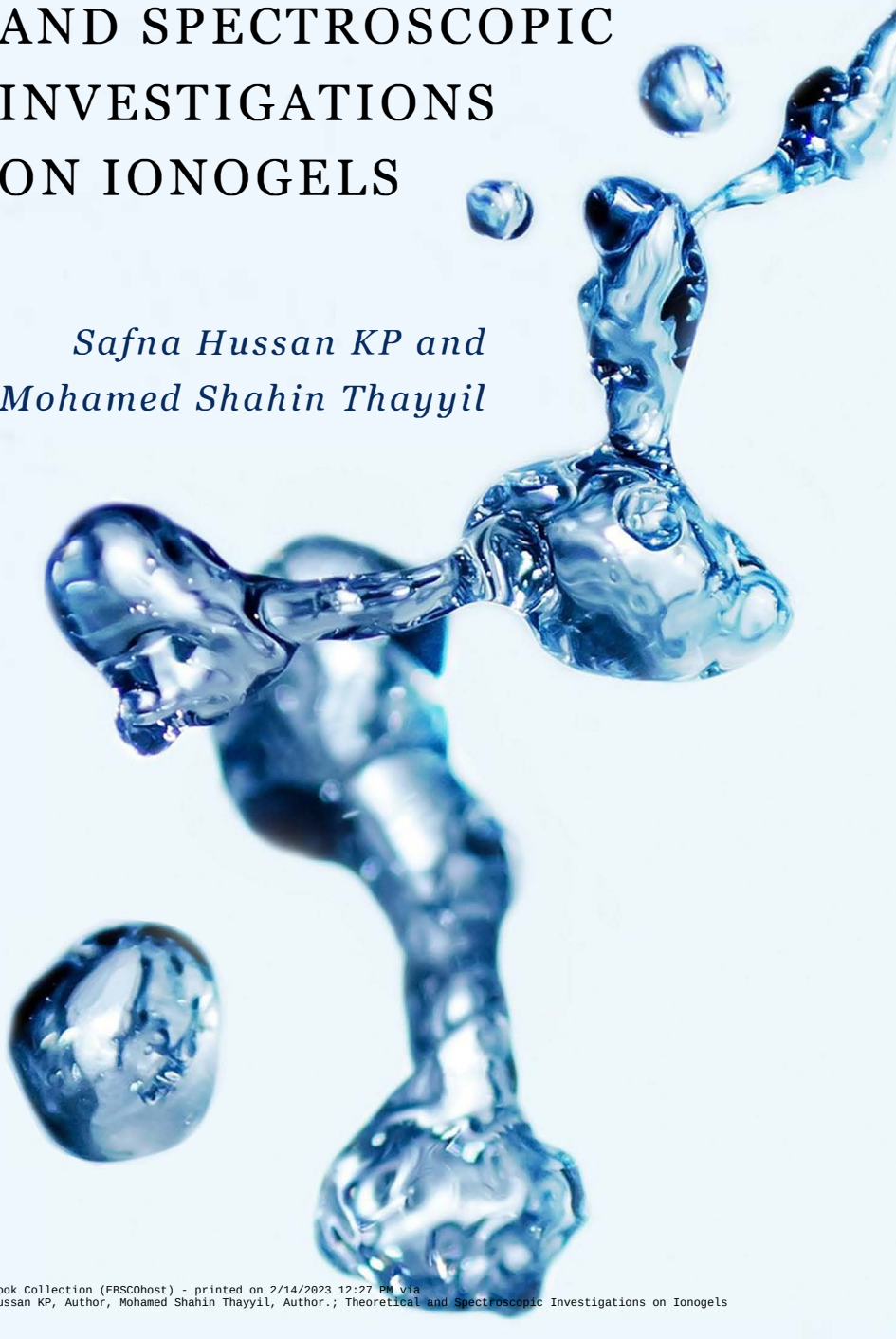

Theoretical and Spectroscopic Investigations on Ionogels

Theoretical and Spectroscopic Investigations on Ionogels

By

Safna Hussan KP

and Mohamed Shahin Thayyil

Cambridge Scholars Publishing

Theoretical and Spectroscopic Investigations on Ionogels

By Safna Hussan KP and Mohamed Shahin Thayyil

This book first published 2019

Cambridge Scholars Publishing

Lady Stephenson Library, Newcastle upon Tyne, NE6 2PA, UK

British Library Cataloguing in Publication Data
A catalogue record for this book is available from the British Library

ISBN (10): 1-5275-3745-5
ISBN (13): 978-1-5275-3745-3

CONTENTS

LIST OF FIGURES

LIST OF TABLES

ACKNOWLEDGMENTS

The research carried out by us on the subject from 2015 to 2019 would not have been possible without the support, encouragement, and association of many of our colleagues, collaborators, and well-wishers. We use this opportunity to express our heartfelt gratitude to them.

First and foremost, we would like to thank the God Almighty for His Blessing in making this endeavor a success. We bow our heads . . .

We are very thankful and indebted to our colleagues and friends in the Department of Physics, University of Calicut for the facilities provided to us and the good ambiance that allowed us to work to formulate this research problem and consistently work towards its successful completion.

We take this opportunity to extend our sincere gratitude to Dr. K. L. Ngai, Dipartimento di Fisica, Università di Pisa, Italy, who inspired us more than anyone and gave critical comments on formulating the problem, consistently providing valuable advice and comments whenever we needed that.

We gratefully acknowledge the research funding from UGC DAE Consortium, BARC, Mumbai, and our principal collaborator, Dr. S. K. Deshpande, who patiently helped us in the dielectric spectroscopic measurements and other research. We are very much thankful to Dr. Muraleedharan K., Department of Chemistry, UOC, and Miss. Vijisha K. Rajan introduced us to the world of computational chemistry. Mrs. Jinitha T. V, Department of Chemistry, UOC, and Dr. Jayant Kolte, Thapar University, need special mention for their support during the experiments. Stimulating discussions with Dr. S. S. N. Murthy (JNU India), Dr. S. Capaccioli (University of Pisa, Italy), Dr. G. Govindaraj (Pondicherry University, India), Dr. Raj Suryanarayan (Univ. of Minnesota, USA), Dr. Marian Paluch (University of Silesia, Poland), Dr. A. K. Bansal (NIPER Mohali, India) are kindly acknowledged.

We want to acknowledge all the teachers from whom we learned knowledge and skills since our childhoods. We would like to extend our gratitude to Dr. Sailaja U., Dr. K. K. Abdulla, Dr. P. A. Subha, et al. Support from our research team members Sulaiman M.K., Sahra Mohamed, Binesh M., A. Afsal, Shabeeba P., Nighilnath and Haroon who have willingly helped us out with their abilities. S.H. specially remembers her friends who have bestowed their love and support to her like Bini,

Arun Krishnan, Bindhu, Fasna, Soumya, Vinitha, Akhila, Soufeena P. P. Akhila A. K. Salma, Hajara, Anu Antony, Ansi, Anupama, Benjamin Hudson Baby, Prakashan, Vintu, Anna S. Kennadi, Dr. Sangeetha, Dr. Shaniba, Dr. Subair. . . .

Finally, any fruitful endeavor would not be complete without the support and encouragement of family and friends, and the authors find this opportunity to acknowledge with a big salute their love, affection, and endurance. S.H. especially takes this occasion to thank her loving husband, Bujair Ahammed V. M., for his patience, support, and willingness to develop her to the fullest of potentials in all ways, her daughter, parents, and in-laws, and other dears and nears.

Safna Hussan K.P.
Dr. Mohamed Shahin Thayyil

PREFACE

Ionic liquids (ILs) are salts with a melting point below 250°C; they have been attracting electrochemists with their unique properties like non-volatility, thermal stability, non-flammability, and low vapor pressure with wide electrochemical window. ILs have emerged as a potential replacement for organic electrolytes. However, the liquid nature of ILs limits their application due to leakage. Thus there is incredible demand for the immobilization of ILs since it overcomes all the restrictions and opens up a new pathway to solid electronic gadgets like batteries, capacitors, super capacitors, fuel cells, sensors, etc. Among all the well-known strategies, entrapping ILs in the polymer matrix can be considered as a feasible, low-cost method for large scale production of ionogels. Ionogel consists of a non-conducting polymeric framework as the host and a conducting IL as the guest. Ionogel not only retains the properties of ILs but also shows the mechanical properties of a polymer matrix like flexibility, film-forming nature, etc. Thus ionogel will be a better choice for solid state electrolytes due to its appealing features of freestanding film and high thermal stability properties that allows us to design easily and cheaply with modularity and reliability in electrochemical devices. The versatility of both ILs and polymer chemistry allows us to develop an infinite number of ionogels. Every combination of ILs and polymer results in unpredictable behavior. Thus the field of ionogel membranes has yet to be explored.

This book is intended to report a complete characterization technique from theoretical prediction to the application level, including quantum mechanical predictions, synthesis method, characterization techniques, and molecular dynamics of the developed ionogel. This book will be useful for students, researchers, industrialists, etc., and whoever wishes to work in the field of ionogels, as well as in the application level of solid-state materials. As we said above, the field of ionogel membranes is yet to be explored, and this book can be used as reference material for upcoming innovations too.

This book covers ionogel membranes and their development, theoretical predictions, characterization, detailed thermal and electrical properties, molecular dynamics, and applications. It is written as a distinctive source taking the reader on a fantastic journey from quantum

mechanical calculations to advanced research areas. Chapter 1 gives detailed information about ionic liquids and ionogel membranes and their preparations. The solution casting on glass technique was employed to develop ionogel by entrapping two highly conducting ILs, namely, 1-Ethyl-3-methyl imidazolium thiocyanate [EMIM] [SCN] and 1-Butyl-1-methyl pyrrolidinium bis (trifluoromethyl sulfonyl imide) [BMPyr] [TFSI], in two non-conducting polymers. Chapter 2 introduces a novel hybrid theoretical approach named ONIOM (n-layered integrated molecular orbital and molecular mechanics approach), which was implemented in the Gaussian 09 program package to study the interaction of ILs with complex polymer chains and subsequently to check the compatibility of the IL with two non-conducting polymers, namely polymethyl methacrylate and polyvinyl pyrrolidone matrix, to form an eco-friendly ionogel. This quantum mechanical approach helped us trace the most compatible pairs of ILs and polymer matrices among the chosen four combinations. Chapter 3 presents a detailed morphological characterization of ionogel membranes by means of the scanning electron microscope, Fourier transforms infrared spectroscopy, Fourier transforms Raman spectroscopy, and an X-ray diffractometer.

Chapter 4 delineates the influence of ILs in the polymer matrices and discusses the variations in phase transitions and thermal stability of the polymer matrices. Chapters 5 and 6 address the molecular dynamics, charge transport mechanism, conductivity relaxation in the ionogel membranes over broad frequency window, and wide temperature range to explore the molecular fluctuations and variations that happened in the ionogel membranes on varying weight ratios of the incorporated ionic liquid.

Chapter 7 discusses the specific properties and applications of the two developed ionogel membranes. This chapter covers the energy storage application of ionogel membranes and also emphasizes the CO_2 sensing and capturing properties of the developed one.

In summary, this will be a remarkable contribution toward the state of the art for material designing and development, morphology, structure, thermal and electrical properties, and applications of ionogel membranes. We hope that this will be very useful for academic and industrial purposes but also for fledgling students and newcomers in the field of solid state devices.

Safna Hussan K. P.
Dr. Mohamed Shahin Thayyil

ABSTRACT

Nowadays, an enormous research effort has been devoted to immobilize ionic liquid for electrochemical applications, since it can be used as an excellent substitute for liquid electrolytes. Among all the well-known strategies, entrapping ILs in the polymer matrix can be considered as a feasible, low-cost method for large scale production of ionogel. The versatility of both IL and polymer chemistry allows us to develop an infinite number of ionogels. Every combination of IL and polymer results in unpredictable behavior; thus the field of ionogel membranes is yet to be explored. This book is intended to report complete characterization techniques from theoretical predictions to the application level, including quantum mechanical predictions, synthesis method, characterization techniques, and molecular dynamics of the developed ionogel.

Moreover, a novel hybrid theoretical approach named ●NI●M (n-layered integrated molecular orbital and molecular mechanics approach) was implemented to study the interaction of ILs with complex polymer chains in the ionogel. This book will be useful for students, researchers, industrialists, and so on, and for anyone who wishes to work in the field of ionogels as well as in the application level of solid-state materials. As we said above, the field of ionogel membranes is yet to be explored, and this book can be used as reference material for upcoming innovations too.

Safna Hussan K.P.
Dr. Mohamed Shahin Thayyil

AUTHOR BIOGRAPHIES

Safna Hussan K. P. is a doctoral research scholar at the University of Calicut, Department of Physics, working with Dr. Mohamed Shahin Thayyil with a UGC-MANF fellowship. She earned her bachelors and master's degrees in physics from University of Calicut, Kerala, India in 2010 and 2012, respectively. She is currently involved in the research area of ionic liquids with two potential applications, namely, electrochemical and pharmaceuticals. She develops ionogel membranes by immobilizing ionic liquids in the non-conducting polymer matrices and makes it viable for application in solid-state devices. She is an internationally renowned scholar with many publications in international peer-reviewed journals. Safna Hussan has many collaborations at national and international levels.

Mohamed Shahin Thayyil is an Assistant Professor at the Dept. of Physics, University of Calicut (CU), India. He holds a Master's in Physics (CU), a PhD in Physics (Jawaharlal Nehru University, New Delhi, India) and pursued a Post-Doctoral Research at the Dept. of Physics, University of Pisa, Italy. Apart from teaching, he is involved in active research on amorphous materials, amorphous pharmaceuticals, ionic liquids, electrochemical studies. He has published more than 50 research papers and acted as reviewer for different journals. He has spent time and effort in developing amorphous materials from their crystalline counterparts and in understanding the molecular dynamics of such a system in the glassy state as well as in a supercooled liquid state. He made his signature in the area of pharmaceuticals and is currently interested in solid state electrolytes. He is also a specialist in broadband dielectric spectroscopy and differential scanning calorimeter analysis for a broad range of materials. He has published around 45 papers and acted as editor for one book. He has supervised PhD and MPhil theses and has had many collaborations across the world.

ABBREVIATIONS USED IN THIS BOOK

IL	: Ionic liquid
[EMIM] [SCN]	: 1-Ethyl-3-methylimidazolium thiocyanate
[BMPyr] [TFSI]	: 1-Butyl-1-methyl pyrrolidinium bis (trifluoromethyl sulfonyl imide)
PMMA	: Polymethyl methacrylate
PVA	: Polyvinyl alcohol
$E_{stretch}$	: The energy associated with bond stretching
$E_{bending}$	: The energy associated with bond bending
$E_{tortion}$	: Torsional energy
$E_{bonding}$	: The energy associated with bonding interactions
$E_{nonbonding}$	: The energy associated with nonbonding interactions
$E_{covalent}$	: The energy associated with covalent bonding
$E_{noncovalent}$	: The energy associated with non-covalent bonding
MM	: Molecular mechanics
QM	: Quantum mechanics
ONIOM	: Our N-layered integrated molecular orbital+ molecular mechanics
Sdf	: Standard data file
$k_{stretch}$	: Proportionality constant
L	: Length
l_{eq}	: Equilibrium length
H	: Hamiltonian energy operator
ψ	: Eigen function
E	: Eigenvalue
SM	: Semi-empirical method
DFT	: Density functional theory
TDFT	: Time-dependent density functional theory
E_{NN}	: Nuclear-nuclear repulsion energy
E_v	: Nuclear-electron attraction energy
E_{coul}	: Classical electron-electron Coulomb repulsion energy
E_T	: Kinetic energy of electrons
E_{ach}	: The non-classical electron-electron exchange energies

E_{corr}	: The energy from the correlated movements of electrons with different spins
PES	: Potential energy surface
FMO	: Frontier molecular orbital
HOMO	: Highest occupied molecular orbital
LUMO	: With lowest unoccupied molecular orbital
UV	: Ultra violet
IR	: Infrared
H	: Enthalpy
S	: Entropy
G	: Gibbs free energy
FTIR	: Fourier transform infrared
ATR-FTIR	: Attenuated total reflectance-Fourier transform infrared
NLO	: Nonlinear optical
IP	: Ionisation potentials
EA	: Electron affinity
H	: Hardness
S	: Softness
M	: Chemical potential
Ω	: Electrophilicity index
P	: Polarization
F	: Electric Field
A	: Polarizability
B	: First static hyperpolarizability
SEM	: Scanning electron microscope
FT-Raman	: Fourier transform Raman spectroscopy
DSC	: Differential scanning calorimetry
TGA	: Thermal gravimetry analysis
DTGA	: First derivatives thermal gravimetry analysis
Tg	: Glass transition temperature
Tm	: Melting point
X_1	: mass (weight) fraction
BDS	: Broadband dielectric spectroscopy
Z	: Impedance
ε	: Permittivity
σ	: Conductivity
M	: Modulus
IP	: Interfacial polarization
MWS	: Maxwell-Wagner-Sillars
G	: Conductance

CPE	: Constant phase element
CPE-T	: Pseudocapacitance
SCLC	: Space charge limited conduction
CV	: Cyclic voltammetry
Ag	: Silver
C	: Capacitance
SPE	: Solid polymer electrolyte
CO_2	: Carbon dioxide

CHAPTER 1

INTRODUCTION

1.1. Introduction

Material design is an art that plays a vital role in our day-to-day needs. Designing a material is the primary phase of any product development where the architect must focus on improving the properties of a material to overcome their limitations or to impart superior qualities. Quality and performance of material are assessed according to their structural, electrical, thermal, mechanical, chemical, and optical properties and by analyzing a wide variety of materials to reveal that a single material is not fulfilling all aspects of our requirements. Thus, in order to make a product viable for practical application, incorporation of diverse properties is essential within a feasible cost. Thus, material selection and design are the prominent stages of research keeping in view their practical applications.

Ionic liquids (ILs) offer a wide variety of properties that make them a prominent substitute for conventional organic electrolytes in many energy-related application fronts. The freedom to choose different cation-anion combinations make them unique with diverse properties like low volatility coupled with high electrochemical and thermal stability; significant ionic conductivity crafts the likelihood of designing an ideal electrolyte for batteries, super-capacitors, actuators, dye-sensitized solar cells, and thermo-electrochemical cells, etc. (1). Thus, the biggest charm of ionic liquids relies on the possibility to tune their properties by choice of the anion-cation combination. Moreover, a large family of them are air and water stable, as well as thermally stable even at temperatures higher than 570 K (2). Though ILs are used successfully as electrolytes in many gadgets, their leakage-causing fluid nature and high cost limit their large scale application (3–5).

Currently, enormous research efforts have been devoted to immobilize ILs for electrochemical applications, since they can be cast as an excellent substitute for liquid electrolytes. Chemical attachment with suitable ionic species and physical entrapment of an IL in non-conducting organic/inorganic matrices are the two strategies popularly used for immobilizing ILs, which

are commonly named *ion-gels* or *ionogels*. Among them, polymers are an attractive platform considering their rich database and low cost for large scale production. The versatility of both ILs and polymer chemistry results in an infinite number of ionogels. Each combination of an IL with a polymer results in unpredictable behavior due to the possibility of diverse chemical bonding. Thus the field of ionogels is yet to be explored systematically.

This book is intended to report a complete overview of the development of ionogels to their application. It covers the characterization technique from theoretical predictions based on quantum mechanical calculations, structural and morphological studies, thermal behavior, molecular dynamics, and charge transport properties. Moreover, a novel hybrid theoretical approach named ONIOM (n-layered integrated molecular orbital and molecular mechanics approach) was introduced and implemented to study the interactions of ILs with complex polymer chains in the ionogels. It will be useful for readers, including students, researchers, and industrialists, who wish to explore the field of ionogels as well as their applications to solid-state materials. As we have said, the field of ionogel membranes is yet to be explored; this book can be used as reference material for upcoming innovations too.

1.2. Ionic liquids

Nowadays, ionic liquids (ILs) are considered as promising materials for electrochemical applications because of their unique characteristics compared with conventional molecular liquids (6). ILs are nothing but organic salts with either an asymmetric cation with a symmetric anion or vice versa or with both an asymmetric anion and cation. ILs are liquid at near room temperature with a shallow melting point precisely below 570 K (7) having negligible vapor pressure, non-flammability, and enhanced thermal and chemical stability. A most interesting feature of ILs is that they consist of ions with high ion density and conductivity.

Moreover, the physical and chemical properties of an IL can easily be tuned by introducing various kinds of ions in it. These unique properties of ILs have attracted worldwide attention for applying them in vast areas including green solvents, media for organic transformation, electrochemical applications, nanotechnology, biotechnology, pharmaceuticals, etc. These applications have already been reported in the literature, and hence we are more focused on their electrolytic applications alone.

Though electrodes play a vital role in electrochemical gadgets regarding their overall capacity, energy density, and cyclic-ability, electrolytes also

have a crucial role in determining the current density, power density, time stability, and safety of the battery in electrochemical devices (8). Henceforth, ILs open up a new platform to improve the ion conductivity of electrolytes. The favorable properties of IL like non-volatility, high ionic conductivity (0.1–740 mS/cm), high thermal stability, and wide electrochemical window made it suitable for an ideal electrolyte. Further, ILs opens up an avenue for improving the properties of conducting materials. Thus ILs act as an excellent substitute for the legendary organic and non-organic electrolytes in the gadgets. A list of such ionic liquid with their characteristic properties is tabulated in Table 2.

Table 2. List of commonly used ionic liquids for the electrochemical application (9).

Ionic liquids	Conductivity	Electrochemical window
a) Highly conductive		
1-Ethyl-3-methylimidazolium dicyanamide	27 mS/cm	2.9 V
1-Ethyl-3-methylimdazolium thiocyanate	21 mS/cm	2.3 V
b) Electrochemically stable		
Triethylsulphonium bis(trifluoromethylsulfonyl)imide	8.2 mS/cm	5.5 V
N-Methyl-*N*-trioctylammonium bis(trifluoro-methylsulfonyl)imide	2.2 mS/cm	5.7 V
N-Butyl-*N*-methylpyrrolidiniun bis(trifluoro-methylsulfonyl)imide	2.1 mS/cm	6.6 V
c) Combined properties		
1-Ethyl-3-methylimidazolium tetrafluoroborate	12 mS/cm	4.3 V
1-Ethyl-3-methylimidazolium trifluoromethylsulfonate	8.6 mS/cm	4.3 V

Generally, ILs with imidazolium cations exhibit higher conductivity while pyrrolidinium and sulphonium cations exhibit a wider electrochemical window. However, the liquid nature of ILs still limits their application as electrolytes in the current scenario, since safety had to be assured rather than their performance (10). A large number of works were already reported on the relevance of ILs and their effectiveness in electrochemistry. However, our main concern is devoted to overcoming the limitations of ILs owing to their liquid nature including leakage, gas formation from solvent decomposition, etc., and will not venture too much

to other areas. This work is solely concentrated on two ILs with high conductivity, namely: 1-Ethyl-3-methylimidazolium thiocyanate and 1-Butyl-1-methyl pyrrolidinium bis (trifluoromethyl sulfonyl imide).

1.2.1. 1-Ethyl, 3-methylimidazolium thiocyanate

1-Ethyl-3-methylimidazolium thiocyanate [EMIM] [SCN], with the formula $C_7H_{11}N_3S$, is a room temperature IL with a molecular weight of 169.25 g/mol extensively used as an electrolyte in energy storage devices. The chemical structure of [EMIM] [SCN] is shown in Figure 1.

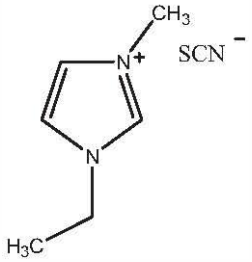

Figure 1. The chemical structure of 1-Ethyl-3-methylimidazolium thiocyanate.

[EMIM] [SCN] has a high conductivity of 2.1Sm ^{1} and low viscosity at room temperature compared to other ILs, e.g. [EMIm]BF_4, [BMIm]BF_4, and organic electrolytes (11). The literature emphasizes that though the ionic conductivity of [EMIM] [SCN] is about 1/40 of that for 35 wt% H_2SO_4 and about five times that for 0.1M (CF_3SO_2) 2NLi in PC: DME (1:2, v/v), the electrochemical performance of [EMIM] [SCN] lie between the two specified electrolytes. Due to high capacitance, uncompromised performance, and stability, [EMIM] [SCN] can be used as a potential electrolyte in capacitors, double layer capacitors, supercapacitor, dye-sensitized solar cells, etc.

1.2.2. 1-Butyl-1-methyl pyrrolidinium bis (trifluoromethyl sulfonyl imide)

1-Butyl-1-methyl pyrrolidinium bis (trifluoromethyl sulfonyl imide) [[BMPyr] [TFSI]] with the formula $C_{11}H_{20}F_6N_2O_4S_2$ is also a room-temperature ionic liquid with a molecular weight of 422.41 g/mol with high conductivity and viscosity. The chemical structure of [BMPyr] [TFSI] is shown in Figure 2.

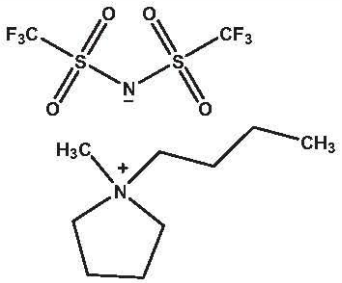

Figure 2. The chemical structure of 1-Butyl-1-methyl pyrrolidinium bis (trifluoromethyl sulfonyl imide).

[BMPyr] [TFSI] has a viscosity of 77.76 mPa.s at room temperature due to the presence of a considerable amount of hydrogen bonding initiated by long alkyl chains in the pyrrolidinium compared with other cations (12). Density (1.395 gcm^{-3}) and electrochemical window (5.67 V) are higher compared with other TFSI based ILs. As in the case of [BMPyr] [TFSI] immobilizing the IL is essential to assure safety for practical applications (13).

The easiest way for the preparation of an immobilized ionic liquid is the addition of a liquid to a solid support. Considering low cost and large-scale production of ionogels, the physical entrapment of IL in the non-conducting polymer matrix is considered to be the best method. The physically entrapped IL has specific commercial interest since it retains the properties of both—the guest IL and the host polymer matrix. Even though, non-conducting polymers are the best platform to immobilize ILs, only a few collections of polymers and ILs were explored until now. However, the versatility of polymer chemistry allows us to develop an infinite combination of ionogels (14). The compatibility and miscibility will declare whether the taken combination is a better choice. Every combination of guest and host in the ionogel has to expect unpredictable properties. Only a few combinations have been studied. Thus the field of ionogel membranes is yet to be explored.

1.3. Non-Conducting Polymers

The non-conducting polymer is an important platform to immobilize the ILs since polymer electrolytes were considered as a significant constituent of many electrochemical devices. Recently solid polymer electrolytes are conquering the electrochemical research due to their

intrinsic properties like thin-film-forming ability, transparency, flexibility, etc. Thus solid polymer electrolytes will fill some gaps in the search for new architectures for electrochemical devices, given that more and more devices use them, such as solid-state batteries, sensors, and portable electrochemical units (15). However, the significant drawbacks of the majority of polymer electrolytes are their low ionic conductivity, thermal instability, and brittle nature. In this regard, the best candidates for entrapping ILs are the polymer matrix, since any polymer that goes with an IL will form a better solution for solid electronic gadgets, as discussed by Hiroyuki Ohno (16), one of the most cited authors in this research field. The central non-conducting polymeric system chosen for this study are polymethyl methacrylate and polyvinyl alcohol.

1.3.1. Polymethyl methacrylate

PMMA is a promising polymer with inimitable properties including transparency, amorphocity, thermoplasticity, light weight, shatter resistance, weather resistance, and scratch resistance. Due to this versatility of its characteristics, PMMA had a wide area of interest in optical, pneumatic actuation, sensor, analytical separation, and conductive devices (3–7). Other applications include the use of PMMA in biomedical applications, polymer electrolytes, and drug delivery using electro-diffusion or electro-osmotic flow. PMMA was discovered in the early 1930s by British chemists Rowland Hill and John Crawford, followed by their first application by a German chemist, Otto Rohm, in 1934. The basic chemical structure of PMMA is shown in Figure 3.

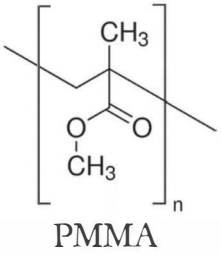

Figure 3. The basic chemical structure of polymethyl methacrylate.

The semi-crystalline nature of PMMA is due to the presence of the adjacent methyl group (CH_3), which prevents it from packing firmly in a crystalline fashion, and from rotating freely around the C-C bonds. The

amorphocity, lack of porosity, and increased mechanical strength make PMMA viable for the polymer electrolytic application. PMMA has to overcome the following limitations such as porosity, strength, and thermal stability of the electrolytes (17). Despite all the advantages of PMMA, the non-conducting behavior and lack of ions for transportation, thermal instability, and brittleness all limit their applications in the field of polymer electrolytes. Many researchers were widely focused on enhancing the conductivity, thermal stability, and fragility of PMMA. Flora et al. developed polymer membranes of poly (methyl methacrylate)/ poly (acrylonitrile)/ lithium perchlorate with different plasticizers such as ethylene carbonate and polycarbonate (EC and PC); the thermal stability and conductivity confirmed that the PAN/PMMA/$LiClO_4$-EC polymer electrolyte was found to be suitable for applications in lithium-ion batteries (17). Similarly, the entrapment of IL in PMMA may also be favorable to tune the properties of PMMA and PMMA will act as a compatible host for ILs (14, 18–22).

1.3.2. Polyvinyl alcohol

Polyvinyl alcohol (PVA) is a synthetic water-soluble odorless, nontoxic polymer with emulsifying and adhesive property (23). It is prepared either by polymerization of vinyl alcohol or by replacing acetyl groups with a hydroxyl group in polyvinyl acetates. It is an excellent film-forming polymer with high ductility and flexibility. It has diverse roles in commercial and industrial applications such as papermaking, textiles, and printing. Polyvinyl alcohol is found in ophthalmic solutions as a lubricant to prevent irritation or to relieve dryness of the eyes (24).

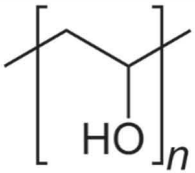

Figure 4. The basic chemical structure of polyvinyl alcohol.

PVA is a hydrophilic linear polymer which forms copolymers of vinyl alcohol and vinyl acetate. Hence, the structural properties of polyvinyl alcohol polymers depend on the extent of polymerization and hydrolysis. Such changes cause both chemical and physical modifications such as esterification, etherification, crystallization, and ion-polymer complexation

in the polymer. Modified PVOH structures are useful in different areas like electrochemical applications, biomedical applications, etc.

1.4. Ionogels

The ILs can be considered as a powerful solvent for polymers due to their nonpolar nature. Recently, enormous research efforts have been employed in polymer solubility with the ILs. ILs may be cationic or anionic dependent but are not restricted to limited numbers including bis (trifluoromethanesulfonyl) amide-1-alkyl-3-methylimidazole (C4mimNTf2), N-butyl-N-methylpyrrolidone bis (trifluoromethanesulfonyl) amide (P14NTf2) for cationic structure dependence, and hexafluorophosphate-1-alkyl-3-methylimidazole (C4mimPF6), trifluoromethanesulfonate-1-alkyl-3-methylimidazole (C4mimTfO) for anionic structure dependence (14). The complexity in polymer dissolution in ILs begins with the engorgement of the polymer in the IL, by adsorbing, absorbing and trapping IL in the polymer network, bringing in polymer/IL binary systems. Such polymer/IL binary systems are termed *ionogels*. Their phase varies from liquid to solid via gel with an increase in the concentration of IL. In other words, the concentration of the polymer determines the viscosity of the binary system. Thus the category of ionogels includes low viscous liquids, gels, and solid films, etc.

This opens a gateway for new applications of the ionogels as solid polymer electrolytes in electrochemical devices, which overcomes all the limitations of the non-conducting polymers and the limitations of IL stemming from leakage due to its liquid nature.

Figure 5. Schematic diagram showing the solution casting on glass technique for the preparation of the ionogel film.

The ionogels can be prepared by simple solution casting on glass technique as shown in Figure 5. For that, 5g of polymer was dissolved in

50 ml of their respective solvent by vigorous stirring with a magnetic stirrer at 60°C until complete dissolution took place. This was followed by the addition of IL in order to obtain different proportions like 100:0, 95:05, 90:10, 80:20 and 70:30 of polymer matrix/ IL films, the higher concentration of IL led to the gel formation. The consistent hot solutions were poured into a specific mold and then dried at room temperature. The membranes were peeled off after keeping it in a vacuum oven at 110°C for 2 hours.

Thus, ionogels form a new class of hybrid materials which are just emerging, but considerably increase the potential of ILs in such key areas as energy, environment, and analysis. As we know, ILs are a tunable material: the properties can independently be modified by altering cation and anions. Beyond all these, ionogel offered one more degree of freedom, i.e., ''flexibility space'' by entrapping it in the polymer matrix (25). Immobilizing ILs within solid membranes gives access to all-solid devices, which are a technical challenge for practical applications (25).

1.5. Conclusion

Thus, replacing conventional organic electrolytes in electrochemical gadgets like lithium batteries and DSSCs, and replacing water in proton exchange membrane fuel cells (PEMFCs) with low vapor pressure and non-flammable ionogel offers significant advantages, like improved safety, stability, and higher operating temperature range. The implementation of ionogel as a solid polymer electrolyte membrane opens new routes for designing advanced materials, especially (bio)catalytic membranes, sensors, and drug release systems, etc. The use of ionogel as a gas-separating membrane benefits from the absence of contamination of the gas stream due to the low vapor pressure of ILs and thermal stability (26). Ionogels as active pharmaceutical ingredients (APIs) overcomes the limitations of their crystalline counterpart, such as polymorphism, low solubility, and low bioavailability associated with their solid form.

CHAPTER 2

COMPUTATIONAL INVESTIGATION ON IONOGELS

2.1. Introduction

The diverse choice in the polymer chemistry and the versatility of the ILs allow us to develop a large number of ionogel membranes—the compatibility of IL with the polymer matrix is a governing factor that determines the characteristic properties of the ionogel (14). A few combinations may have outstanding results while others may give rise to adverse effects. Similarly, the weight ratio of both ingredients will determine their nature: whether it is a highly viscous liquid or gel or a flexible sheet. So, one has to be more vigilant at the time of selection of guest and host as well as their weight ratios. Likewise, the lack of knowledge about the physiochemical properties of polymers, ILs, and possible interaction between them before preparation may lead to adverse results. In such situations, computational tools have been widely used to predict the interaction between dopant and host, most favorable weight ratio for optimum properties, etc. Such predictions may help ease the synthesis in the laboratory.

At the same time, we indeed cannot depend on such tools, since computational models can only be used to rule out a suitable model for a wide range of models. We can only expect approximations within the error limit using computational calculations. Moreover, computational modeling and calculations will help us get a better insight into the physiochemical properties of the developing ionogels. In this scenario, a nitty-gritty theoretical examination based on the optimized geometry of an individual IL and the influence of an IL in the polymer matrix is being anticipated to assess the unique properties, like structural, thermo-chemical, electronic, orbital, and optical properties (27–38). From the time when computational approaches gained significant worldwide attention, even experimentalists started to do computational modeling and predictions in order to underline and explain their experimental results (28). Thus computational predictions

will help us reduce the wastage of chemicals, trial and error, and human effort; it can thus be treated as an eco-friendly approach in research. Recently, however, there has been a trend to apply computational chemistry and cheminformatics to process development, analytical chemistry, and biology too (39, 40).

2.2. Theoretical Chemistry

Computational calculations in material science are hugely exciting and a fast-emerging field with implications for mathematics and quantum mechanics. Nowadays, modeling and simulations in complex systems such as biomolecules, organic-inorganic molecules, polymers, etc. are widely used. With the evolvement of fast and efficient computers and computer software, computational work becomes easy. Thus theoretical calculations can be employed to get a better understanding of the interaction of IL and polymer matrices. Similarly, the interaction of ILs with the PMMA matrix has been studied, and is discussed in the following sections.

With the growth of computational tools, scientists could eliminate the time-consuming and expensive experimental set-up. In 2013, Martin Karplus, Arieh Warshel, and Michael Levitt won the Nobel Prize in Chemistry for their work for better replication and to get the fine details of chemical reactions based on classical (Newtonian) physics and quantum physics in the 1970s. But before this, three well-known computational chemists, Mario Molina, Paul Crutzen, and F. Sherwood Rowland, won the Nobel Prize for constructing mathematical models to explain how ozone forms and decomposes in the atmosphere on the basis of thermodynamic and chemical laws. But, computational chemistry was not particularly revolutionized until 1998, when Walter Kohn and John Pople won the Nobel Prize in Chemistry for their work on density functional theory and computational methods in quantum chemistry (41).

The computational calculations open up a virtual platform that adds information to the experimental results. Computational calculations use molecular models, which may be quantum mechanical or molecular mechanical either with simple mathematical descriptions or completely non-mathematical visuals to solve, predict, and understand chemical problems.

2.2.1. Molecular mechanical computation

Molecular mechanical [MM] computation uses classical mechanics to solve chemical problems in which atoms are considered as particles with a

radius, polarizability, and constant net charge, and bonded interactions are treated as springs with an equilibrium distance equal to the experimental or calculated bond length. The energy can be expressed using simple classical equations like the harmonic oscillator equation in order to calculate the energy associated with bond stretching, bending, rotation, and intermolecular forces, such as Van der Waals interactions and hydrogen bonding (42). The potential energy associated with such a model can be expressed as the sum of energies of bond stretching, angle bending, torsional motion, and non-bonded interactions:

$$E = \sum_{bonds} E_{stretch} + \sum_{angles} E_{bend} + \sum_{dihedrals} E_{torsion} + \sum_{pairs} E_{nonbond}$$

in which the energy associated with bond stretching is proportional to the square of the change in the bond length:

$$E_{stretch} = k_{stretch}(l - l_{eq})^2$$

where $k_{stretch}$ is the proportionality constant, l is the length of the bond when stretched, and l_{eq} is the equilibrium length of the bond or natural length.

Similarly, the angle of bending energy varies with the square of the difference in angle, and hence the expression is given by:

$$E_{bend} = k_{bend}(a - a_{eq})^2$$

torsional energy is expressed as:

$$E_{torsion} = k_0 + \sum_{r=1}^{n} k_r[1 + \cos(r\theta)]$$

and non-bonding interactions are given by a Lennard–Jones 12–6 potential (43, 44)

$$E_{nonbond} = k_{nb}[(\frac{\sigma}{r})^{12} - (\frac{\sigma}{r})^{6}]$$

where "r" is the distance between the centers and "σ" is calculated from Vander Waal's radii.

Simply in MM, the energy of a system is given as a sum of two components:

$$E=E_{\text{covalent}}+E_{\text{non covalent}}$$

Where, the energy from the covalent includes the contribution from the bond, angles, and dihedral angles, while energy from the non-covalent considers the energy from the electrostatic interactions and Van der Waals interactions.

Molecular mechanics [MM] can be applied to a wide variety of systems ranging in size and complexity. It can be used to calculate the geometries and energies of polymers including proteins and nucleic acids. In complex calculations, the resulting structure can be used as a starting geometry for quantum mechanical methods. However, MM has some limitations in its accuracy and features compared with quantum mechanical calculations; the force fields have to be parameterized for each class of compounds separately, it does not consider the hyperfine structures and spin angular momentum. Any software that does *ab-initio*-type calculations can be used for MM calculations.

2.2.2. Quantum mechanical computation

Quantum mechanical computation is based on solving the Schrödinger equation:

$$H\psi = E\psi$$

where H is the Hamiltonian energy operator and ψ is the Eigenfunction with E as its Eigenvalue. The equation is unique for each system as the Hamiltonian energy operators vary between different systems. Be that as it may, a few systems can be solved rigorously with accuracy. For all other complex systems, the approximation technique can be used, which permits one to divide a Schrödinger equation into a set of smaller equations before carrying out Hückel calculations.

The Schrödinger equation can be solved at a different level of computational complexity. On the basis of this difference in the operational algorithm, modeling techniques can be classified into the following types:

- *Ab-Initio* QM modeling
- Semi-empirical method
- Density Functional Theory (DFT)

Ab-Initio QM modeling

Ab-initio QM modeling is a computational chemistry method used to solve the electronic Schrödinger equation to yield useful information on electron densities, ground state energy, and other properties. As the name implies, *Ab-initio* QM modeling starts with physical constants like the positions of the nuclei and the number of electrons as the input parameters. However, the *ab-initio* methods require large amounts of computer time, memory, and disk space. Moreover, the calculations are based on valence electrons, and it does not consider indistinguishability and spin of electrons.

Semi-empirical method

The semi-empirical method is a medium level approach; it is not as empirical as molecular mechanics, nor as theoretical as *ab-initio* calculations. A Fock matrix is designed and is diagonalized to get information regarding the molecular orbitals and their energy levels. The Fock matrix element is calculated from a core integral, density matrix elements P_{tu} and electron repulsion integrals $(rs \mid tu), (ru \mid ts)$ in the expression:

$$F_{rs} = H_{rs}^{core}(1) + \sum_{m}^{t=1} \sum_{m}^{u=1} P_{tu}[(rs|tu) - \frac{1}{2}(ru|ts)]$$

The input parameters are merely guessed coefficients for calculating density matrix values. This guess can be obtained from the simple Huckel calculation or an extended Huckel calculation. The Fock matrix element F_{rs} is subjected to repeated diagonalization to refine.

Density functional theory (DFT)

The main advantage of density functional theory (DFT) is to describe an interacting system of fermions using its density and not through its many-body wave function. The relationship between wave function and electron density is given as:

$$\rho = \sum_{i=1}^{n} n_i \mid \psi_i \mid^2$$

For the multi-electron system, the electron density will be more complicated, as N electrons in a solid, which obey Pauli's exclusion principle, repel each other via Coulomb potential. The basic variables of such a system depend only on the three spatial coordinates x, y, and z rather than 3×N degrees of freedom. Hence, the DFT gives a good description of ground state properties. Practical applications of DFT are based on approximations for the so-called exchange-correlation potential. In DFT the energy of a system is given as a sum of six components:

$$E_{DFT} = E_{NN} + E_T + E_v + E_{coul} + E_{exch} + E_{corr}$$

Where

E_{NN} = nuclear-nuclear repulsion energy

E_v = nuclear-electron attraction energy

E_{coul} = classical electron-electron Coulomb repulsion energy

E_T = kinetic energy of electrons

E_{exch} = the non-classical electron-electron exchange energies

E_{corr} = the energy from the correlated movements of electrons with different spins

Thus among all the above said computational methods, the DFT level of computation had been identified as most suitable for molecular level calculations in bio-molecular macromolecules, nanoparticles, polymer composites, etc.

2.2.3. ONIOM calculation

The main problem encountered by quantum chemists are related to accurate and reliable theoretical calculations for large molecular systems; but in actual practice, quantum chemistry can tackle more complicated and complex real situations in chemistry. For such essential cases, ONIOM (our N-layered integrated molecular orbital+ molecular mechanics) method was developed by Keiji et al. (45). This novel hybrid approach allows us to combine a variety of quantum mechanical methods as well as a molecular mechanical method in multiple layers, like the vegetable the *onion*.

Figure 6. Shows the layers inside an onion, a vegetable similar to ONIOM layers in computational calculations.

The case of ionogels is not different; they can be considered as complex molecules. Thus the lone quantum mechanical approach will be tiresome and expensive, whereas molecular mechanics will be inaccurate to study the relevant intramolecular and intermolecular interactions between the ionic liquid and the polymer matrix. Accordingly, we can also employ our novel hybrid theoretical approach, ONIOM, to get an insight into the structural behavior of the ionogels. This hybrid theoretical approach will provide a genuine opportunity to deal with ionogels by considering them as several layers and permit us to treat the layers separately with different levels of well-developed conventional computational methods. The most accurate quantum mechanical computational level (higher level) is given to the most and relatively smaller part of the real system, i.e., between the ionic liquid and polymers, where the probability of bond formation and bond breakage occur. Other parts of the ionogels, which are already optimized with the quantum mechanical approach and are not directly involved in the interaction between the IL and polymer host, are treated at less demanding computational levels (MM methods) (8).

In this ONIOM approach, prior calculations on ILs and polymers are essential, since the area where the molecular method applied was only to calculate the potential energy of the system through the use of force fields as given in the following equation:

$$E = E_{covalent} + E_{non\text{-}covalent}$$

Where, the energy from the covalent includes the contribution from bond, angles, and dihedral angles, while energy from the non-covalent considers the energy from the electrostatic interactions and Van der Waals

interactions. The MM methods are significantly faster than QM, but MM methods fail to compute various chemical reactions such as changes in chemical bonding and quantum effects including electronic excitations in the lower layer. Generally, the ONIOM hybrid approach is an energy subtraction method, and total energy can be expressed as:

$$E = E_{MM,\,real} + E_{QM,\,model} - E_{MM,\,model}$$

Here the term "real" refers to the whole system of the substrate, catalytic residue, solvent molecules, etc., and the term "model" refers to the substrate and residue only. The uniqueness of this approach is that the boundary terms are no longer an issue—it is possible to mix methods of any level of theory rather than just QM and MM as originally described—since the formulation is so simple that it is possible to add n-layers to the system and thus partition of the system in as many regions as one would like. The Gaussian 09 software (46) package allows at most three layers, which can be written as:

$$E = E_{low,\,real} + E_{medium,\,intermediate} + E,\,High,_{model} - E_{low\,intermediate} - E_{medium\,model}$$

where the terms "low, medium, high" respectively describe the low, middle, and high levels of theory. The term "real" describes the complete system, "model" describes only the region of interest, and "intermediate" means the boundary between the region of interest and rest of the system.

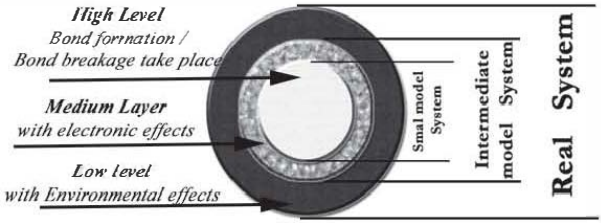

Figure 7. Schematic diagram representing the multilayers in the ONIOM approach.

Both semi-empirical (SE) methods and the DFT method with lower and higher basis set can be used for the ONIOM approach. The commonly used software packages for the computational calculations of the organic molecules are Gaussian 09 and Gauss view 05. The detailed discussions on these two are as follows. These hybrid calculations were employed as a novel approach to study the interaction between ionic liquids and polymers in the ionogels.

2.3. Computational software

The input structures for the computational calculations were downloaded from the PubChem database (47). The downloaded structures were converted to a Gaussian input file using Open Babel (48), and for further graphical manipulation, Gaussview-5.0 was used as a graphical user interface. All other computational calculations were done using the Gaussian 09 program. Further details regarding structures, level of theory, and basis set will be given in the respective working chapters. All the computational calculations for the entire work are performed in the Windows 10 platform using Dell Precision T5610 workstation with an Intel® Xeon® CPU E5-2620 v2 @ 2.10 GHz processor and 32.0 GB RAM.

2.3.1. Open Babel

Open Babel (48) is an open chemical toolbox which helps search, analyze, or convert data for research. The initial input structures were downloaded from the PubChem database in .sdf format. This software is used for the conversion of the .sdf file to a Gaussian input.

2.3.2. Gaussian 09

Gaussian 09 (46) is a new version of Gaussian, which is a computational tool used usually for quantum mechanical calculation. John Pople and his research group at Carnegie Mellon University initiated it in 1970. The name "Gaussian" originates from Pople's use of Gaussian orbitals to speed up calculations compared to those using Slater-type orbitals, a choice made to improve performance on the limited computing capacities of the then-current computer hardware for Hartree–Fock calculations. It allows for electronic structure modeling and predicts the energies, molecular structures, vibrational frequencies, and molecular properties of molecules and reactions in a wide variety of chemical environments using fundamental laws of quantum mechanics. Moreover, it can be applied to stable species and compounds that are difficult or impossible to observe experimentally (e.g., short-lived intermediates and transition structures). Gaussian 09 produces accurate, reliable and complete models without cutting corners with the full range of chemical conditions and problem sizes across the entire periodic table. Its flexibility and ease of handling make Gaussian unique among all other computational tools like Chemcraft, ChemDraw, and Avogadro, etc. In Gaussian, the algorithm used for optimization will vary the structure until changes have been made in the gradient and the

structure on two successive iteration convergences (49).

2.3.3. Gauss View 05

Gauss View is a graphical user interface designed to help us prepare input for submission to Gaussian and to examine the output of Gaussian jobs graphically. Gauss View is not integrated with the computational module of Gaussian, but rather is a front-end/back-end processor to aid in the use of Gaussian. Gauss View provides three main benefits to Gaussian users. First, through its advanced visualization facility, Gauss View allows us to rapidly sketch in every large molecule, then rotate, translate, and zoom in on these molecules through simple mouse operations. It can also import standard molecule file formats such as PDB files. Second, Gauss View makes it easy to set up many types of Gaussian calculations. It makes preparing complex input easy for both routine job types and advanced methods like ONIOM, QST2/QST3 transition structure optimizations, CASSCF calculations, periodic boundary conditions (PBC) calculations, and many more. The Gauss View can also be used to launch jobs as well if Gaussian is installed on the same computer (50, 51).

2.3.4. Chemcraft

Chemcraft is visualization software for preparing jobs structures by analyzing and manipulating the computed output files obtained from the Gaussian software. It helps visualize and extract information from the 3-dimensional pictures of molecules, isosurfaces of molecular orbitals, etc. In this work, Chemcraft was used mainly to create a customizable display of computed output images for publications that are discussed in successive chapters.

2.4. Computational methodology

2.4.1. Structural characterization

2.4.1.1. Potential energy surface and geometry optimization

The potential energy surface (PES) plays an essential role in understanding the relationship between potential energy and molecular geometry. A potential energy surface can be considered as a mathematical model depicting the energy of a molecule as a function of its geometry (stretches, bends, torsions, etc.). The stationary points on the potential energy

surfaces are the points on the PES where the gradients concerning all internal coordinates are zero. There are three types of stationary points namely:

- **Saddle point:** Stationary point that is minimal in all except one direction.
- **Local minima:** Stationary points that are minimal with respect to nearby surfaces.
- **Global minima:** Stationary point with the lowest energy of all the potential surfaces.

The geometry optimization of a compound starts with initial structure and proceeds through different structures by altering the specified variables; subsequently, the potential energy will be calculated. The structure with global minima can be considered as the most optimized geometry and considered for further geometrical optimization. Energy minimization is done on the obtained global minima by supplying possible geometry closer to it and systematically modifying the structure from energy minimization (mathematical statement for the energy minimization is shown below) to get the best-minimized geometry.

Let a function f that depends on independent variable x_1, x_2, x_3 . . . x_i with respect to each of the variable to zero and second derivative to a positive value.

$$\frac{\partial f}{\partial x_i} = 0 \quad \text{and} \quad \frac{\partial^2 f}{\partial x_i} > 0$$

where f is a mathematical function with x_1, x_2, x_3 . . . x_i as independent variables.

2.4.1.2. Frontier molecular orbital analysis

The frontier molecular orbital (FMO) plays a vital role in predicting the chemical reactivity of the molecules. FMO help us to understand the interaction between the highest occupied molecular orbital (HOMO) and the lowest unoccupied molecular orbital (LUMO) and the transition between them. The FMO decides the optical and electronic properties as well as reactivity, reaction mechanism, and kinetics of a molecule. HOMO gives information regarding the donation of the electron whereas LUMO gives information regarding the molecule's tendency to accept electrons.

The HOMO-LUMO energy difference (ΔE) directly gives the band gap or energy gap of the compound, which can be associated with the reactivity of the molecule. A molecule with a high energy gap (ΔE) is found to be less reactive when compared with a molecule with a larger energy gap. This energy gap can also be defined as the activation energy of the molecule. Thus without the activation energy, it is easily polarizable. In this work, the FMO of all molecules has analyzed and picturized the transition states and calculated its band gap.

2.4.2. Spectral characterization

2.4.2.1. Frequency calculations

Vibrational frequencies are figured out from the optimized geometry by defining the second derivatives of Cartesian nuclear coordinates (52). However, this calculation is only valid for a stationary point; computation of frequencies of any remaining geometry will be meaningless. Thus, once the optimization of the molecule is over in a stationary point of choice, it is compulsory to check whether the structure is optimized in the local minima or not. For that, normal modes of vibrations can be calculated; a structure with real minima has positive force constants for all normal modes. Normal modes of vibrations are nothing but the simplest vibrations where all atoms move in phase with frequency. The remaining vibrations of the molecule can be treated as the combination of the normal modes of vibration. The IR intensities of the vibrational modes were calculated as the derivative of the molecular dipole moment with respect to each normal coordinate. However, the calculated results were not in agreement with the experimental values. So, the calculated frequencies must be scaled down; the scaling factors may vary with the level of theory and basis set as shown below (53).

HF/6-31+G/6-311++G(d,p) method: 0.88 and 0.903
B3LYP/6-311++G (d,p) basis set: 0.980, 0.907, 0.955/0.920, 0.975
B3PW91/6- 31+G/6-311+G (d,p): 0.930,0.906, 0.955
and 1.02/0.910, 0.955, 0.982

The polarizability can also be computed from the normal modes of vibration with the keyword *polar*; from these polarisabilities the Raman optical activity can figure out.

2.4.2.2. UV—visible spectra

Time-dependent density functional theory (TDDFT) is used to study the electronic properties of the molecule in the excited states. TDDFT is the modified form of DFT, which concerns the time-dependent external potential energy that describes the photon-electron interaction. TDDFT is based on the Runge–Gross (RG) theorem, a time-dependent analog of the Hohenberg–Kohn theorem, which obeys the time-dependent Schrodinger equation.

$$H\psi(r,t) = i\hbar\frac{\partial\psi(r,t)}{\partial t}$$

The main advantage of the TDDFT is that it is capable of calculating electronic excitations and optical spectra. The UV spectra can be plotted from the energy of the excited states as ε vs. λ, where ε is the absorptivity of the sample and λ is the excitation wavelength in nm. The theoretically obtained peak in the spectra assume a Gaussian band shape of the form

$$\varepsilon_i(\vartheta) = \varepsilon_i^{max}\exp\left[-\left(\frac{\vartheta-\vartheta_i}{\sigma}\right)^2\right]$$

where the i subscript refers to the electronic excitation of interest. From the value of maximum absorptivity ε_i^{max}, the absorbance "A" of the sample can be calculated using Beer's Law:

$$A = \varepsilon_i^{max} IC$$

where I = path length in cm, C is the concentration (mol/L).

2.4.3. Thermochemistry

The thermo-chemical parameters are important in determining the possibility and temperature dependence of a chemical reaction. It also helps us understand the interaction and the forces between intermolecular as well as intramolecular atoms. Thermo-chemical properties including enthalpy (H), entropy (S), and Gibbs free energy (G) determine whether the product is plausible. A reaction is feasible when its Gibbs free energy change is negative, i.e., the more negative the G value, the more feasible it is. The changes in G value reported in the present work correspond to the following reaction:

$$\Delta G = G_{Ionogel} - (G_{Ionic\ liquid} + G_{Polymer\ matrix})$$

The enthalpy of formation of ionogel can be calculated using the formulae:

$$\Delta H = H_{Ionogel} - (H_{Ionic\ liquid} + H_{Polymer\ matrix})$$

In this work, we checked the compatibility and feasibility of all reactions.

2.4.4. Global Descriptive Parameters

The global descriptive parameters of the molecule give the relation between the chemical reactivity of the molecule and its sensitiveness to structural perturbations and responses to the changes in external conditions. These quantities depend on the electron density concerning the changes in the external potential and number of electrons (54). Thus global descriptors are of particular relevance in comparing the properties of different molecules; here they allow us to compare the properties of the product to reactants. To understand the reactive nature of all the products in this work, the global descriptors, including hardness, softness, chemical potential, electronegativity, and electrophilicity index (28), were calculated using Koopman's theorem for closed-shell compounds, as follows:

$$\text{Ionization Potentials (IP)} \approx - E_{HOMO}$$

$$\text{Electron Affinity (EA)} \approx - E_{LUMO}$$

where E_{HOMO} is the energy of HOMO and E_{LUMO} is the energy of LUMO

$$\text{Hardness } (\eta) \approx \frac{IP-EA}{2}$$

$$\text{Electro negativity } (\chi) \approx \frac{IP+EA}{2}$$

$$\text{Softness(S)} \approx \frac{1}{2\eta}$$

$$\text{Chemical potential } (\mu) \approx -\chi$$

$$\text{Electrophilicity index } (\omega) \approx \frac{\mu^2}{2\eta}$$

The global hardness reflects the overall stability of the system (55). The chemical hardness fundamentally signifies the reluctance towards the deformation or polarization of the electron cloud of the atoms, ions, or molecules under small perturbation encountered during chemical processes. Chemical softness is the measure of the capacity of a molecule to receive electrons; more precisely it is related with the groups or atoms present in that molecule and is inversely proportional to chemical hardness. The chemical potential in DFT, which measures the escaping tendency of an electron from equilibrium, is accounted by the first derivative of energy with respect to the number of electrons (56) and is also the negative of electronegativity, which is a measure of the tendency to attract electrons in a chemical bond. The electrophilic index tells us about the strength of electrophilicity of the species (57). Two different methods can calculate global reactive descriptors, one is based on the difference in total electronic energy of a neutral molecule and its corresponding anion and cation, obtained from the geometry of the neutral molecule in order to keep the external potential constant; it is usually called the *energy vertical* (58). The global properties are computed by using the equations given above (59).

2.4.5. Nonlinear optical properties

The computational approach can also be used as an inexpensive way to study the interaction of electromagnetic fields in various media to produce new fields which are altered in frequency, phase, and amplitude, or other propagation characteristics from the incident fields. The polarization P, induced in a medium by an external electric field F, is given by

$$P = P_0 + \chi^{(1)} F + \chi^{(2)} F^2 + \chi^{(3)} F^3 + \ldots$$

where $\chi^{(n)}$ is the n^{th} order susceptibility tensor of the bulk medium.

The dipole moment of a molecule interacting with an electric field can be written

$$\mu_i = \mu_i^0 + \alpha_{ij} F_j + (1/2)\beta_{ijk} F_j F_k + (1/6)\Upsilon_{ijkl} F_j F_k F_l + \ldots$$

where μ_i^0 is the permanent dipole moment and α_{ij}, β_{ijk}, and Υ_{ijk} are tensor elements of the linear polarizability and first and second hyperpolarizabilities respectively. This interaction may even lead to nonlinear optical effects (NLO). In this direction in order to study the NLO properties, the dipole moment, first static hyperpolarizability (β_{tot}), and their related properties

including α, β, and Δα of the molecules can be calculated computationally. The second order term of the hyperpolarizability gives rise to sum and difference frequency mixing (including second harmonic generation) and optical rectification. The third order term is responsible for the third harmonic generation and two-photon resonances. The polarizability and hyperpolarizability of NLO can be written as tensors. The linear polarizability tensor α is shown below, which is a 3×3 matrix having nine components.

$$\alpha = \begin{bmatrix} \alpha_{xx} & \alpha_{xy} & \alpha_{xz} \\ \alpha_{yx} & \alpha_{yy} & \alpha_{yz} \\ \alpha_{zx} & \alpha_{zy} & \alpha_{zz} \end{bmatrix}$$

$$\alpha_{total} = \frac{\left(\alpha_{xx} + \alpha_{yy} + \alpha_{zz}\right)}{3}$$

Alternatively, the first hyperpolarizability, the quantity of interest β is a 3×3×3 matrix, has β_{xzz}, β_{xxx}, β_{xyy}, β_{yyy}, β_{yzz}, β_{yxx}, β_{zzz}, β_{zxx} β_{zyy}, β_{xyz}, respectively, from which the x, y, and z components of β are calculated as

$$\beta_{total} = \sqrt{\left(\beta_{xxx} + \beta_{xyy} + \beta_{xzz}\right)^2 + \left(\beta_{yyy} + \beta_{yzz} + \beta_{yxx}\right)^2 + \left(\beta_{zzz} + \beta_{zxx} + \beta_{zyy}\right)^2}$$

Comparing the values of polarizability and Hyperpolarizabilities of molecules with one of the prototypical molecules, urea (μ and β of urea is 4.56 D and 48× 10^{-36} esu) (60), one can predict the nonlinear optical activity of any molecule.

2.5. Compatibility of ILs with PMMA matrix

2.5.1. Geometry

The three levels ONIOM method (n-layered integrated molecular orbital and molecular mechanics approach) was implemented in the Gaussian 09 program package for the geometry optimization of the ionic liquid polymer composite. The ONIOM multilevel extrapolation method helped us divide the molecular system into two–three layers in which the inner part of IL along with the surrounding atoms from the polymer was treated using a "high-level" theory and the rest of the system as described dealt with the computationally less demanding method "lower level." The

level of theories and corresponding basis set used for the optimization of all the samples were tabulated in Table 2.

Table 3. The level of theories and corresponding basis set used for the optimization of MMA, PMMA, [BMPyr] [TFSI], [EMIM] [SCN], and their polymer composites.

Sl.No	Sample	Theory	Basis Set
1.	MMA	DFT/B3LYP	321-G
2.	PMMA	DFT/PBEPBE	321-G
3.	[BMPyr] [TFSI]	DFT/B3LYP	631-G(d,p)
4.	[EMIM] [SCN]	DFT/B3LYP	631-G(d,p)
5.	PMMA/[BMPyr] [TFSI]	ONIOM/SM:DFT:SM	PM6: 321-G:PM6
6.	PMMA/ [EMIM] [SCN]	ONIOM/SM:DFT:SM	PM6: 321-G:PM6

From the optimized geometry of the composite of both polymers, the intermolecular hydrogen bonding between the PMMA host and two ILs ([BMPyr] [TFSI] and [EMIM] [SCN]) were assessed after omitting the intramolecular hydrogen bonding, depicted in Figure 8. According to the optimized geometry of the PMMA/ [BMPyr] [TFSI] composite, there are at least 4 H-bonds between [BMPyr] [TFSI] and PMMA; 1 bond from the 114-O and three bonds from the 101-O. All the H-bonds were originated from the BMPyr cation to the oxygen of the PMMA chain. Similarly, PMMA/ [EMIM] [SCN] exhibited at least 3 H-bonds between the cation and the oxygen atom of the PMMA chain; 1 bond from 24-O and two bonds from 64-O (61).

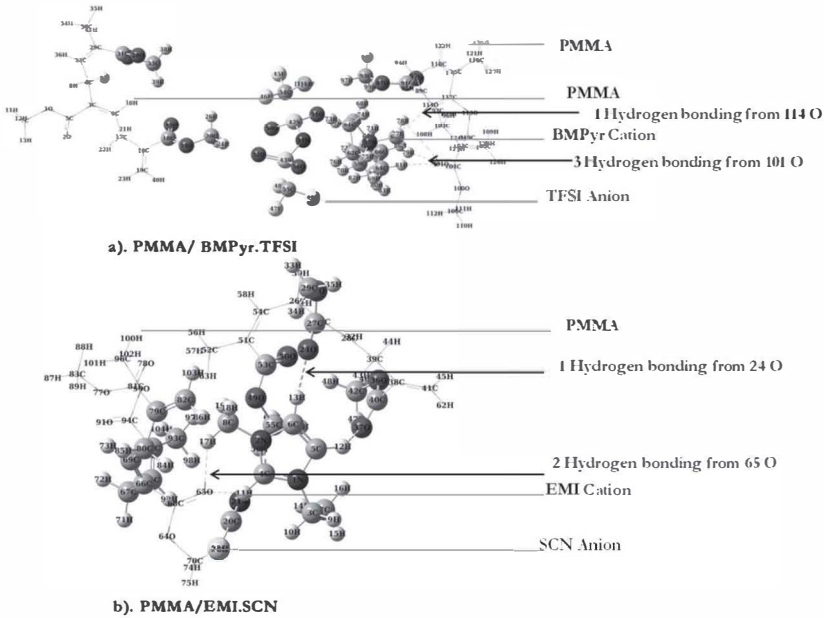

Figure 8. Optimized geometry and H-bonding in a) PMMA/ [BMPyr] [TFSI] and b) PMMA/ [EMIM] [SCN] systems.

2.5.2. Thermo-chemical properties

In this section, the compatibility and feasibility of two PMMA-based ionogels were determined from the thermochemical parameters, since these parameters play a crucial role in the chemical reaction. The thermo-chemical parameters of the PMMA-based ionogel membranes were computed and tabulated in Table 3. It is found that the Gibbs free energy of PMMA/[BMPyr] [TFSI] is -1835367.45 kcal/mol while that of PMMA/ [EMIM] [SCN] is -1169654.06 kcal/mol: the more negative the value of G, the greater the thermodynamic feasibility.

Similarly, thermodynamic feasibility can be determined in terms of entropy; the higher the value of entropy, the more will be the reactivity. In our calculation, it is found that PMMA/[BMPyr] [TFSI] has 449.88 cal/mol points of entropy, which indicates that PMMA/[BMPyr] [TFSI] is more stable than PMMA/ [EMIM] [SCN] (352.49 cal/mol) ionogel membrane.

The positive value of ΔH for both the IL-based polymer composite exhibits their endothermic nature. The change in enthalpy for PMMA/[BMPyr] [TFSI] is 602969 kcal/mol, while that of PMMA/ [EMIM] [SCN] is 22.09kcal/mol, which indicates that the binding of [BMPyr] [TFSI] in the PMMA matrix is highly energy demanding. This the vague idea that [BMPyr] [TFSI] tries to bind into the polymer matrix by forming strong hydrogen bonds while the [EMIM] [SCN] tries to entrap in the voids of the PMMA matrix.

Table 4. The thermodynamic parameters of MMA, PMMA, [BMPyr] [TFSI], [EMIM] [SCN], and their polymer composites PMMA/[BMPyr] [TFSI] and PMMA/ [EMIM] [SCN].

Sl. No	Sample	Molecular Mass (amu)	Energy (Kcal/mol)	Dipole Moment (Debye)	Enthalpy (Kcal/mol)	Entropy (Cal/mol)	Gibbs Free Energy (Kcal/mol)
1.	MMA	100.05	-2.15e+005	1.49	-215495.77	81.46	-215519.47
2.	PMMA	296.12	-6.45e+005	6.32	-645144.01	46.78	-645181.49
3.	[BMPyr] [TFSI]	422.07	-1.40e+006	15.57	-140347.99	195.24	-1403525.61
4.	[EMIM] [SCN]	169.06	-5.24e+005	11.50	-524427.35	116.09	-524462.046
5.	PMMA/[BMPyr] [TFSI]	1014.32	-1.82e+006	18.45	-182522.21	449.88	-1835367.45
6.	PMMA/ [EMIM] [SCN]	761.31	-1.1e+006	12.49	-1169549.27	352.49	-1169654.06

Though both ionogel membranes exhibited large electronegativities of the bonded atoms when compared with their parental counterparts [BMPyr] [TFSI] and [EMIM] [SCN], the dipole moment of the ionogel membrane is found to increase on formation of the ionogel, emphasizing strong *ion-dipole interaction* rather than ion-ion interaction when IL is doped in a polar matrix. Hence, we can conclude that the charge delocalization is increasing in the solid polymer electrolyte due to electron disordering of respective IL in PMMA matrix.

2.5.3. Vibrational analysis

The vibrational spectra can be considered as a fingerprint of each molecule. Thus the FT-IR spectroscopy and theoretical studies can be considered as a vital tool to study the interaction between the polymer matrix and the doped ILs. The FTIR spectra in the range of 3500–500 cm^{-1}

of PMMA in the presence of [BMPyr] [TFSI] IL is shown in Figure 9, while that of [EMIM] [SCN] IL is shown in Figure 10. The frequencies were computed from the optimized structures using the same hybrid ONIOM approach with certain systematic errors. In the meantime, measures were considered to account for errors due to the neglecting electron correlation and the basis set incompleteness. The systematic errors of B3LYP were considered with a 0.983 scaling factor for below 1700 cm^{-1} and 0.958 for above 1700 cm^{-1} (62, 63). For experimental analysis, attenuated total reflectance–Fourier transform infrared (ATR-FTIR) spectroscopy was used to get evidence of [BMPyr] [TFSI] and [EMIM] [SCN] doped ionic liquid in the host PMMA polymer matrix.

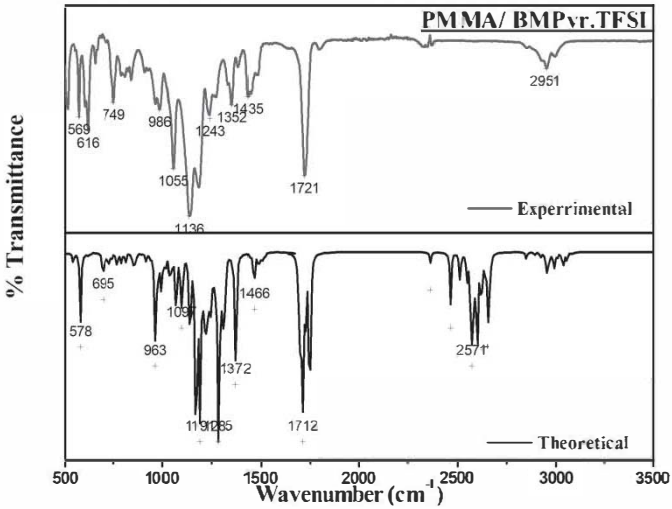

Figure 9. Vibrations of PMMA/[BMPyr] [TFSI] polymer composite (14, 22).

The characteristic peaks of isotactic PMMA were observed in both polymer composites as shown in Figure 9 & Figure 10 at 695-790 cm^{-1} (C-H bending), 841 cm^{-1} (C=C bending/alkenes), 963-1089 cm^{-1} (C=C Bending/Alkene), 1235-1242 cm^{-1} (C-O Stretching/Alkyl aryl ether), 1352-1364 cm^{-1} (C-H Bending/Aldehyde group), 1436-1466 cm^{-1} (C-O Stretching), 1712-1728 cm^{-1} (C=O stretching/α,β-unsaturated ester), and 2571-2951 cm^{-1} (CH Stretching/Alkane groups) (64).

The presence of [BMPyr] [TFSI] IL was confirmed in the PMMA/ [BMPyr] [TFSI] polymer composite from the presence of bands centered

at 512-578 cm^{-1} (TFSI anion), 616-695 cm^{-1} (TFSI anion), 1055-1097 cm^{-1} (S=O Stretching), and 1181-1136 cm^{-1} (S=O Stretching) and from the absence of C-O stretched vibration as depicted in Figure 9.

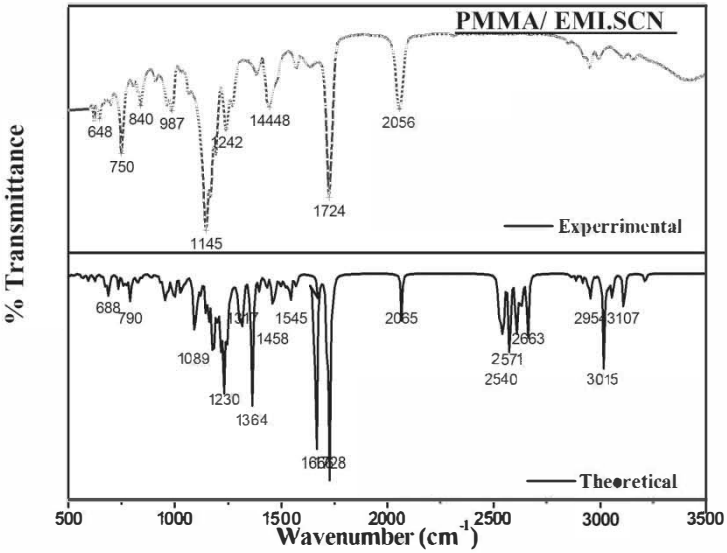

Figure 10. Vibrations of PMMA/ [EMIM] [SCN] polymer composite.

The presence of [EMIM] [SCN] IL in the PMMA/ [EMIM] [SCN] polymer composite can be solely confirmed from the presence of an additional band centered at 2056-2065 cm^{-1} (SCN anion), in addition to the bands of PMMA and EMIM as depicted in Figure 10.

2.5.4. Global descriptive parameters

To understand the reactive nature of the IL-based polymer composite and to trace out the most reactive ionogel, the global descriptors including hardness, softness, chemical potential, electronegativity, and electrophilicity index were calculated using Koopman's theorem (28).

The calculated global descriptive parameters of MMA, PMMA, [BMPyr] [TFSI], [EMIM] [SCN], and their polymer composite are given in Table 4.

Table 5. The ionization energy, electron affinity, electronegativity, chemical potential, electrophilicity, hardness and softness of MMA, PMMA, [BMPyr] [TFSI], [EMIM] [SCN] and their polymer composites PMMA/[BMPyr] [TFSI] andPMMA/ [EMIM] [SCN].

Sl.No	Sample	IE (ev)	EA (ev)	χ(ev)	μ (ev)	ω (ev)	η (ev)	S
1.	MMA	3.56	0.65	2.11	-2.11	0.00	1.36	0.36
2.	PMMA	2.55	1.92	2.23	-2.23	7.934	0.31	1.61
3.	[BMPyr] [TFSI]	7.00	1.08	4.04	-4.04	2.76	2.96	0.16
4.	[EMIM] [SCN]	8.17	0.28	4.22	-4.22	2.259	3.94	0.126
5.	PMMA/[BMPyr] [TFSI]	5.96	1.82	6.87	-6.87	4.672	5.05	0.099
6.	PMMA/ [EMIM] [SCN]	4.662	1.144	5.23	-5.23	3.348	4.09	0.122

The values emphasize that the whole ionogel membrane understudy is hard enough, so that the IL-based solid polymer composite is stable in its ground state. The ionization energy of PMMA/[BMPyr] [TFSI] and PMMA/[EMIM] [SCN] is comparatively higher than PMMA matrix and lower than the respective IL, which indicates that the IL-based polymer composite has considerably greater stability than the respective IL. In addition, PMMA/[EMIM] [SCN] exhibited higher reactivity than PMMA/ [BMPyr] [TFSI], the polymer composite. It is again confirmed from the higher values of hardness for PMMA/[BMPyr] [TFSI], which in turn attributed to the presence of strong intermolecular hydrogen bonding in the polymer composite. It is surprising to note that the hardness of [BMPyr] [TFSI] is increased when it is entrapped in the PMMA matrix while that of [EMIM] [SCN] is not altered, indicating the decrease in the chemical reactivity of [BMPyr] [TFSI] in the polymer composite. This discrepancy may be due to the formation of hydrogen bonding between the [BMPyr] [TFSI] and PMMA matrix, which in turn makes [BMPyr] [TFSI] less reactive in the polymer composite. While the studies show that [EMIM] [SCN] is much more free to be more reactive due to their immiscible nature in the PMMA matrix, it is just entrapped it in it. In a similar manner the electrophilicity index of PMMA/[BMPyr] [TFSI] is higher than that of PMMA/[EMIM] [SCN], signifying maximal electron flow between donor and acceptor.

2.5.6. Optical properties

The optical parameter plays a decisive role in determining the suitability of a material for optical devices. The room temperature UV-visible absorption spectra in the range 200 to 800 nm for the IL-based polymer composite were taken using a JASCO-V550 spectrophotometer, while electronic transitions were computed using the TDDFT/B3LYP/6311-G+d level of theory. Figure 11a shows the room temperature absorption spectra for the prepared IL-based polymer composites along with their theoretical predictions in the range 200 800 nm. All the samples retain the absorption of PMMA in the range of 200 250 nm (65).

The active band observed at 223 nm for PMMA/[BMPyr] [TFSI] might be assigned to the n-→π* transition due to the presence of the C=O group; meanwhile the other two absorptions may be assigned to the π-→π* transition due to the unsaturated groups [46] (C=O, C=C) in the polymer (14).

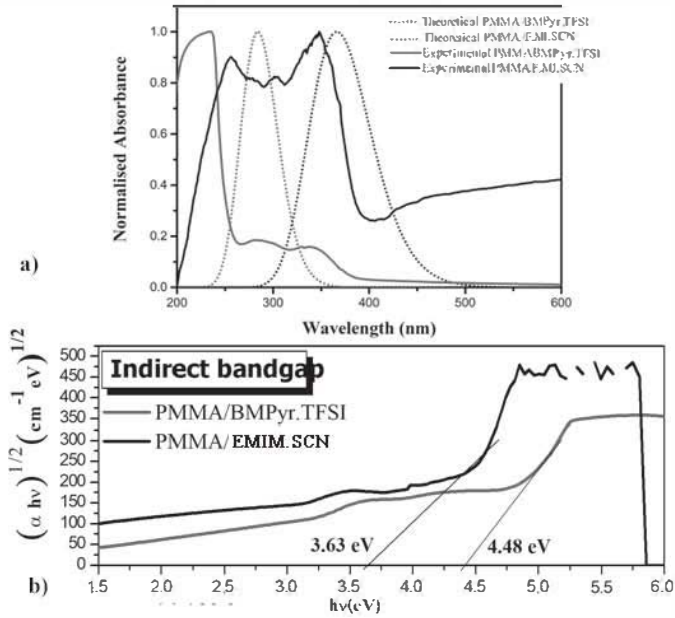

Figure 11. a) The theoretical and experimental optical absorbance of prepared polymer composites PMMA/[BMPyr] [TFSI] and PMMA/[EMIM] [SCN]. b) Indirect band gaps of prepared polymer composites PMMA/[BMPyr] [TFSI] and PMMA/[EMIM] [SCN].

The absorption coefficient of PMMA/[BMPyr] [TFSI] and PMMA/[EMIM] [SCN] was calculated using the equation shown below

$$\alpha = \frac{2.303A}{t}$$

where α is the absorption coefficient, A is the optical absorbance of the film, and t is the thickness of the film. The indirect band gap of SPE plays an important role since it determines the energy required to transfer an electron from the highest occupied molecular orbital (HOMO) to the lowest unoccupied molecular orbital (LUMO) in order to make the film optically active. The smaller the band gap, the higher will be their charge conduction (14). The optical band gaps of PMMA/ [BMPyr] [TFSI] and PMMA/[EMIM] [SCN] composite films involving indirect electronic transitions are depicted in Figure 11b. The experimental results show that PMMA/[BMPyr] [TFSI] have a band gap of 4.48 eV while that of PMMA/[EMIM] [SCN] have a band gap of 3.63 eV(66).

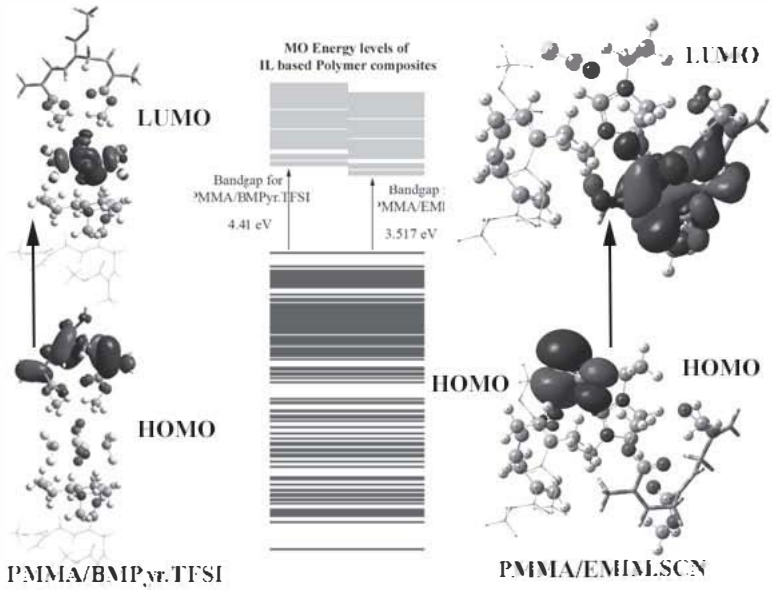

Figure 12. The HOMO and LUMO molecular orbitals of prepared polymer composites PMMA/[BMPyr] [TFSI] and PMMA/[EMIM] [SCN].

On the basis of the frontier molecular orbital approach, the HOMO and LUMO are mainly responsible for electron transitions. The transition from HOMO to LUMO in the PMMA/[BMPyr] [TFSI] is characterized by $n\rightarrow\pi^*$ from the PMMA to anion with a band gap of 4.41 eV; at the same time, the transition from HOMO to LUMO in the PMMA/[EMIM] [SCN] is characterised by $n\rightarrow\pi^*$ from the anion SCN to PMMA with a band gap of 3.517 eV. These results were in good agreement with that of the experimental values.

2.5.7. NLO properties

The electronic dipole moment μi, polarizability α_{ij} and the first hyperpolarizability β_{ijk} of all PMMA based ionogel membranes (PMMA/[BMPyr] [TFSI] and PMMA/[EMIM] [SCN]) were calculated at QM and hybrid ONIOM level using the Gaussian 09W program package and were listed in Table 5 and Table 6.

Table 6. The calculated dipole moment μ (Debye), the polarizability α_{tot} of PMMA, [BMPyr] [TFSI], [EMIM] [SCN] and their polymer composites PMMA/[BMPyr] [TFSI] and PMMA/ [EMIM] [SCN].

Sl.No	Sample	Dipole moment (Debye)	α_{xx}	α_{yy}	α_{zz}	α_{tot} x 10^{-24} (esu)
1	PMMA	6.3281	70.9869	40.87622	344.3495	225.0649
2	[BMPyr] [TFSI]	15.5780	118.7628	153.0201	125.7807	196.1314
3	[EMIM] [SCN]	11.5017	99.63988	193.5383	30.65181	159.7561
4	PMMA/[BMPyr] [TFSI]	18.4526	540.44	2258.47	2294.68	2512.833
5	PMMA/ [EMIM] [SCN]	12.4959	254.39	270.09	189.69	352.3288

The computational quantum mechanical NLO calculations of the IL-based polymer composite revealed that both samples, PMMA/[BMPyr] [TFSI] and PMMA/[EMIM] [SCN], exhibit the nonlinear response. The calculated polarizability α_{ij} had non-zero values and was dominated by the diagonal components, while the hyperpolarizability β dominated by the longitudinal components of β_{xxx}, β_{xxy}, β_{xyy}, and β_{yyy}. It is found that PMMA/[BMPyr] [TFSI] has a dominating dipole moment, polarizability, and first-order polarizability compared with the PMMA/[EMIM] [SCN] and PMMA matrix. This may be due to the high polar nature of [BMPyr] [TFSI]; the dipole moment of [BMPyr] [TFSI] is 15.5780 Debye while that of [EMIM] [SCN] is 11.5017 Debye; in a similar manner, the

polarizability of [BMPyr] [TFSI] is 196.1314×10^{-24} esu and that of [EMIM] [SCN] is 159.7561×10^{-24} esu. The crucial nonlinearity determining factor (β), is also high for [BMPyr] [TFSI]. Consequently, the highest value of dipole moment is observed for PMMA/[BMPyr] [TFSI] polymer composite 18.4526 Debye, and the calculated polarizability α_{tot}, (2512.8×10^{-24} esu) and hyperpolarizability (4.54×10^{-30}esu) is highest for PMMA/[BMPyr] [TFSI] when compared with the other.

Table 7. The calculated first hyperpolarizability $\beta_{tot}$of PMMA, [BMPyr] [TFSI], [EMIM] [SCN] and their polymer composites PMMA/[BMPyr] [TFSI] and PMMA/ [EMIM] [SCN].

Sample	β_{xxx}	β_{xyy}	β_{xzz}	β_{yyy}	β_{yzz}	β_{yxx}	β_{zzz}	βx 10^{-30} (esu)
PMMA	-160.03	-47.18	-1.49	-10.09	-13.1	66.57	-0.065	1.84
[BMPyr] [TFSI]	101.78	1.99	20.27	1.59	-0.29	-22.58	-13.95	1.16
[EMIM] [SCN]	103.56	29.91	10.90	6.90	11.08	5.94	-15.58	1.26
PMMA/ [BMPyr] [TFSI]	325.63	-3.81	61.48	186.59	30.17	-127.73	118.63	4.54
PMMA/ [EMIM] [SCN]	158.90	156.49	78.90	-11.94	64.67	59.67	-101.8	4.00

However, when we compare the values of the dipole moment, polarizability, and hyperpolarizability of two ILs and two polymer composites with that of the reference values of urea and p-nitroaniline, which are considered as prototypical donor-acceptor organic molecules with large hyperpolarizability (67), it is interesting to note that both polymer composites exhibit nonlinear optical behavior higher than urea (α_{tot} = -8.88×10^{-24}esu, β_{tot}=0.00518×10^{-30} esu) and comparable to that of p-nitroaniline (β_{tot}=11.464×10^{-30} esu). Nevertheless, by considering the miscibility and other optical property, it is worthwhile to point out the nonlinear behavior of the PMMA/[BMPyr] [TFSI] polymer composite.

2.6. Compatibility of ILs with PVA matrix

In a similar way, the interaction of ILs with the PMMA matrix has been studied, and the affinities of ILs with PVA matrixes have also been evaluated and are discussed in the following sections.

2.6.1. Geometry

Two levels of the ONIOM method (n-layered integrated molecular orbital and molecular mechanics approach) were implemented in the Gaussian 09 program package for the geometry optimization of PVA-based ionogel membranes. The ONIOM multilevel extrapolation method helped us divide the molecular system into two layers in which the inner part of IL along with the surrounding atoms from the polymer were treated using a "high-level" theory and the rest of the system described dealt with a computationally less demanding method at a "lower level." The level of theories and the corresponding basis set used for the optimization of all the samples were tabulated in Table 7.

Table 8. The level of theories and the corresponding basis set used for the optimization of PVA, [BMPyr] [TFSI], [EMIM] [SCN] and their polymer composites.

Sl.No	Sample	Theory	Basis Set
1.	PVA	DFT/PBEPBE	321-G
2.	[BMPyr] [TFSI]	DFT/B3LYP	631-G(d,p)
3.	[EMIM] [SCN]	DFT/B3LYP	631-G(d,p)
4.	PVA/[BMPyr] [TFSI]	ONIOM/SM:DFT	PM6:631-G
5.	PVA/ [EMIM] [SCN]	ONIOM/SM:DFT	PM6:631-G

From the optimized geometry of both polymer composites, the intermolecular hydrogen bonding between the PVA host and the respective two ILs ([BMPyr] [TFSI] and [EMIM] [SCN]) were assessed and depicted in Figure 13 after omitting the intramolecular hydrogen bonding. According to the optimized geometry of the PVA/ [BMPyr] [TFSI] composite, there are at least two H-bonds between [BMPyr] [TFSI] and PVA; one bond from the 9-O to 63-H and one bond from the 11-O to 57-H. All the H- bonds were originated from the TFSI cation to hydrogen atom of the PVA chain. Similarly, PVA/ [EMIM] [SCN] exhibited at least two H-bonds between the cation and the oxygen atom of the PVA chain; 1 bond from 22-O to 47-H and one bond from 8-O to 44-H (61).

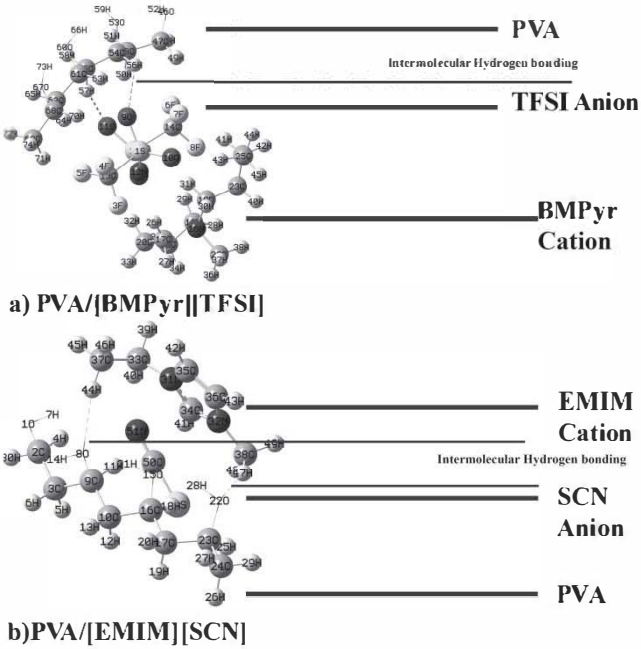

Figure 13. Optimized geometry and H-bonding in a) PVA/ [BMPyr] [TFSI] and b) PVA/ [EMIM] [SCN] systems.

2.6.2. Thermo-chemical properties

The thermo-chemical properties, including enthalpy, entropy, and Gibb's free energy of PVA-based ionogel membranes, were obtained from the Gaussian out file directly and tabulated in Table 8. Knowing the thermochemical properties, one could easily understand the feasibility of a reaction.

Both the ILs interact with the PVA matrix in a thermodynamically feasible manner with stable energy values. However, after an in-depth look at the free energy values of both, we could determine that [EMIM] [SCN] is more stable than [BMPyr] [TFSI] in the PVA matrix. At the same time, the entropy value of PVA/[EMIM] [SCN] emphasizes that it is reactive enough, though it is stable. The exothermic nature of the chemical reaction was predicted from the enthalpy of formation.

Table 9. The thermodynamic parameters of [BMPyr] [TFSI], [EMIM] [SCN] and their polymer composites PVA/[BMPyr] [TFSI] and PVA/ [EMIM] [SCN].

Sl. No	Sample	Molecular mass (amu)	Energy (Kcal/ mol)	Dipole moment (Debye)	Enthalpy (Kcal/ mol)	Entropy (Cal/ mol)	Gibbs free energy (Kcal/ mol)
1.	[BMPyr] [TFSI]	422.07	-1.40e+ 006	15.5780	-140347.99	195.24	-1403525.61
2.	[EMIM] [SCN]	169.06	-5.24e+ 005	11.5017	-524427.35	116.094	-524462.046
3.	PVA/[BM Pyr] [TFSI]	600.19	-1.59 e+ 006	17.6554	-1592961.9	264.674	-1593040.22
4.	PVA/ [EMIM] [SCN]	347.18	-7.2e+ 005	12.7016	-722333.38	195.817	-722391.17

2.6.3. Vibrational analysis

Just like our fingerprints, an FTIR spectrum is unique to each compound, and thus FT-IR spectroscopy can be considered as an efficient tool to study the functional groups in organic compounds. The frequencies of study ILs were computed from the optimized structures using the same hybrid ONIOM approach with certain systematic errors; the scale down information was discussed in section 2.4 and the spectra were shown in Figure 14.

The theoretical and experimental spectra are close to each other. It retained all the relevant peaks of PVA (64). The observed transmittance at 827 cm^{-1} (C=C Bending/ Alkenes), 915 cm^{-1} (CH_2), 1085 cm^{-1} (C-O Stretching/ Alkyl aryl ether), 1386 cm^{-1} (C-H Bending/ Aldehyde group), 1413 cm^{-1} (C-O Stretching), 1643 cm^{-1} (C=O stretching /α,β-unsaturated ester), and 2918 cm^{-1} (CH Stretching/ Alkane groups) correspond to the presence of host PVA matrix (68).

The characteristic band at 1169 cm^{-1} and 2064 cm^{-1} relates to the C=O and SCN^- anion respectively, which are solely required to affirm the presence of IL in the PVA matrix; the increase in intensity denotes an increase in the concentration of IL in the films as weight proportion increments (14, 69–72)

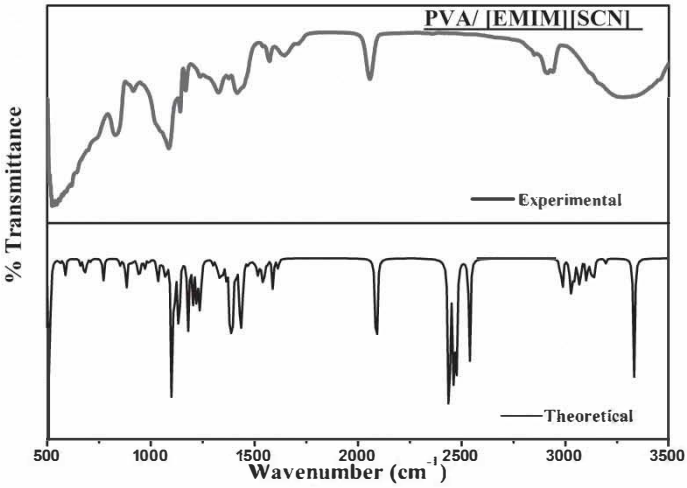

Figure 14. Vibrations of PVA/ [EMIM] [SCN] polymer composite.

2.6.4. Global descriptive parameters

In order to get a clear-cut idea about the reactivities of PVA-based ionogel membranes and to trace out the best compatible IL for the PVA matrix; the global descriptors were calculated in terms of hardness, softness, chemical potential, electronegativity, and the electrophilicity index using Koopman's theorem (28).

The computed global descriptive parameters of PVA, [BMPyr] [TFSI], [EMIM] [SCN], and their polymer composite were given in Table 4. The hardness values of both ionogels record that all PVA-based ionogel membranes were stable enough in the ground state. However, the hardness value is slightly lowered for the PVA/[EMIM] [SCN] composite indicating the free availability of ions in the matrix. The ionization energy of both ionogels is comparatively higher than that of the two ILs, which indicates that IL-based polymer composites have considerable stability compared with the respective IL. However, when the EA values were increased for both the composites, the PVA/[EMIM] [SCN] had a better electron-accepting capacity compared with others, which indicates the reactive nature of the [EMIM] [SCN] ionogel membrane. This is again confirmed from the electrophilicity values. The softness values show that, in the PVA matrix, the reactivity lessened for [BMPyr] [TFSI] while it is increased for [EMIM] [SCN]. However, it is surprising to note that the reactivities are higher in the PVA matrix than in the PMMA matrix, which

may be due to the availability of void spaces in PVA and because their hydrophilic nature encourages the IL to be trapped in the PVA matrix.

Table 10. The global descriptive parameters of PVA, [BMPyr] [TFSI], [EMIM] [SCN] and the polymer composites PVA/[BMPyr] [TFSI] and PVA/ [EMIM] [SCN].

Sl.No	Sample	IE (ev)	EA (ev)	χ(ev)	μ (ev)	ω (ev)	η (ev)	s
1.	PVA	40.386	0.0440	2.21	-2.21	1.13	2.17	0.23
2.	[BMPyr] [TFSI]	7.00	1.08	4.04	-4.04	2.76	2.96	0.16
3.	[EMIM] [SCN]	8.17	0.28	4.22	-4.22	2.25	3.94	0.126
4.	PVA/[BMPyr] [TFSI]	8.823	1.26	5.04	-5.04	3.36	3.78	0.132
5.	PVA/ [EMIM] [SCN]	8.119	1.40	4.76	-4.76	3.37	3.35	0.148

2.6.5. NLO properties

Table 11. The calculated dipole moment μ (Debye), the polarizability α_{tot} of PVA, [BMPyr] [TFSI], [EMIM] [SCN], and their polymer composites PVA/[BMPyr] [TFSI] and PVA/ [EMIM] [SCN].

Sl. No	Sample	Dipole moment (Debye)	α_{xx}	α_{yy}	α_{zz}	α_{tot} x 10^{-24} (esu)
2	[BMPyr] [TFSI]	15.5780	118.7628	153.0201	125.7807	196.1314
3	[EMIM] [SCN]	11.5017	99.63988	193.5383	30.65181	159.7561
4	PVA/[BMPyr] [TFSI]	17.6554	-172.03	-212.07	-216.35	515.6175
5	PVA/ [EMIM] [SCN]	12.7016	-77.959	-1288.8	-134.07	1921.185

As the DFT methods were highly recommended for the study of organic molecules, the same can be used for computing the total molecular dipole moment (μ), linear polarizability (α), and first-order hyperpolarizability (β) of such molecules to evaluate their nonlinear optical property (73). The electronic dipole moment μi, polarizability α_{ij}, and the first hyperpolarizability β_{ijk} of PVA-based ionogel membranes (PVA/[BMPyr] [TFSI] and PVA/[EMIM] [SCN]) were calculated at QM and hybrid QNIQM level and were listed in Table 5 and Table 6.

The quantum mechanical descriptors in Table 10 revealed that PVA/[BMPyr] [TFSI] and PVA/[EMIM] [SCN] exhibit a remarkable

nonlinear response. The calculated polarizability α_{ij} had non-zero values and was dominated by the diagonal components, while the hyperpolarizability β dominated by the longitudinal components of β_{xxx}, β_{xxy}, β_{xyy}, and β_{yyy}. It is found that although PVA/[BMPyr] [TFSI] has a dominating dipole moment, PVA/[EMIM] [SCN] exhibited higher polarizability and first-order polarizability compared with the PVA/[BMPyr] [TFSI]. This may be due to the high reactivity of [EMIM] [SCN] even after trapping it in the PVA matrix, which is well evidently discussed in section 2.4.2. The dipole moment of [BMPyr] [TFSI] is 15.5780 Debye while that of [EMIM] [SCN] is 11.5017 Debye; in a similar manner, the polarizability of [BMPyr] [TFSI] is 196.1314×10^{-24} esu and that of [EMIM] [SCN] is 159.7561×10^{-24} esu. Though the crucial nonlinearity determining factor, (β) is high for [BMPyr] [TFSI], the freedom obtained by [EMIM] [SCN] in PVA matrix after immobilizing plays a crucial role in determining the polarizability and hyperpolarizability values.

Table 12. The calculated first hyperpolarizability β_{tot} of [BMPyr] [TFSI], [EMIM] [SCN], and their polymer composites PVA/[BMPyr] [TFSI] and PVA/ [EMIM] [SCN].

Sample	β_{xxx}	β_{xyy}	β_{xzz}	β_{yyy}	β_{yzz}	β_{yxx}	β_{zzz}	β_x 10^{-30} (esu)
[BMPyr] [TFSI]	101.783	1.9993	20.271	1.5985	-0.2971	-22.588	-13.95	1.164
[EMIM] [SCN]	103.561	29.9169	10.909	6.907	11.088	5.9468	-15.58	1.267
PVA/[BMPyr] [TFSI]	57.7386	-57.82	-82.147	71.59	18.6779	-2.5211	-1.077	1.14
PVA/ [EMIM] [SCN]	-35.12	56.6863	114.9752	20.4554	8.4864	51.6185	9.2264	1.40

However, when we compare the values of dipole moment, polarizability, and hyperpolarizability of two ILs and two polymer composites with that of the reference values of urea and p-nitroaniline, which is considered as a prototypical donor-acceptor organic molecules with large hyperpolarizability (67), it is interesting to note that both polymer composites exhibit nonlinear optical behavior higher than urea (α_{tot} = -8.88×10^{-24} esu, $\beta_{tot}=0.00518\times10^{-30}$ esu) and comparable to p-nitroaniline ($\beta_{tot}=11.464\times10^{-30}$ esu). Nevertheless, by considering the activity and stability, it is necessary to point out the nonlinear behavior of the PVA/[EMIM] [SCN] polymer composite, even it fails to unveil the optical property in the UV and visible region.

2.7. Conclusion

In this chapter, a detailed quantum mechanical investigation on ionogel membranes was narrated with its theoretical backgrounds. The main aim of this work was to find the most compatible ionic liquid among the two most conductive ILs for two polymer matrices, namely PVA and PMMA. Here DFT-level calculations in conjunction with a new hybrid ONIOM-level approach were used to trace out the most compatible one. The detailed discussion of the thermochemical properties and global descriptive parameters emphasized that though [BMPyr] [TFSI] is the most stable and reactive IL, with a large spatial orientation due to the lengthy alkyl chains, it is not a suitable dopant for both matrices. [BMPyr] [TFSI] is very compatible with PMMA, as it has comparatively high ionization energy to form a strong enough nature with higher chemical stability. However, it exhibited a good amount of strong intermolecular hydrogen bonding, and it has higher reactivity with a better electrophilicity index. The inbuilt optical property in PMMA gave a substantial contribution to the optical and nonlinear optical properties of the PMMA/[BMPyr] [TFSI] ionogel membrane.

At the same time, [EMIM] [SCN] showed better compatibility with PVA than the other. Though the hardness values are slightly lessened for PVA/[EMIM] [SCN], it showed a better electron-accepting capacity indicating the free availability of ions in the matrix. Such availability of free ions will be favorable for the charge transport mechanism and will make the membrane viable for the use of a solid polymer electrolyte in energy storage devices.

Thus the theoretical prediction helped us trace out the two most compatible ionogel membranes from the four possible combinations. Thus, further experimental investigations will center on these two, PMMA/[BMPyr] [TFSI] and PVA/[EMIM] [SCN] ionogel membranes, by remembering to reduce the limitations of the chemical and preserve the environment.

CHAPTER 3

MORPHOLOGICAL AND STRUCTURAL CHARACTERIZATION

3.1. Introduction

One interesting and challenging task is to have a deep understanding of the morphology of the ionogel membranes. The ionogel membranes were developed as a result of modification of the non-conducting polymers with ionic liquids. Ionic liquids exhibit outstanding thermal stability, ionic conductivity, and non-volatility, thus making them a promising filler in the polymer matrix. At the same time, the polymer matrix acts as a platform to immobilize the ionic liquids. However, the formed binary system offers many interesting characteristics based on their morphology and the interaction between the IL and the polymer matrix. An increase in the concentration of the ILs usually results in a transition from a non-conducting to semiconducting state at threshold concentration. In recent years, interest in the industry is increasing drastically in using ILs in the non-conducting polymers due to their eco-friendly nature. It is always difficult to discover a good de-agglomerated membrane with a well-defined interface with a threshold concentration.

In the same way, it is always a challenge to discover the mode of chemical bonding between the doped IL and the polymer matrix: whether it is covalent, ionic, or Vander Waal. These morphological changes can completely change the properties, especially the crystallinity, electrical, and thermal properties and therefore must be considered. Building up the structure-property relation of ionogels with varying concentrations of doped IL can be analyzed using different experimental techniques. This chapter elaborately discusses the chemical and structural characterization of the ionogel membranes using different experimental techniques like a scanning electron microscope (SEM), X-ray diffraction (XRD) studies, Fourier transforms infrared spectroscopy (FTIR), and Fourier transforms Raman spectroscopy (FT-Raman).

3.2. Scanning electron microscope

The name of the scanning electron microscope (SEM) implies that a beam of focused electrons are used in a raster scan pattern to scan the surface of the sample (74). The SEM method provides the surface and morphology patterns of the synthesized membranes in this work. It can also provide vague information about whether the dopant is just trapped or is miscible in the polymer host matrix.

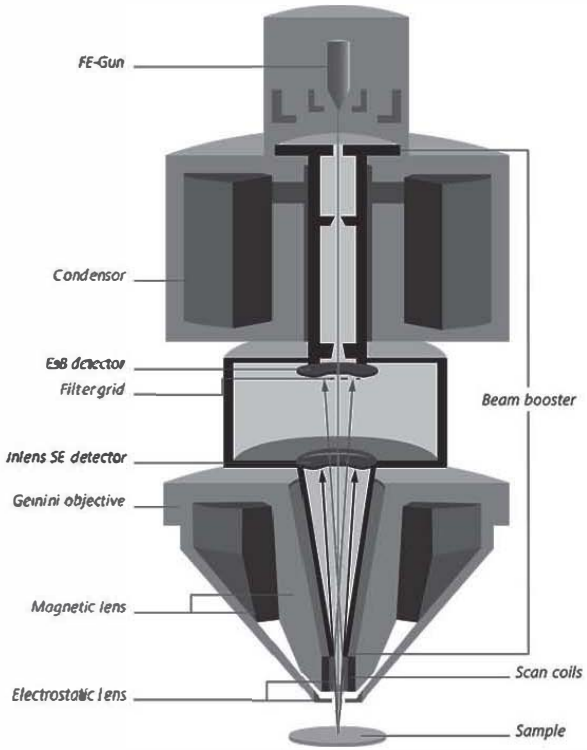

Figure 15. Ray diagram of scanning electron microscopy (75).

Typically in SEM, a focused mono-energetic electron beam is impinged on a specimen surface and is scanned back and forth. To obtain signals from a part, the electron beam is scanned over the specified region by two pairs of electromagnetic deflection coils, and the signals are transferred from point to point, and the signal map of the scanned area is displayed on a screen. Backscattered electrons and secondary electrons are

exploited for SEM application that can be collected individually by the detectors and can be utilized to obtain information. The intensity of the electrons depends on the atomic number of the host atoms. The signals derived from electron-sample interactions provides information regarding the external morphology (texture), chemical composition, and crystalline structure and orientation of materials making up the sample [Figure 15]. Data are collected over a specified region of the surface of the specimen, and a two-dimensional image is formed that shows spatial variations in these properties. Areas ranging from approximately 1 cm to 5 microns in width can be imaged in a scanning mode and can provide magnification up to 30,000 times. There is no particular sample preparation process except that for non-conducting samples gold sputtering is required to make it conductive. Field emission constitutes an advanced way of generating electrons.

In this work, a scanning electron microscope (SEM, SU6600HI-2102-0003) operated at an accelerating voltage of 5 KV was used to observe the immiscible ILs and grain boundaries at the microscopic level. The specimens were sputter-coated with a thin gold layer before imaging in order to prevent charging of specimens and to increase the signal to noise ratio. The SEM images of neat polymers, PMMA and PVA, along with their ionogels were shown in Figure 16.

Although the computational results pointed out that PMMA is compatible with [BMPyr] [TFSI], while PVA is compatible with [EMIM] [SCN] ionic liquids respectively, two unique, controversial images were obtained from the SEM for the above mentioned two ionogel membranes. The SEM studies showed that even though all ionogels are entirely amorphous, [EMIM] [SCN] was found to be immiscible in PVA while [BMPyr] [TFSI] was miscible in PMMA without any boundaries and particles. These SEM images lead to the conclusion that [BMPyr] [TFSI] was completely assorted to the PMMA matrix, but [EMIM] [SCN] IL is just entrapped in the PVA matrix. PMMA/ [BMPyr] [TFSI] ionogels have a fairly smooth surface and lack a visible boundary between [BMPyr] [TFSI] and PMMA matrix emphasizing the complete miscibility of [BMPyr] [TFSI] in the polymer matrix; the detailed report of all concentrations was already published (14). The wrinkled pattern in Figure 16.d confirms the instability and integrity of PVA/[EMIM] [SCN] film.

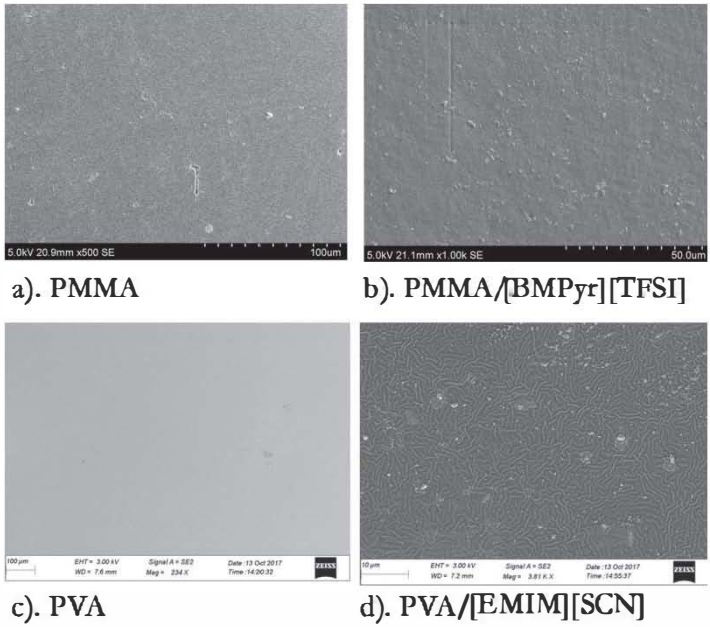

Figure 16. SEM images of polymers at 100 micrometers and ionogels at 50 micrometers.

These results were in good agreement with the optimized geometry of ionogel film. The quantum mechanical calculations showed that PMMA/[BMPyr] [TFSI] had an intermolecular hydrogen bond between the trapped IL [BMPyr] [TFSI] to form a miscible compatible ionogel. On the other hand, the theoretical calculation of PVA/[EMIM] [SCN] revealed that the lack of intermolecular hydrogen bonding between PVA and [EMIM] [SCN], which accentuates that the IL is just entrapped in the PVA matrix without any additional bond breakage or bond formation.

3.3. X-ray diffraction

Characterization of the local molecular order has vital importance in understanding the chemical and physical stability of any materials. The x-ray diffraction pattern is considered as an elementary tool to distinguish crystalline, semi-crystalline, and amorphous materials. The schematic diagram of the X-ray diffractometer is shown below.

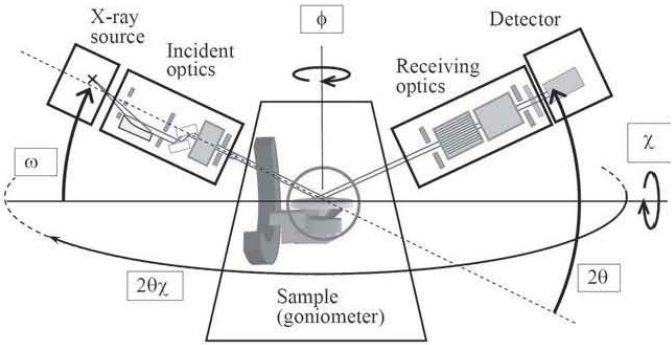

Figure 17. Ray Diagram of X-Ray Diffractometer (76).

In an X-Ray diffractometer, the incident X-ray beams interact with the planes of atoms, allowing a few to transmit through and the rest to refract and diffract. Depending upon the phase of oscillation of the electron cloud, destructive as well as constructive interference will be produced. In crystals, the constructive interference will be in a few directions, depending upon the spacing between parallel planes, the wavelength of X-ray angle of incidence using Bragg's law

$$n\lambda = 2d\sin\theta$$

where θ is the angle between the incident rays and the scattering plane, λ, is the wavelength of incident radiation, which is generally CuK_α 1 (1.54056Å) and CuK_α 2 (1.5444Å). The detailed discussion on the crystalline peaks in XRD and their analysis is very much outside the scope of this work since the samples dealt with here are purely non-crystalline.

Glassy materials are merely one among thousands of examples of solid-state systems that give rise to X-ray amorphous powder patterns. Any non-crystalline solid or liquid with a lack of long-range order will give rise to an X-ray amorphous powder pattern. In semi-crystalline polymers, it is possible to determine the crystalline and, conversely, amorphous orientation.

Here, XRD patterns of two polymer-based ionogel electrolyte membrane were recorded using an X-ray diffractometer (Rigaku powder diffractometer) with CuK_α radiation (λ=1.5418 Å) in the Bragg angle (2θ) range from 10 to 60°. Accordingly, the XRD pattern is shown in Figure 18.

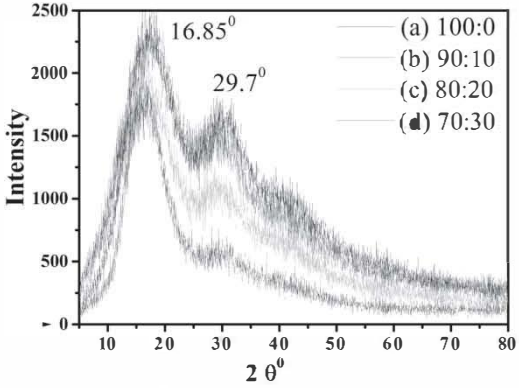

a). PMMA/[BMPyr][TFSI] ionogel with different weight ratio

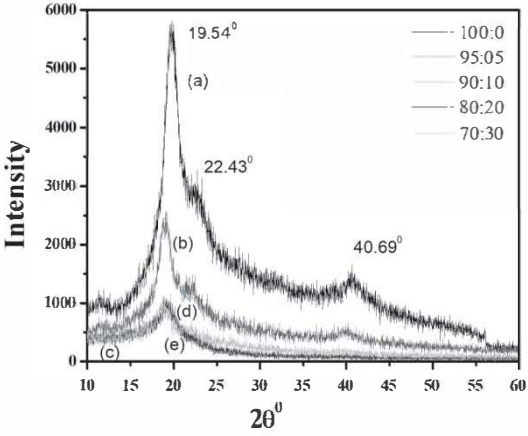

b). PVA/[EMIM][SCN] ionogel with different weight ratio

Figure 18. X-ray powder diffraction pattern of a) PMMA/[BMPyr] [TFSI] ionogels b) PVA/ [EMIM] [SCN] ionogels at different weight ratios.

It is interesting to note that on the addition of ionic liquids to both polymers PMMA as well as PVA, the membrane losses their semi-crystalline nature and gradually attains amorphocity. In this work, XRD is used to investigate the change in crystalline structure in terms of degree of crystallization, orientation, crystal size, lattice strain, etc. of the polymer matrix.

The XPRD patterns of both polymers revealed their semi-crystalline nature with the presence of a broad crystalline peak at 26–33° while dominating the amorphocity at 14–21° for neat PMMA, while the PVA film showed a semi-crystalline peak at around 2θ = 19.54° and a shoulder at 22.43°, along with a small broad peak at 40.69° as shown in Figure 18(a, b). The literature review shows that PMMA has a double-stranded helices structure with reflections from (101) and (200) planes.

The intensity of the diffraction peak of both polymers decreases with the incorporation of respective ILs to the matrix. As the weight ratio of IL increases, a decrease in intensity and an increase in width of the diffraction crystalline peak of the pure polymer was observed, which indicates the decrease in the percentage of crystalline and increased amorphosity of the polymer composite membrane. The relative variation in the crystallinity can be monitored by a relative crystallinity index, which is calculated as follows.

The relative crystallinity index was calculated with the equation

$$\chi_c = \frac{I_f - I_s}{I_f} \times 100\%$$

where χ_c is the crystallinity index, I_f is the intensity of the fundamental peak, and I_s intensity of the secondary band (77). A correlation has been established between area, width, the intensity of the peak, and the degrees of crystallinity which was reported by Safna et al. (14, 78).

3.4. Vibrational analysis

The vibrational frequencies and spectrum of each molecule are taken to be a unique characteristic feature of the molecule. Once the information about the functional group is deduced, one is able to infer the local orientation of the group of the structure. Subsequently, the origin of the sample, their prehistory, and the characteristic behavior of the sample will help us correlate with the output results. For such analysis and interpretation, Fourier transform-infrared spectroscopy and Fourier transform-Raman spectroscopy are considered as a tool to identify the fingerprint of the samples (79).

3.4.1. Fourier transform infrared spectroscopy

Fourier transform-infrared spectroscopy (FTIR) is an analytical tool used to spot the organic or inorganic functional groups in the unknown sample quantitatively for the analysis of solids, liquids, and gases. The basic principle behind FTIR is that every molecular bond, depending upon the elements and types of bonds, vibrates at unique frequencies. This technique used to measure the absorption of infrared radiation by the sample material versus wavelength. According to quantum mechanics, these absorbed frequencies correspond to certain molecular vibration (80). The essential condition to show the IR spectrum of a molecule is that the vibrating motion of the bond must change in their dipole moment with time. The schematic diagram for FT-IR spectroscopy is shown below.

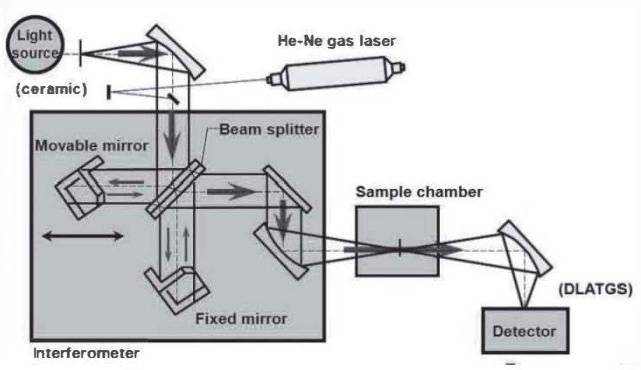

Figure 19. Ray Diagram of FT-IR Spectroscopy (75).

The infrared radiation is allowed to fall on a beam splitter in which their 50% will reflect and the rest will transmit through towards a moving mirror and will again reflect the mirror. At the same time, the reflected beam moves towards the mirror is and then reflected back to the beam splitter. Thus the detector can detect two beams simultaneously with an interference pattern—either constructive interference or destructive interference, depending upon the position of the moving mirror. This can be analyzed by scanning the sinusoidal signal from the moving mirror for a specific frequency over a range. The corresponding Fourier spectrum is computed from the obtained interferogram within a fraction of seconds.

According to quantum mechanics, these absorbed frequencies correspond to certain molecular vibrations (80). But these techniques fail for some materials including films, rubber sheets, etc.; in such situations

experimentalists prefer attenuated total reflection (ATR).

ATRFTIR spectroscopy is normally utilized in conjunction with FTIR to examine directly in the solid or liquid state without further preparation with Potassium bromide (KBr). ATR-FTIR spectroscopy uses the advantage of total internal reflection resulting in an evanescent wave (80). Thus, ATR-FTIR spectroscopy was used to get evidence of doped ionic liquids in the host PMMA and PVA polymer matrix. Here, the vibrational information of ionogel was collected using the ATR-FTIR spectra of the ionogel films, which were recorded by the JASCO spectrometer at ambient temperature. The measurements were carried out in the wave number range from 400 to 4000 cm^{-1} (14). The spectra were recorded from loaded ionogel films of PMMA/[BMPyr] [TFSI] and PVA/[EMIM] [SCN] with wt/wt% a) 100:0 b) 90:10 c) 80:20 d) 70:30. The recorded ATR-FTIR spectra for the PMMA/[BMPyr] [TFSI] ionogel with different weight ratios were shown in Figure 20.

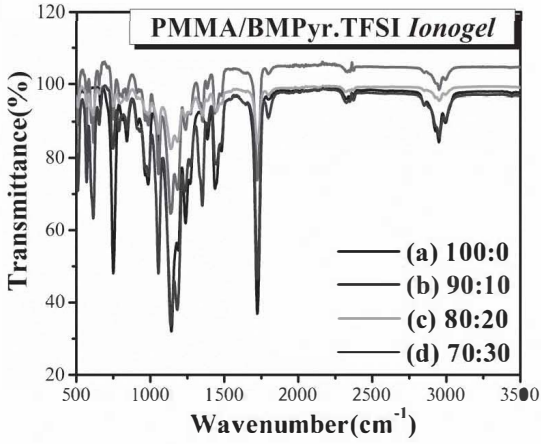

Figure 20. The vibrations of the ionogels PMMA/[BMPyr] [TFSI] wt/wt% a) 100:0 b) 90:10 c) 80:20 d) 70:30 obtained from ATR-FTIR.

The PMMA/ [BMPyr] [TFSI] ionogel films that retain the absorption bands of isotactic PMMA in all weight ratios exhibit their characteristic peaks at 751 cm^{-1} corresponding to C-H bending, 841 cm^{-1} corresponds to C-C bending/ alkenes, 985 cm^{-1} corresponds to C-C bending/alkene, 1238 cm^{-1} corresponds to C-O Stretching/Alkyl aryl ether, 1386 cm^{-1} corresponds to the C-H bending/aldehyde group, 1436 cm^{-1} corresponds to C-O

stretching, 1723 cm ^{1} corresponds to C=● stretching/ α,β-unsaturated ester, and finally 2951 cm ^{1} corresponds to CH stretching/ alkane groups. Similarly, the presence of [BMPyr] [TFSI] ionic liquid was confirmed from the presence of a band centered on 512 cm ^{1}, 569 cm ^{1}, and 616 cm ^{1}, which corresponds to TFSI anion, and the band at 1055 cm ^{1} confirms the presence of cation with S=● characteristic peak.

The addition of IL decreased the intensity of all these peaks and showed some additional peaks at 512-560, 610, and 653-655 cm^{-1}, which as it corresponds to $TFSI^-$ anion indicates the presence of IL in the ionogel membrane. The out-of-phase vibrations of $S●_2$ were seen at 1350–1352 cm^{-1}, while the SNS vibration of $TFSI^-$ were observed at 749 cm^{-1}. The bands seen at 2580–3200 cm^{-1} are because of the chelate hydrogen holding emerging from being entombed and additionally intra hydrogen holding between the PMMA and [BMPyr] [TFSI]. The lack of the presence of vibration corresponding to the C=● functional group of PMMA helps us decipher that the ionogel was shaped by the interaction of [BMPyr] [TFSI] and the PMMA was shaped by variable hydrogen bonding without any additional bond breakage or bond formation (14). The characteristic peaks and their assignments were tabulated in Table 12. The harmonic vibrations of the ionogels were in good agreement with the computational results. Detailed discussion on its scaling and assignments were already discussed in Chapter 2.

Similarly we explored the possible interaction between the [EMIM] [SCN] ionic liquid and PVA host matrix in the compatible PVA/[EMIM] [SCN] ionogel using ATR-FTIR spectroscopy. Figure 21 exhibits the characteristic absorption bands of ionogel films of [EMIM] [SCN] wt/wt% a) 100:0 b) 95:05 c) 90:10 d) 80:20 e) 70:30. The characteristic bands of all ionogel films retain the presence of PVA polymer by exhibiting absorption where 827 cm^{-1} corresponds to C=C bending/ alkenes, 915 cm^{-1} corresponds to CH_2 stretching, 1085 cm^{-1} corresponds to C-● Stretching/ Alkyl aryl ether, 1386 cm^{-1} corresponds to C-H Bending/ aldehyde group, 1413 cm^{-1} corresponds C-● Stretching, 1643 cm^{-1} corresponds to C=● stretching /α, β-unsaturated ester, and finally 2918 cm^{-1} corresponds to CH Stretching/ Alkane groups (68).

Table 13. Harmonic vibrations of ionogel films PMMA/[BMPyr] [TFSI] wt/wt% a) 100:0 b) 90:10 c) 80:20 d) 70:30 obtained from ATR-FTIR and their assignments.

Wavenumber (cm^{-1}) 100:0	Wavenumber (cm^{-1}) 90:10	Wavenumber (cm^{-1}) 80:20	Wavenumber (cm^{-1}) 70:30	Assignments
	512	511	511	TFSI anion
	569			TFSI anion
	616	615	615	TFSI anion
750	749	749	748	C-H Bending
841	839	839		C=C Bending/ Alkenes
985	986	985	986	C=C Bending/ Alkene
	1055	1054	1054	S=O Stretching
1142				C-O Stretching
	1181	1181	1181	S=O Stretching
1238	1136	1139	1137	C-O Stretching/ Alkyl aryl ether
	1352	1351	1350	out of phase vibrations of SO2
1386				C-H Bending/ Aldehyde group
1436	1435	1438	1449	C-O Stretching
1723	1721	1723	1724	unsaturated ester
2949	2952	2953	2952	chelate hydrogen bonding

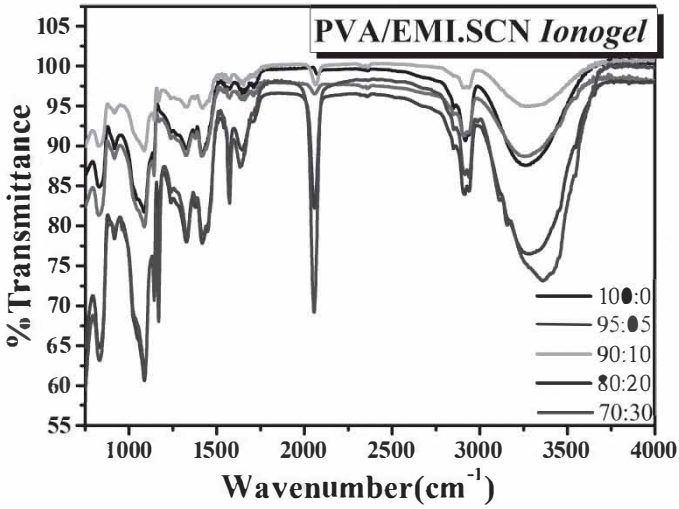

Figure 21. Vibrations of the ionogel films PVA/[EMIM] [SCN] wt/wt% a) 100:0 b) 95:05 c) 90:10 d) 80:20 e) 70:30 obtained from ATR-FTIR.

The presence of [EMIM] [SCN] ionic liquid was solely confirmed from the characteristic band where 1169 cm^{-1} and 2064 cm^{-1} relate to the C=N and SCN^- anion respectively, and it was interesting to note that on increasing the concentration of IL the intensity was found to increase (14, 69–72).

Table 14. Harmonic vibrations of ionogel films PVA/[EMIM] [SCN] wt/wt% a) 100:0 b) 95:05 c) 90:10 d) 80:20 e) 70:30 obtained from ATR-FTIR and their assignments.

Wave Number (cm^{-1}) 100:0	Wave number (cm^{-1}) 90:10	Wave number (cm^{-1}) 80:20	Wave number (cm^{-1}) 70:30	Assignments
828	827.6	827.6	827.6	C=C bending/ alkenes
916	915	915	915	CH_2 vibration
1085	1085	1085	1085	C-O stretching/ alkyl aryl ether
		1169	1169	C=O Stretching
1326	1324	1324	1324	C-H bending/ aldehyde group
1415	1413	1413	1413	C-O stretching
1643	1575	1575	1575	C=O stretching /α,β-unsaturated ester
	2064	2064	2064	SCN- anion
2918	2918	2906	2906	CH stretching/ alkane groups
3264	3257	3266	3266	hydrogen bonding

3.4.2. Fourier transform Raman spectroscopy

Fourier transform Raman spectroscopy (FT-Raman) is considered to be a complementary tool to Fourier transform-infrared spectroscopy for vibrational analysis of a molecule. FT-Raman is also used to identify the specific functional groups in a molecule or compound; furthemore, it yields more information about certain types of organic functional groups, where its fingerprint is absent in FTIR counterparts. Fourier transform Raman spectroscopy is thus considered to be an excellent diagnostic tool for the identification of organic species. While IR vibration arises from the absorption of the electromagnetic radiation in the IR region under a change in the electric dipole moment that originates from the molecular vibrations, without a doubt, the Raman scattering spectrum bears a resemblance to the infrared absorption spectrum quite closely (79).

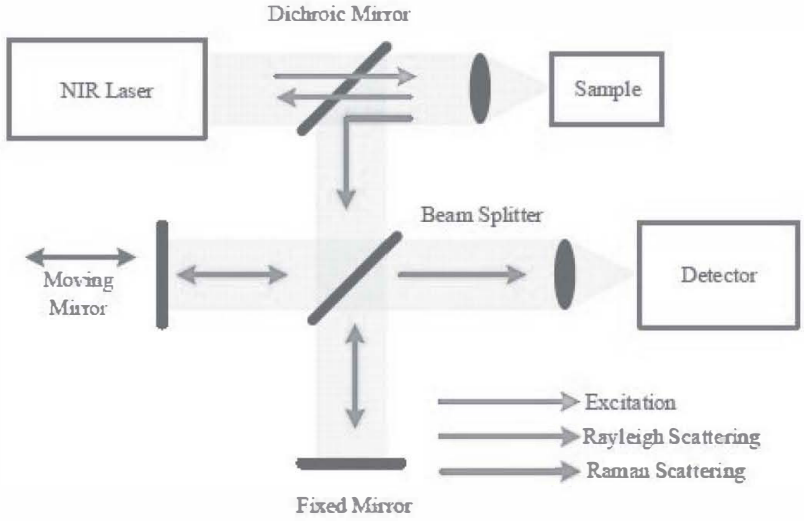

Figure 22. Ray diagram of FT-Raman spectroscopy (76).

The fundamental vibrations of Raman scattering were recorded between region 3500 and 50 cm^{-1} on a Bruker FRA 106/S FT-Raman instrument using 1064 nm excitation from an Nd: YAG laser. The detector used was a liquid-nitrogen-cooled Ge detector.

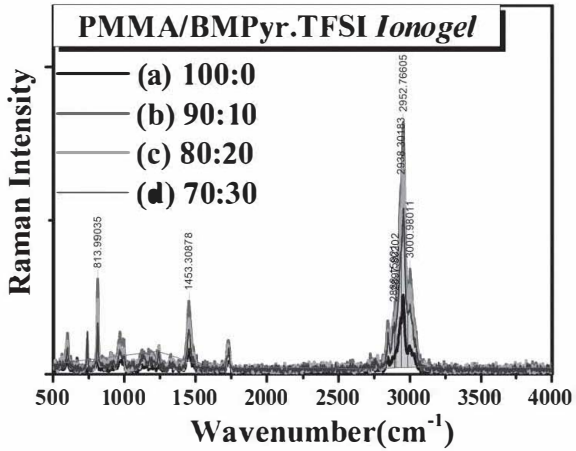

Figure 23. Harmonic vibrations of ionogel films PMMA/[BMPyr] [TFSI] wt/wt% a) 100:0 b) 90:10 c) 80:20 d) 70:30 obtained from FT-Raman.

The FT-Raman spectrum of PMMA/ [BMPyr] [TFSI] ionogel films show chelate hydrogen bonding at 2952 cm^{-1}, where 1453 cm^{-1} corresponds to C-H stretching, and 813 cm^{-1} corresponds to the C = C bending/alkenes. These characteristic peaks were already observed from FTIR spectroscopy.

Table 15. Harmonic vibrations of ionogel films PMMA/[BMPyr] [TFSI] wt/wt% a) 100:0 b) 90:10 c) 80:20 d) 70:30 obtained from FT-Raman and their assignments.

Wavenumber (cm^{-1}) 100:0	Wavenumber (cm^{-1}) 90:10	Wavenumber (cm^{-1}) 80:20	Wavenumber (cm^{-1}) 70:30	Assignments
813	813	813	813	C=C is bending/alkenes
1453	1453	1453	1453	C-H stretching
2952	2952	2952	2952	chelate hydrogen bonding

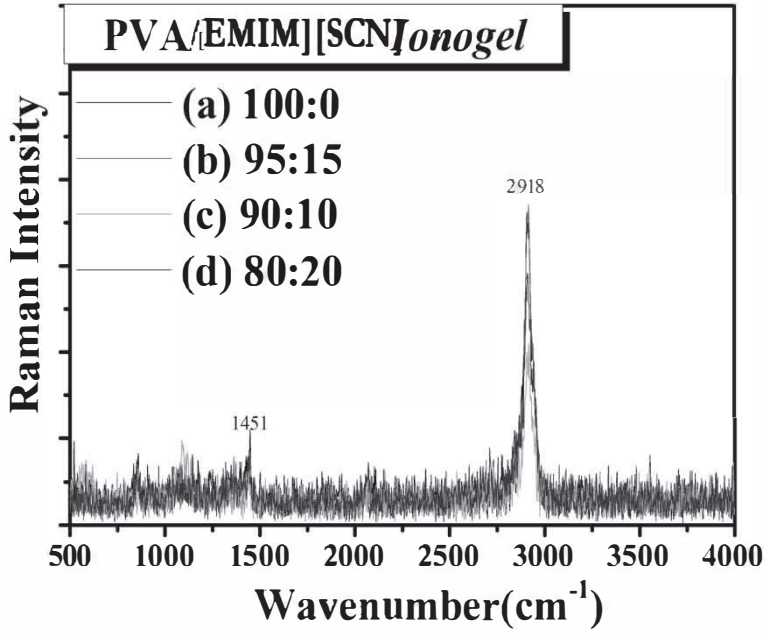

Figure 24. Harmonic vibrations of ionogel films PVA/[EMIM] [SCN] wt/wt% a) 100:0 b) 95:05 c) 90:10 d) 80:20 obtained from FT-Raman.

The FT-Raman spectrum of PVA/[EMIM] [SCN] ionogel films exhibited only two peaks, one at 2918 cm^{-1} indicating the moisture content in the film and the other at 1451 cm^{-1} that corresponds to C-H Stretching.

3.5. Conclusion

The presence of entrapped ILs in the polymer matrix and the influence of the concentration of the IL in the polymer matrix is confirmed from the vibrational analysis. The morphological characterization revealed that the incorporation of ionic liquid in the polymer matrix decreases their semi-crystalline nature and amorphocity was gradually attained. Subsequently, the relative variations in the crystallinity were monitored on the addition of ionic liquid in it. Although the addition of two ILs resulted in entirely different morphology due to their variation in chemical bonding, the addition of [BMPyr] [TFSI] resulted in a miscible ionogel without any visible boundaries at the same time the entrapment of [EMIM] [SCN] resulted in an immiscible ionogel with the wrinkled pattern. Thus, as the IL varies, the way of interaction between the guest and host becomes unpredictable, and it even affects the morphological pattern of the ionogels. Indeed, the wet crack-free wrinkled pattern in the free-standing solid polymer electrolyte may have wide applications like anti-corrosion coatings, sensors, and superhydrophobic surfaces and further can be used for functional device fabrications too.

CHAPTER 4

THERMAL BEHAVIOR OF IONOGELS

4.1. Introduction

Materials with a tailored property applicable for everyday use are of great relevance and importance in the current research arena. This is achieved by judicious turning of diverse and versatile properties including electrical, thermal, magnetic, and optical properties of a material. Among these, the thermal properties of the electrolyte membrane are significant, because they are allied with the response of an ionogel membrane to the heat supplied. This response might change the physical and chemical properties of the ionogel leading to a change of length or volume, phase transition, initiation of chemical reactions, including oxidation, reduction, thermal degradation, etc. Thus, temperature is an important factor for characterizing material performance.

In this chapter, various thermal properties including phase transitions (first and second order), chemical reactions, thermal stability, and degradation are investigated using various calorimetric techniques. Thermal analysis, such as differential scanning calorimetry (DSC) and thermal gravimetric analysis (TGA) are frequently used to describe the behavior of a polymer composite as a function of temperature. Moreover, thermal investigations are of particular interest in polymers and ionogel membranes because they provide detailed information on the molecular level interactions between the host and the guest and their miscibility (81).

4.2. Differential scanning calorimetry

Differential scanning calorimetry (DSC) is used to reveal first and second order thermal transitions like melting (Tm), crystallization (Tc), and glass transition (Tg) phenomena.

The differential scanning calorimetry (DSC) is a versatile and powerful tool to analyze the thermal behavior of the materials over a wide temperature. The DSC is used to determine the temperature, heat flow, enthalpy, and specific heat associated with all endothermic (heat absorption)

and exothermic processes (heat evolution) of the materials during different phase transitions including melting, crystallization, glass transitions, oxidation, water loss, and other heat-related changes. A schematic diagram of a typical DSC is shown below.

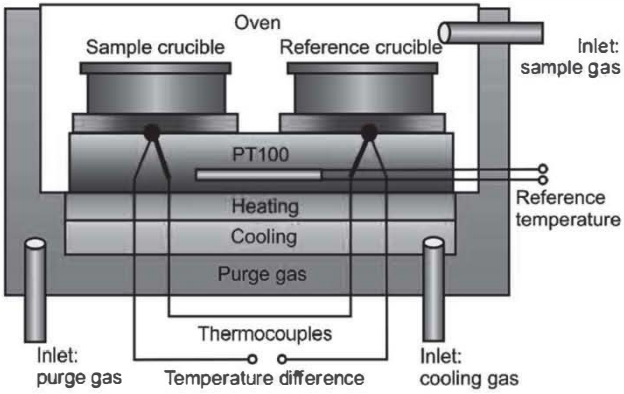

Figure 25. Schematic representation of differential scanning calorimeter (82).

In a typical DSC, the sample and reference pans were heated simultaneously at the same rate from a single heating source. The difference between the temperatures of the pans was precisely recorded as the power difference against the temperature and time. Subsequently, the heat difference is calculated from the power difference (76).

$$\Delta P = \frac{\Delta Q}{dt}$$

Here, the DSC was used to investigate the effects of ionic liquid on the thermal and crystallization behavior of the host polymer matrix. DSC thermograms of both ionogel membranes exhibited only a single glass transition temperature and found to decrease as the IL concentration increases. The thermograms of PMMA/[BMPyr] [TFSI] were shown in Figure 26. The Tg of pure PMMA is noticed at 342 K as a sharp endothermic event. The addition of [BMPyr] [TFSI] resulted in a shift of the transition temperature to lower temperatures, and the peaks were broadened with lower values of the change of specific heat (ΔCp). This fascinating change may be ascribed due to the formation of hydrogen

bonding between the [BMPyr] [TFSI] and PMMA matrix, which was further verified from FTIR spectra. The slight decrease in ΔCp at Tg on doping of the IL emphasizes the increase in the flexibility and fragility of the developed membranes.

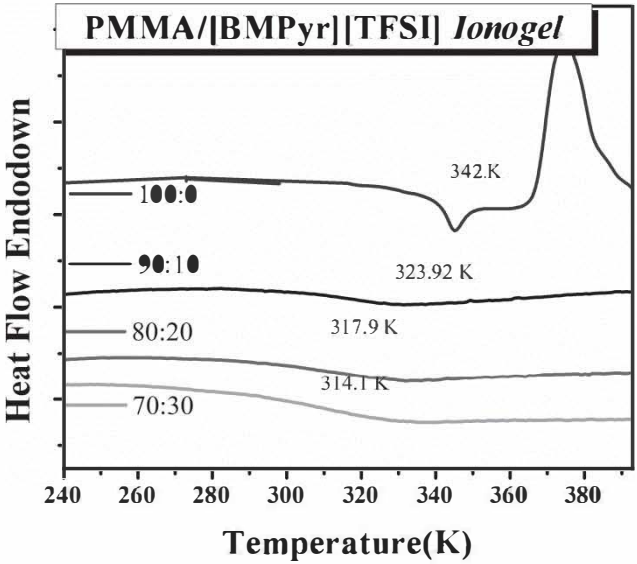

Figure 26. Thermograms of prepared ionogel membranes PMMA/[BMPyr] [TFSI] wt/wt% a) 100:0 b) 90:10 c) 80:20 d) 70:30 using differential scanning calorimetry.

At the same time, the addition of IL in the PVA matrix may break transient coordination bonds between charge carriers, especially the cation and oxygen from hydroxyl group in PVA and thus alter the interactions between PVA chains resulting in a shift in all phase transitions towards the lower temperature side (11, 83–86). In the neat PVA, the broad endotherm at around 373 K, attributed to the evaporation of water, masked the glass transition. By taking the onset value of the endotherm at 358 K as Tg of PVA, the subsequent sharp endotherm at 475 K is attributed to the melting. The addition of [EMIM] [SCN] to these two peaks were shifted to lower temperatures with a decrease in the heights emphasizing the plasticizing effect of [EMIM] [SCN].

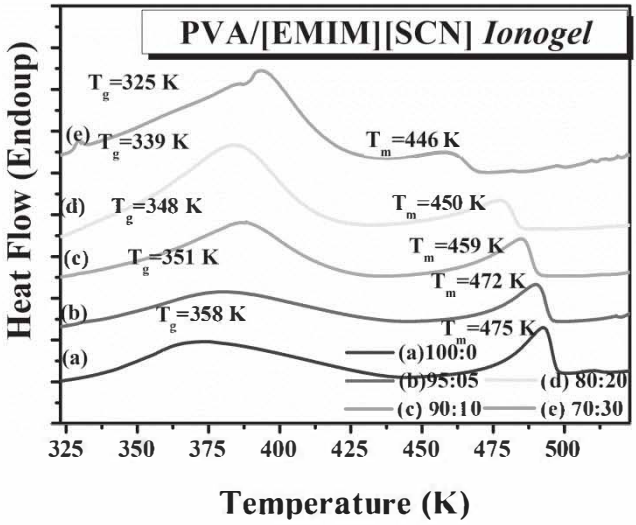

Figure 27. DSC thermogram of SPE, PVA/[EMIM] [SCN] wt/wt% a) 100:0 b) 95:05 c) 90:10 d) 80:20 e) 70:30.

Thus the glass transition peaks, crystallization, and melting temperatures of all the films were systematically shifted to lower temperatures as the concentration of IL is increased.

4.2.1. Correlation between experimental values and theoretical predictions of Tg

In reality, there is no precise glass transition temperature for polymers and their blends, only their glass transition region, since the phase transition from the liquid to glass or rubbery state is a gradual process. Even the values of Tg are indeed useful for a variety of purposes; no sophisticated experimental tool is available to trace the precise Tg values of such polymer blends though different experimental techniques leading to different Tg values. In this situation, analytical equations were developed from theoretical considerations for deducing the Tg as the function of the concentration of the dopant if the Tgs of both parent compounds is accurately known. Here we are taking the advantage to correlate the experimental values with the theoretical predictions (87).

Several attempts had already been made to find the Tg(x) of the blend. Initially, Fox (88) developed an equation for binary systems as follows:

$$\frac{1}{Tg} = \frac{x_1}{Tg_1} + \frac{1 - x_1}{Tg_2}$$

where Tg corresponds to the glass transition temperature of the polymer blend, Tg_1 corresponds to the Tg of the pure polymer matrix, and x_1 is their mass (weight) fraction, x_2--1-x_1 points out the weight proportion of the dopant and Tg_2 is the Tg of the dopant. Subsequently, Gordon Taylor (89) came up with introducing a new parameter and modified the above equation as follows:

$$Tg = \frac{x_1 Tg_1 + K_{GT}(1 - x_1)Tg_2}{x_1 + K_{GT}(1 - x_1)}$$

where $K_{GT} = \frac{Tg_1}{Tg_2}$ has to be supplimented from the experimental data, which represents the unequal contributions of components to the blend.

According to Coushman Karaz (90), the glass transition of the blend can be predicted using the equation,

$$Tg = \frac{x_1 Tg_1 + K(1 - x_1)Tg_2}{x_1 + K(1 - x_1)}$$

where $K = \frac{\Delta Cp2}{\Delta Cp1}$ has to be traced out from experimental data (91, 92).

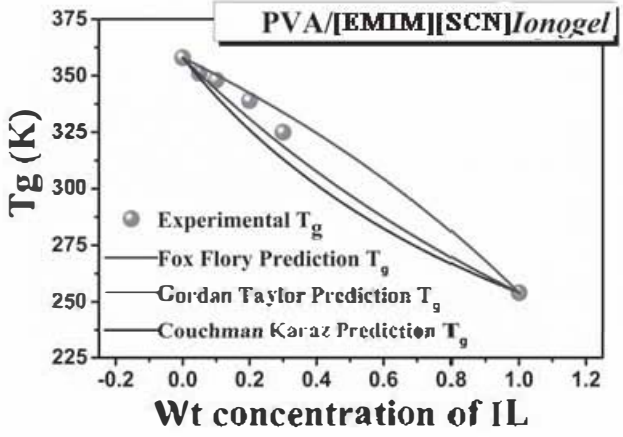

Figure 28. Theoretical prediction versus experimental values of PVA/[EMIM][SCN] membranes.

Figure 28 depicts the experimental values of Tg along with the theoretical predictions; the data deviates from all three equations. Deviations may be ascribed as the immiscibility of IL in the PVA matrix. It is worth perceiving that the predictions were obtained from mathematical manipulations of Tgs of parent compounds with the weight ratios without any flexible parameters for fitting. However, experimentally observed Tg composition profiles differ from the predictions obtainable from the general expression set for immiscible compositions. For such crucial situations, modifications were further developed by Jenkel and Heusch by proposing an expression accommodating monotonic deviations (positive or negative) from the linear combination (93).

$$Tg = x_1 Tg_1 + (1 - x_1)Tg_2 + kx1(1 - x_1)$$

where k is the fitting parameter. Kwei (94) came up with an additional parameter q evaluating from the experimental data and modified the equation as follows:

$$Tg = \frac{x_1 Tg_1 + K_{KW}(1 - x_1)Tg_2}{x_1 + K_{KW}(1 - x_1)} + qx1(1 - x_1)$$

The origins of the Kwei expression are empirical, and the physical meaning of the parameters k and q had been a subject of subsequent interpretations correlating with the intermolecular interactions between the mixture components.

4.3. Thermal gravimetric analysis

Thermal gravimetry analysis (TGA) measures the heat flow and weight loss in a sample and records various thermal events as a function of temperature or time. It is an effective method for investigating changes in physical and chemical properties due to various thermal events including absorption, desorption, water loss, vaporization, sublimation, oxidation, reduction, decomposition, and degradation. Here, the TGA thermograms were used along with their first derivatives (DTGA) to study the thermal behavior of all developed ionogel membranes for crucial monitoring of their thermal characteristics and degradations. The basic technique used in a TGA is their thermobalance. The schematic diagram of the TGA instrument is shown below

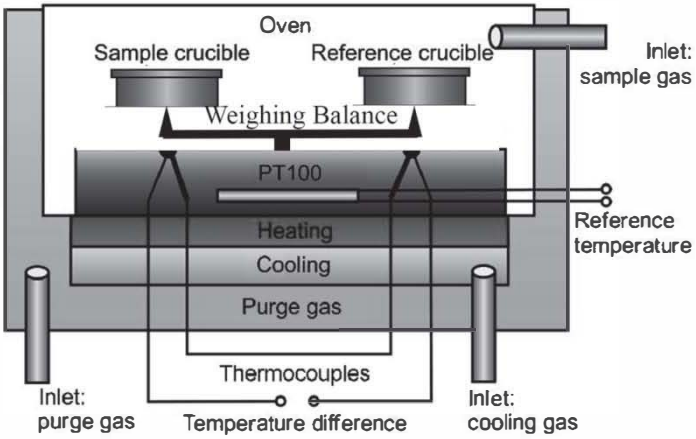

Figure 29. Schematic representation of Thermal Gravimetric Analysis.

TGA consists of a sample pan and a reference pan kept in a furnace that is supported by a weighing balance. A purge gas of N_2 is applied to make the sample environment inert to prevent unwanted reactions. The change in mass and temperature is monitored during the analysis.

The DTGA thermograms of all ionogel membranes were shown in Figure 31 and Figure 33. Initially, it was observed that all the ionogel membranes exhibited a weight loss in the range of 333 to 400 K due to their evaporation. All PMMA/[BMPyr] [TFSI] ionogel membranes showed stability up to 723 K and showed weight loss on further heating. The initial 9% mass loss in pure PMMA around 373 K, may be ascribed to the degradation of the polymer fraction formed by head-to-head linkage (95).

The above degradation in the neat PMMA can be suppressed by the addition of a small fraction of propylene carbonate (PC) that penetrates to the host PMMA initiating molecular-level mixing and stabilizes the domain against degradation (65). However, the addition of PC does not make any variation to the degradation temperature of the blend or their onset from the host, which is at ~673 K. The higher thermal stability of [BMPyr] [TFSI] increases the thermal stability of the ionogel membrane upon their addition. Thus the incorporation of [BMPyr] [TFSI] bypasses the complete degradation of PMMA and increases their stability by 100 K.

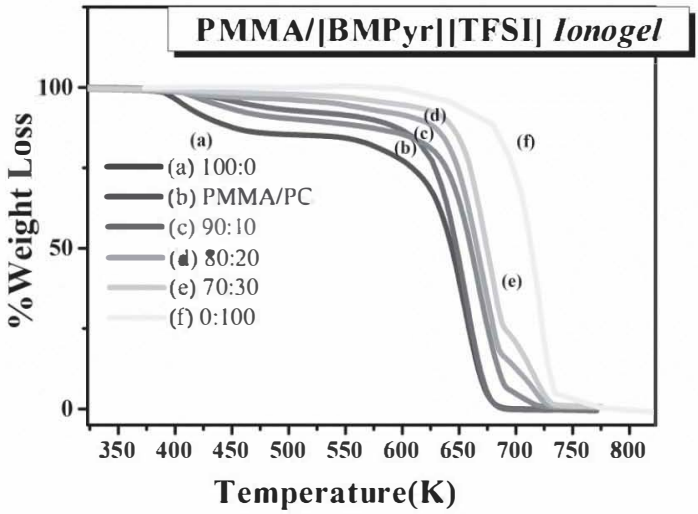

Figure 30. Thermograms of prepared ionogel membranes PMMA/[BMPyr] [TFSI] wt/wt% a) 100:0 b) PMMA/PC c) 90:10 d) 80:20 e) 70:30 f) 0: 100 using TGA.

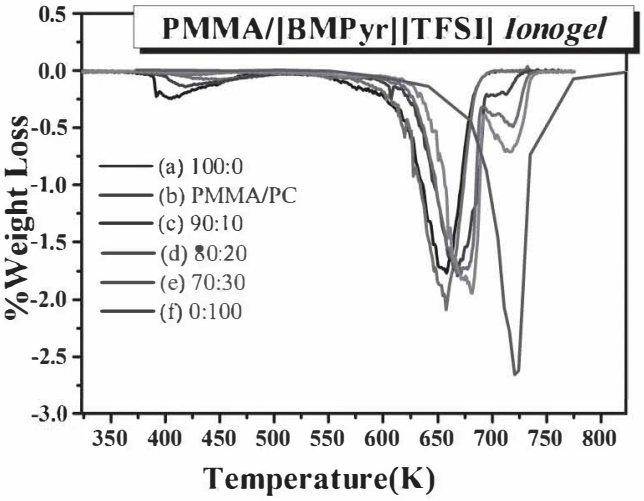

Figure 31. DTGA curves of prepared ionogels PMMA/[BMPyr] [TFSI] wt/wt% a) 100:0 b) PMMA/PC c) 90:10 d) 80:20 e) 70:30 f) 0: 100.

Contrary to [BMPyr] [TFSI], [EMIM] [SCN] is a less stable IL having stability up to 538 K. Similar to the previous case, initial weight loss is from the water loss originating from the hydrophilic nature of neat PVA. Later the complete degradation of the PVA film may be due to structural degradation. It is worthwhile noting that the increase in the degradation of PVA by the addition of IL is only by an increase of around 50 K from the host, which is around 575 K.

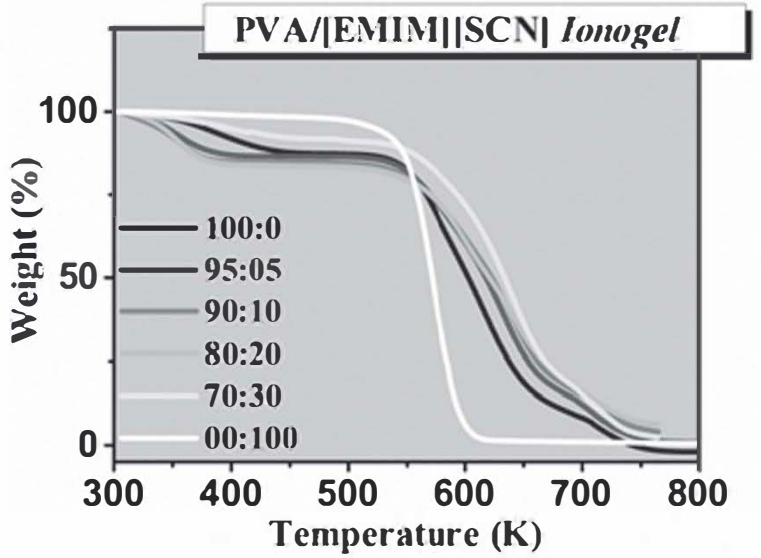

Figure 32. TGA thermograms for prepared ionogel membranes PVA/[EMIM] [SCN] wt/wt% a) 100:0 b) 90:10 c) 80:20 d) 70:30 e) 0:100.

It was amazing to note that just a drop of thermally stable IL enhances the thermal stability of the polymer matrix.

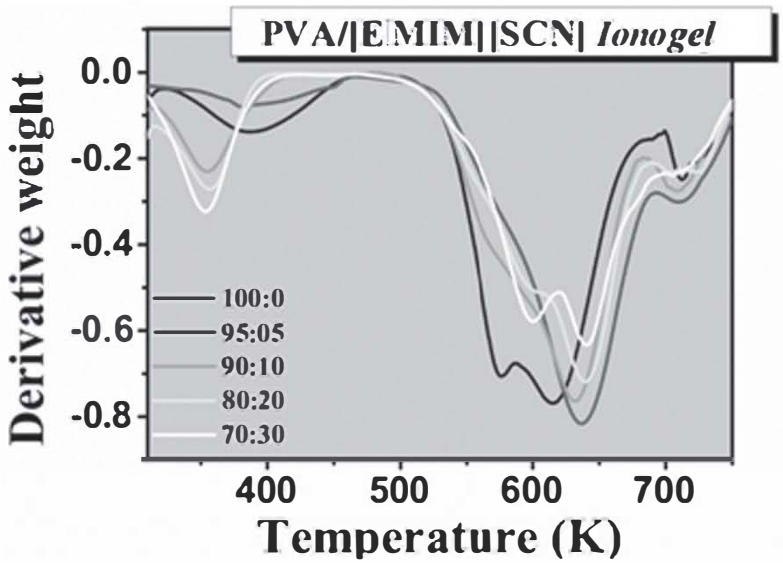

Figure 33. DTGA curves of prepared ionogels PVA/[EMIM] [SCN] wt/wt% a) 100:0 b) 95:05 c) 90:10 d) 80:20 e) 70:30.

4.4. Conclusion

In this chapter, DSC and TGA were successfully employed to explore the thermal characteristics and the stability of a couple of developers of ionogel membranes based on [BMPyr] [TFSI], [EMIM] [SCN] ionic liquids. From the results acquired, a deeper insight into elucidating the structural as well as chemical changes occurring in the addition of IL in the host polymer with different weight ratios was obtained. Thermal studies revealed that the incorporation of IL shifted all phase transitions of the host polymer to lower temperatures and the thermal stability was enhanced due to the plasticizing effect of IL and breakage of transient coordinate bonds in the polymer. Addition of IL induces further complications in the molecular structure of the host polymer and causes a gradual transition towards a more amorphous nature and the reduction in their semi-crystallinity index. It has been further noted that the doping concentration places a dominant role in both morphological and microstructural changes in the polymer matrix due to variations in the internal mechanisms. The XRD investigations correlate well with the

microstructural changes leading to the decrease in the semi-crystalline nature of the membranes. Thus, in summary, the DSC and TGA investigations revealed the miscibility between the host polymer and the doped IL and the induced morphological changes of the developed films and their thermal stability on doping.

CHAPTER 5

MOLECULAR DYNAMICS OF IONOGEL

5.1. Introduction

Broadband dielectric spectroscopy (BDS) has been widely used as a versatile tool to investigate molecular dynamics by probing rotational fluctuations of molecular dipoles, charge transport, and hopping of ions. By extracting the impedance data and analyzing the dielectric function, the composite information about the molecular ensemble and its dynamics can be deduced. This experimental technique helps us study the molecular motions on various length scales ranging from the fluctuations within a monomeric unit to the entire macromolecular level. Presence of dipoles is the prerequisite for the application of BDS to any system since the dipoles provide the link between the molecular motions and the interaction with an external electric field. This technique can be used to explore a wide variety of systems comprising monomers to polymers of different states, including solids, liquids, glasses, rubbers, etc. Developments during the last couple of decades have enabled this technique to explore the system in an extremely wide frequency window of about 15 decades in a single click to explore the dynamics at varying time scales by keeping the temperature/pressure constant.

Figure 34. Broadband dielectric spectroscopy (96).

This technique measures the complex impedance $Z(\omega) = Z'(\omega) + Z''(\omega)$ of the material in the form of a capacitor, with empty capacitance C_0, filled with the sample material as shown in Figure 35. Accurate measurements of electrode diameters (d) and sample thickness (l) are essential for accurate measurements of dielectric parameters (impedance, permittivity, conductivity, conductance, capacitance, etc.) (97).

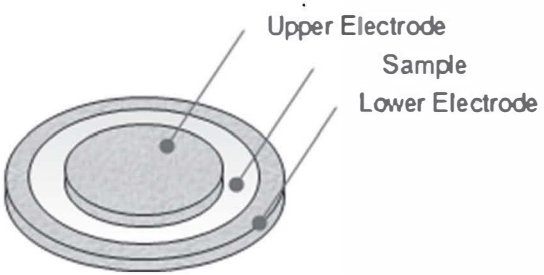

Figure 35. Schematic diagram of a capacitor with two gold plated electrodes.

A sinusoidal voltage $V_1(t) = V \times \exp(j\omega t)$ corresponding to a particular frequency ω is applied across the sample cell and the corresponding current $I_s(t) = V \times \exp(j\omega t + \phi)$ is precisely measured. Here, ϕ is the phase lag between the voltage and current that depends upon the frequency and the thermochemical properties of the sample. The schematic diagram of the circuit is shown in Figure 36.

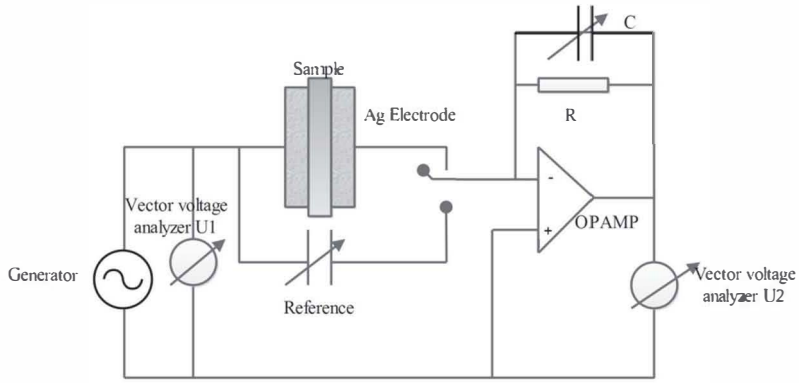

Figure 36. Schematic diagram showing the circuit of Broadband dielectric spectroscopy.

From the applied voltage and measured current, the value of complex impedance can be calculated using the following equation:

$$Z^*(\omega) = Z'(\omega) + jZ''(\omega) = \frac{V^*(\omega)}{I^*(\omega)}$$

Consequently, some parameters can be derived from the complex impedance, the parameters are as follows; the complex permittivity can be calculated from the complex impedance using the following equation:

$$\varepsilon^*(\omega) = \varepsilon'(\omega) - j\varepsilon''(\omega) = \frac{1}{j\omega C_0 Z^*(\omega)}$$

Permittivity is considered a vital material parameter that measures the degree to which the molecules of that material oppose the applied electric field. The permittivity of a material compared with the permittivity of a vacuum (no electrons present) is known as the relative permittivity or dielectric constant of that material. The following equation mutually interrelates the complex conductivity and the permittivity:

$$\sigma^*(\omega) = \sigma'(\omega) + j\sigma''(\omega) = j\omega\varepsilon_0\varepsilon^*(\omega)$$

The real part of the complex conductivity $\sigma'(\omega)$ relates to the electric charge flow of various spatiotemporal scales and roughly modeled with Johncher's power law (98):

$$\sigma'(\omega) = \sigma_0 + A\omega^s$$

where A is a constant and s is the power law exponent, 0<s<1. As the equation indicates, the conductivity is the contrary of the permittivity, where it measures the degree to which the molecules of the material favor the applied electric field. It is of two types: one due to free electrons, and the other due to hopping of ions. Conversely, it can even be classified as ac and dc conductivity, where the former depends on the frequency while the latter is independent of frequency. It may be kept in mind that all the three formalisms emphasize different facets of the same underlying mechanism and each representation may be preferred in appropriate cases to enhance clarity (99).

In the case of conducting materials; either ionic or electric, the dielectric loss spectra are dominated by dc conductivity towards low frequencies arising from the conductivity contribution of the ions. Subsequently, the information on the structural relaxation often is hardly observable. The corresponding information available from the real part of permittivity will be masked by the electrode polarization ("blocking electrodes") at the same time (100). In such crucial situations, modulus formalism can be used to overcome the problems above as given below.

$$M^*(\omega) = M'(\omega) + jM''(\omega) = \frac{1}{\varepsilon^*(\omega)}$$

The real and imaginary parts of M* can be interrelated to ε* through the following relations:

$$M'(\omega) = \frac{\varepsilon'(\omega)}{(\varepsilon'(\omega))^2 + (\varepsilon''(\omega))^2}$$

and

$$M''(\omega) = \frac{\varepsilon''(\omega)}{(\varepsilon'(\omega))^2 + (\varepsilon''(\omega))^2}$$

In this formalism, temperature-dependent peaks rise from translational ionic motions by suppressing the conductivity and electrode contributions. Correspondingly, in the modulus formalism, the peaks can be called at the conductivity relaxation time.

Though most of the polymers contain weakly polar groups, and ionic liquids contain inbuilt polarity, BDS can be preferred to study the

molecular dynamics of ionogel. This work is envisioned to investigate this notion in more detail; in this chapter, we are going to discuss the dielectric data of two polymers PVA and PMMA and the influence of entrapped IL on the molecular dynamics of the polymer matrix in modulus formalism. This chapter provides an overview of dielectric information about the nature, behavior, and analysis of the relaxation mechanisms and macroscopic charge transport phenomena in pure polymer membranes as well as in ionogel membranes.

5.2. Structural relaxation

The neat PMMA polymer film is rigid, brittle, and transparent with a smooth film surface. The main disadvantage of the PMMA film is their brittleness. The mechanical properties of the film can be altered by adding plasticizers like propylene carbonate. The conductivity behavior of PMMA is strongly dependent on the glass transition temperature. Relatively, PMMA has a very high glass transition temperature and low conductivity in the range of 10^{-10} S/cm.

The dielectric permittivity and loss of pure PMMA are shown in Figure 37. The dielectric constant, ε′, shows a strong frequency dependent behavior at lower frequencies gradually becoming frequency independent towards higher frequencies. This is because at high frequencies the dipoles are no longer able to follow the rapid fluctuations in the electric field and begin to lag behind the field (101). As the temperature increases, the frequency dependence of the dielectric constant also decreased in PMMA, due to its rigidity and lack of melt.

The dielectric loss spectra (ε'') of PMMA for selected temperatures from 263 K to 328 K were shown in Figure 37. Two relaxations are observed in the dielectric loss spectra, which linearly depend on temperature. Most probably these relaxations are the secondary relaxations of PMMA since the glass transition temperature of it is very high. It may be a very challenging and time-consuming effort to trace the α relaxation of pure PMMA. The observed two dipolar relaxations have a frequency dependence to the extent of the particular temperature range, beyond that the dependency decreases due to its rigid, brittle nature. One of the prominent secondary relaxation, β-process, may arise due to the stepwise rotation of the side chain around the carboxyl group along with a small angle wagging motion of smaller parts of the backbone chain (102) while that of vague γ– may be due to localized motions of ethyl units at the end of the alkyl group in the side chains of PMMA (14, 103).

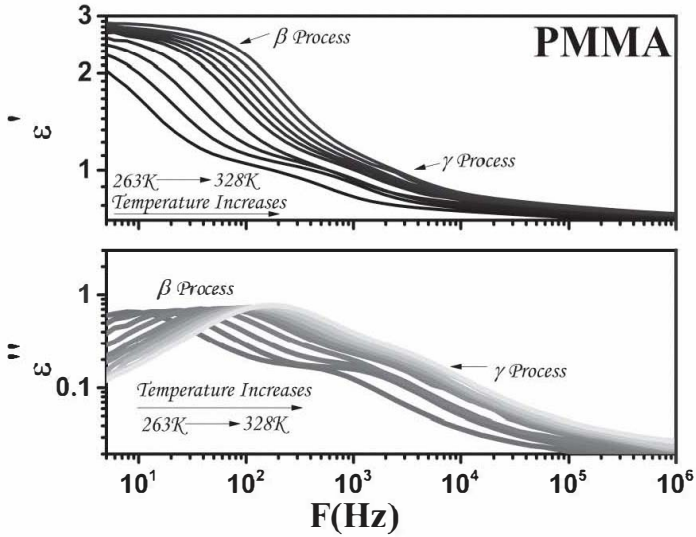

Figure 37. The real and imaginary parts of dielectric data of PMMA for selected temperatures.

In the case of neat PVA, only one relaxation is visible at lower temperatures; even that relaxation was gradually getting masked by the dc conductivity towards higher temperatures, which may be due to the hopping of –OH ions as well as electrode polarization. The real and imaginary parts of the permittivity of PVA for selected temperatures ranging from 263 to 373 were shown in Figure 38. The invasion of dc conductivity causes an abrupt increase in the dielectric constant of PVA. However, at high frequencies, the dielectric constant becomes frequency independent and attains nearly a constant value, since, at higher frequencies, the dipoles will no longer be able to respond to the rapid changes in the field, and subsequently, it will no longer be able to orient themselves in the direction of the applied field (101).

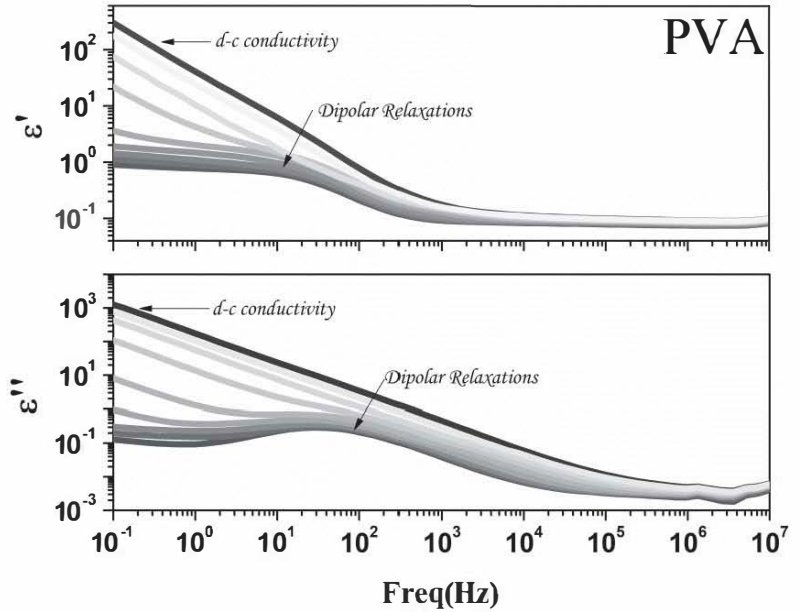

Figure 38. The real and imaginary parts of dielectric data of PVA for selected temperatures.

The addition of ILs in the polymer matrix increases the concentration of freely hopping ions and the dc conductivity masks the structural relaxation. Thus, it has no longer possible to single out the changes in the structural relaxation and study the dynamics. Hence, it is hardly worth pursuing the permittivity data of ionogels due to the hike in the dc conductivity at the lower frequency side of permittivity.

5.3. Conductivity relaxation

As discussed in the previous section, the structural relaxations of all ionogel membranes in the dielectric formalism were masked by the dc-conductivity aroused due to the hopping of doped ions in the membrane. In such crucial situations, modulus formalism will play a key role in analyzing impedance data and deducing the information about rotational and translational motions (104–106, 106–110). Modulus is nothing but the inverse of dielectric permittivity. $M^*\varepsilon^* = 1$ (111). The frequency dependent electric modulus M*(ω) is given as follows:

$$M^*(\omega) = \frac{1}{\varepsilon^*(\omega)} = M'(\omega) + jM''(\omega)$$

The real and imaginary parts of M* can correlate to the permittivity (ε*) through the following relations:

$$M'(\omega) = \frac{\varepsilon'(\omega)}{(\varepsilon'(\omega))^2 + (\varepsilon''(\omega))^2}$$

and

$$M''(\omega) = \frac{\varepsilon''(\omega)}{(\varepsilon'(\omega))^2 + (\varepsilon''(\omega))^2}$$

The main advantages of using modulus formalism are: large variations in the permittivity and loss at low frequencies and high temperatures are minimized; the electrode polarization effects can be neglected. They occur because of the difficulties that occur due to the electrode's nature, electrode–specimen contact, injection of space charges, and absorbed impurities (78). Since the modulus is independent of polarization P and does not make any assumption about the source impedance of the sine generator, it can be expressed and derived as follows:

$$M^*(\omega) = \frac{\varepsilon_0 E^*(\omega)}{D^*(\omega)} = \frac{i\omega\varepsilon_0 A/d}{I^*(\omega)/U^*(\omega)} = \frac{Z^*(\omega)}{Z\ (geometry)}$$

where $E^*(\omega)$ is the frequency dependent electric field, $D^*(\omega)$ is the dielectric displacement, $Z^*(\omega)$ is the frequency domain impedance that can be measured as $Z^*(\omega) = U^*(\omega)/I^*(\omega)$, in which $U^*(\omega)$ is the voltage across the capacitor, $I^*(\omega)$ is the current across the capacitor, and $Z\ (geometry)$ is the impedence of a disc capacitor of known geometry (112).

In this formalism, temperature-dependent peaks can be revealed by suppressing the contributions from the hopping of ions and electrode-electrolyte polarization effects. The relaxation time corresponding to the temperature-dependent peaks in modulus formalism can be called *conductivity relaxation time*. Although it was introduced initially by Macedo (113) and Moynihan (99) to study effects of space charge and their relaxation phenomena, M* representation is now extensively used to analyze the ionic conductivities (100, 105, 107, 112, 114–144). Consequently, all the data were depicted in the modulus formalism shown

in Figure 39 and Figure 40 and fitted with the Havriliak Nigami equation:

$$M^*(i\omega) = M'(i\omega) + iM"(i\omega) = \frac{1}{\varepsilon^*(i\omega)}$$
$$= M_\infty \left[1 - \int_0^\infty dt exp(-i\omega t)(-\frac{d\varphi}{dt})\right]$$

and can be written in its Fourier transform as

$$M *_{HN} (\omega) = M_\alpha + \frac{\Delta M}{(1 + (-i(\omega\tau_{HN})^{-1})^{1-\alpha})^\beta}$$

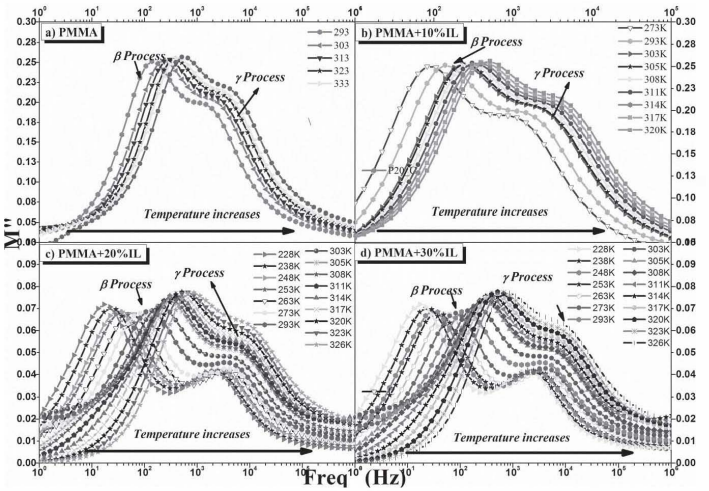

Figure 39. Conductivity relaxation in the modulus formalism obtained for the prepared ionogel membranes PMMA/[BMPyr] [TFSI] wt/wt% a) 100:0 b) 90:10 c) 80:20 d) 70:30.

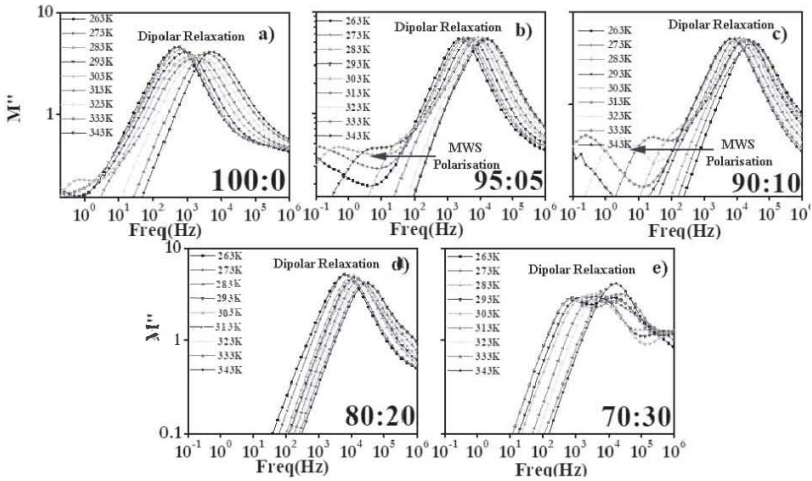

Figure 4**0**. Conductivity relaxation in the modulus formalism obtained for the prepared ionogel membranes PVA/[EMIM] [SCN] wt/wt% a) 1**00**:**0** b) 95:**0**5 c) 9**0**:1**0** d) 8**0**:2**0** e) 7**0**:3**0**.

When the data of PMMA/[BMPyr] [TFSI] is represented in the modulus formalism, only two relaxations were found in all films, as in pure PMMA. Thus the entrapment of IL in the PMMA matrix causes enhancement in the hopping of ions and does not make any further relaxations in the matrix. This is because [BMPyr] [TFSI] is miscible in PMMA, which is evidently observed from the SEM image and DSC results discussed in detail in chapters 3 and 4. The observed two relaxations linearly depend on temperature, which identifies them as secondary relaxations of PMMA, since it shows less shift towards higher frequencies on increasing temperature. Such temperature independent relaxation may be due to dipolar fluctuations produced due to the side chains of PMMA and confirms the lack of melt of the ionogel membrane.

However, the amalgamation of IL increases the temperature dependence of the relaxation resulting in a shift towards the higher frequency side compared to the neat polymer. This may be due to the increased thermal stability and decreased fragility of the film. Thus the plasticizing effect of [BMPyr] [TFSI] increases the freedom of hopping of ions by decreasing the viscosity of PMMA. It is observed that the relaxation spectra get more temperature dependent on adding ionic liquid into it, signifying the increased amorphocity and flexibility of the film.

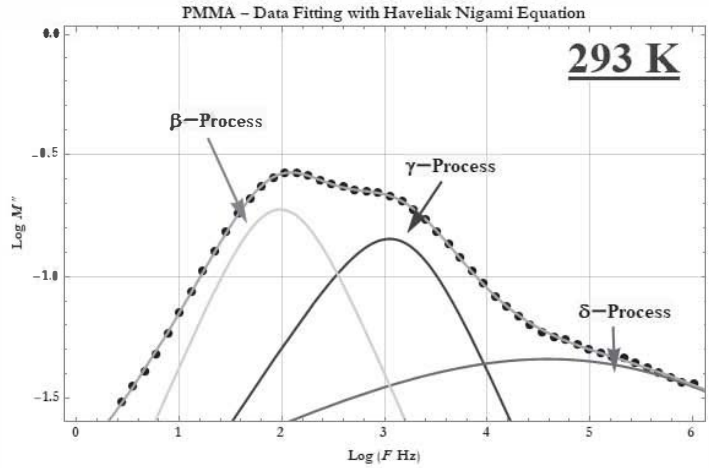

Figure 41. Different structural relaxation processes in the neat PMMA membrane in modulus formalism.

The addition of [EMIM] [SCN] IL in the PVA matrix increased the number of relaxations in the membrane in modulus formalism. Two relaxations can be seen in the spectra, one prominent relaxation found in all investigated concentrations at higher frequencies are ascribed to pure intrinsic dipolar relaxation due to the bulk polarization effect of PVA, while the second slow process seen in 95:05 and 90:10 weight ratios of PVA/[EMIM] [SCN] are attributed to interfacial polarization (IP) or the Maxwell-Wagner-Sillars (MWS) effect (84, 145). Thus at low temperatures, two sets of peaks are apparent, corresponding to bulk and interfacial polarization effect, respectively. Meanwhile, at the higher temperature region (Figure 40), only one set of the peak is obvious, corresponding to inter dipolar relaxation due to bulk polarization. This is because of the immiscibility of IL in the PVA matrix, where [EMIM] [SCN] is just entrapped in the host matrix without forming any additional bonds or its breakage. It is visible from the wrinkled patterns in the SEM image, where the IL flows like a lake in the PVA matrix and is not miscible as it is in the PMMA/[BMPyr] [TFSI] ionogel membrane. As the temperature increases, the viscosity of PVA decreases, which effectively reduces the dielectric boundary between the host and the dopant which in turn allows all the charge carriers to hop substantially at the same frequency. The same occurs with an increase in the concentration of the IL frequency of relaxation due to IP and bulk merge due to the plasticizing nature of [EMIM] [SCN].

Temperature dependence of the relaxation time

Introduction of ionic liquids in the polymer matrix facilitates the relaxation process to higher frequencies much more naturally. The variation of the characteristic relaxation time τ can be expressed by the well-known Arrhenius equation, given as follows:

$$\tau_{max} = \tau_{\infty} \exp\left(\frac{Ea}{KT}\right)$$

where the pre-factor τ_{∞} and the activation energy Ea are the governing parameters. The above equation relates to the relaxation time (τ_{max}) with the temperature (T). The temperature dependence of the conductivity relaxation times of PMMA/[BMPyr] [TFSI] ionogel membranes were shown in Figure 42.

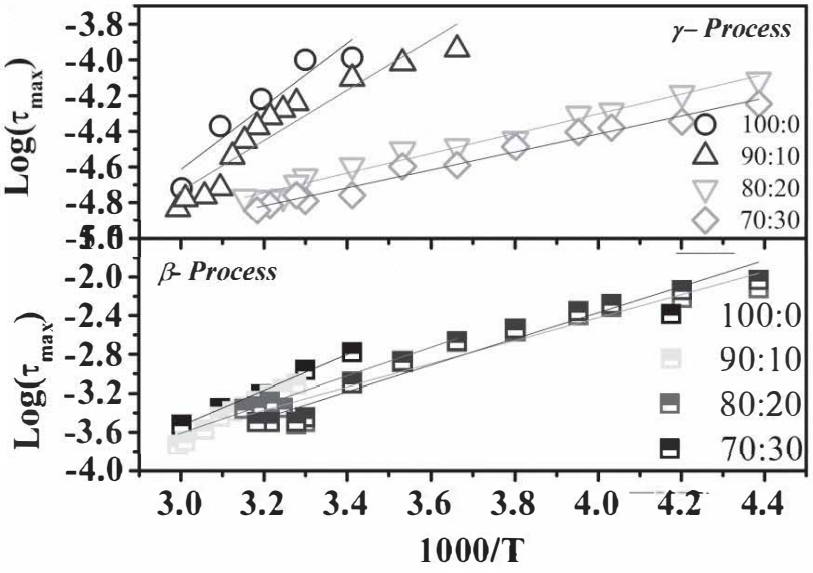

Figure 42. Logarithmic representation of relaxation time versus inverse temperature for different processes in PMMA/[BMPyr] [TFSI] membranes with various weight ratios.

It is found that the activation energies of all PMMA-based ionogel membranes decrease with the increase in temperature which is a standard

criterion for all ionic conductors (126). It is interesting to note that the activation energy decreases with the increase in the doping percentage of [BMPyr] [TFSI] until 20%, above which it is found to increase, signifying that it requires more energy to make the molecules free to undergo relaxation as well as the ions to hop in response to the applied electric field.

Table 16. Change in activation energy, Ea. and Log (τ_0) for various weight ratios of PMMA/[BMPyr] [TFSI] membranes

Sample PMMA/[BMPyr] [TFSI]	β- Relaxation		γ- Relaxation	
	Log (τ_0)	Ea(eV)	Log (τ_0)	Ea(eV)
100:00	-9.01127	00.362	-9.93224	0.352
90:10	-8.01771	00.292	-8.9768	0.281
80:20	-7.1822	00.236	-6.51859	0.110
70:30	-7.79179	00.269	-6.43401	0.10

Similar behavior is observed for PVA/[EMIM] [SCN] ionogel membranes. The activation energies of all ionogel membranes decreases with an increase in temperature as mentioned above (126). As in the case of a PMMA-based ionogel, the activation energy decreases with increases in the concentration of [EMIM] [SCN] up to a concentration of 20% IL, above which some hindrance is caused for charge transport due to the accumulation or agglomeration of excess ions in the host matrix. The temperature dependence of the conductivity relaxation times of PVA/[EMIM] [SCN] ionogel membranes was shown in Figure 43, and the fitting parameters, activation energy, and log (τ_0) for various weight ratios of the membranes were tabulated in Table 17.

Table 17. Change in activation energy, Ea and, Log (τ_0) for various weight ratios of PVA/[EMIM] [SCN] membranes

Samples PVA/[EMIM] [SCN]	Ionic conductivity bulk polarization		Ionic conductivity interfacial polarisation	
	Log (t_0)	Ea(eV)	Log (t_0)	Ea(eV)
100:00	-7.85	0.234		
95:05	-7.7705	0.185	-24.7859	1.35
90:10	-7.44781	0.149	-24.9694	1.34
80:20	-7.42622	0.148		
70:30	-8.30317	0.256		

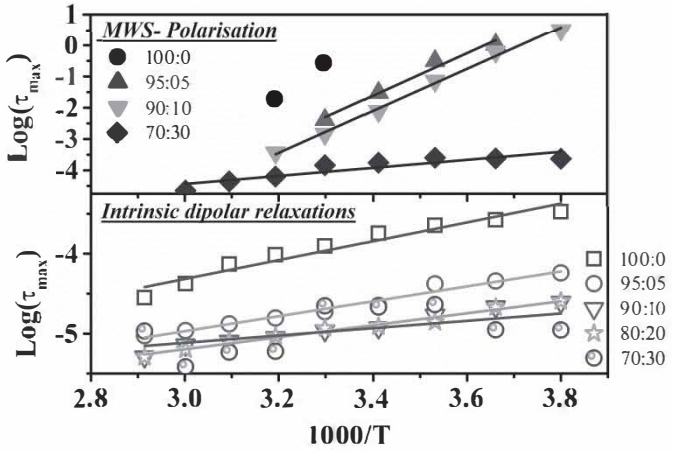

Figure 43. Logarithmic representation of relaxation time versus inverse temperature for different processes in PVA/[EMIM] [SCN] membrane with various weight ratios.

5.4. Conclusion

Broadband dielectric spectroscopy was successful in investigating the molecular dynamics of PMMA/[BMPyr] [TFSI], PVA/[EMIM] [SCN] ionogel membranes over a wide frequency range for selected temperatures. The polymer matrices PVA and PMMA were initially explored to understand the behavior of the host platforms. It was found that PMMA film has two to three observable secondary relaxations, which were comprehended from the dielectric data itself. Meanwhile, the PVA has only a single relaxation visible within the experimental window, which is masked by the dc-conductivity at higher temperatures. The incorporation of IL in the polymer resulted in impressive improvements in their mechanical and electric properties. The heterogeneity in their morphology greatly influences their charge transport mechanism; the addition of [BMPyr] [TFSI] in PMMA increases the flexibility with a strong temperature dependence on the relaxation. The addition of [EMIM] [SCN] in PVA gives rise to wrinkled patterns in the ionogel causing additional pathways for charge transport mechanism from interfacial polarization. The temperature dependence of the conductivity relaxations revealed that the ionogels with 20% IL concentration yielded minimum activation energy with superior performance to project these to be the optimum concentration for practical applications.

CHAPTER 6

CONDUCTIVITY STUDIES

6.1. Introduction

Broadband dielectric spectroscopy can also be used as an ideal tool to explore the charge transport mechanism due to translational diffusion of charge carriers and hopping of ions in a conducting system. It covers a broad frequency range over 10^{-2} to 10^{7} Hz with widely varying temperature. Thus this technique is suitable for investigating molecular and collective fluctuations, charge transport, and polarization effects at inner and outer dielectric boundaries of the material being studied for both electrical and non-electrical applications (146, 147). BDS dominates other dielectric experiments because other experimental techniques were either limited to high or low frequencies and thus fail to capture conductivity dynamics precisely in a limited temperature range. The charge transport mechanism can be explored in detail from complex conductivity since it is due to the translational diffusion of the charge carriers in a conducting system. It is a well-known fact that the complex impedance plot consists of two regions: a semicircular arc in the high-frequency region and a straight line incline concerning the real axis in the low-frequency region (84). The arc at high frequencies is allied to the conduction process, and the straight line at a lower frequency is correlated to electrode/electrolyte interfacial properties (84). The conductivity of the ionogel membranes was calculated from the measured resistance, area and thickness of the polymer film using the following equation:

$$\sigma = \frac{Gl}{A}$$

where A is the area of the gold plated electrodes (cm^2) as shown in Figure 35, l is the thickness (cm) of the membranes, and G is the conductance of the film, which can be expressed as follows:

$$G = \frac{1}{R_b}$$

where R_b, the bound resistance can be measured from the Nyquist plot.

As mentioned in chapter 5, the conductivity and the complex permittivity of the samples are mutually correlated as follows:

$$\sigma^*(\omega) = \sigma'(\omega) + j\sigma''(\omega) = j\omega\varepsilon_0\varepsilon^*(\omega)$$

The real part of the complex conductivity σ′ (ω) relates to the electric charge flow of various spatiotemporal scales and is roughly termed in terms of Johncher's equation (98).

$$\sigma'(\omega) = \sigma_0 + A\omega^s$$

where A is a constant and n is the power law exponent, 0<s<1.

In this chapter, the response of the developed ionogel membranes to the applied electric field were investigated in a broad frequency and temperature range. Subsequently, this study unravels the role of doped IL in the host polymer matrix on quantities such as dc conductivity, diffusion of dielectric boundaries, and viscosities. When the information elucidated from BDS is used in conjunction with other techniques, such as current-voltage response, a wealth of information about charge transport, translational diffusion, and gradual transformation of non-conducting polymers towards semiconducting behavior upon IL addition can be explored.

6.2. Nyquist Plot

The typical impedance plots (Z' vs. Z'') for ionogel membranes were drawn in the name of Nyquist plots, to unfold the impedance behavior of the membranes at room temperature (303 K).

In general, the obtained complex impedance from BDS for ionogel membranes consists of two well-defined regions: one semi-circle in the higher frequency range corresponds to the conduction process and, second, a spike in the low-frequency region attributed to the effect of interfacial polarization between the IL and the polymer matrix. The diameter of the semi-circle in the higher frequency indicates the bulk resistance (R_2). Once the bulk resistance is known, we can calculate the conductivity of the membranes using the relation,

$$\sigma = \frac{L}{AR_2},$$

where L is the thickness of the sample, and A is the electrode area, respectively.

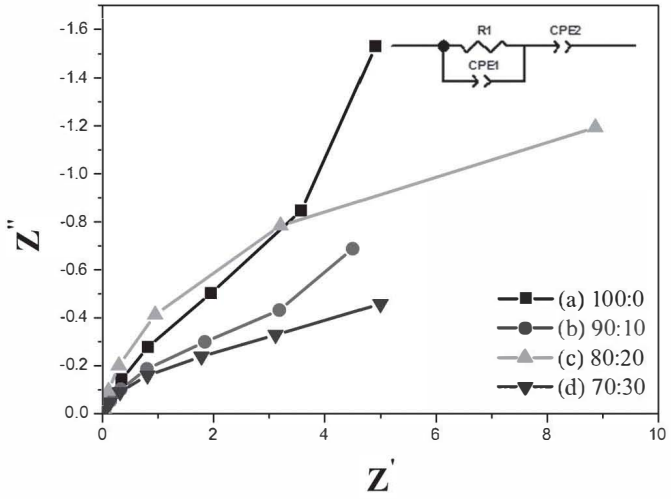

Figure 44. Nyquist Plot obtained for prepared PMMA/[BMPyr] [TFSI] ionogel. The inset shows an equivalent electric circuit used to model the impedance curve in which CPE1 is the geometrical capacitance of electrolyte, CPE2 is the capacitance of the double layer formed at the electrode-electrolyte interference, and R is resistance.

The PMMA/[BMPyr] [TFSI] ionogel had one small semi-circle and a long spike as shown in Figure 44, while that of PVA/[EMIM] [SCN] had a major semi-circle with a small spike in the low-frequency side, as depicted in Figure 45. This contrary behavior may be credited to the morphological difference of the ionogel membranes. In PMMA-based membranes the doped ionic liquid [BMPyr] [TFSI] was chemically bonded with the PMMA to form a miscible transparent ionogel membrane, while that of PVA/[EMIM] [SCN], the trapped IL, is just entrapped in the PVA matrix without any additional bond breakage and formation. This discrepancy caused the formation of a dielectric boundary between the IL and PVA matrix nurturing to form a dominant semi-circle in the Nyquist plot.

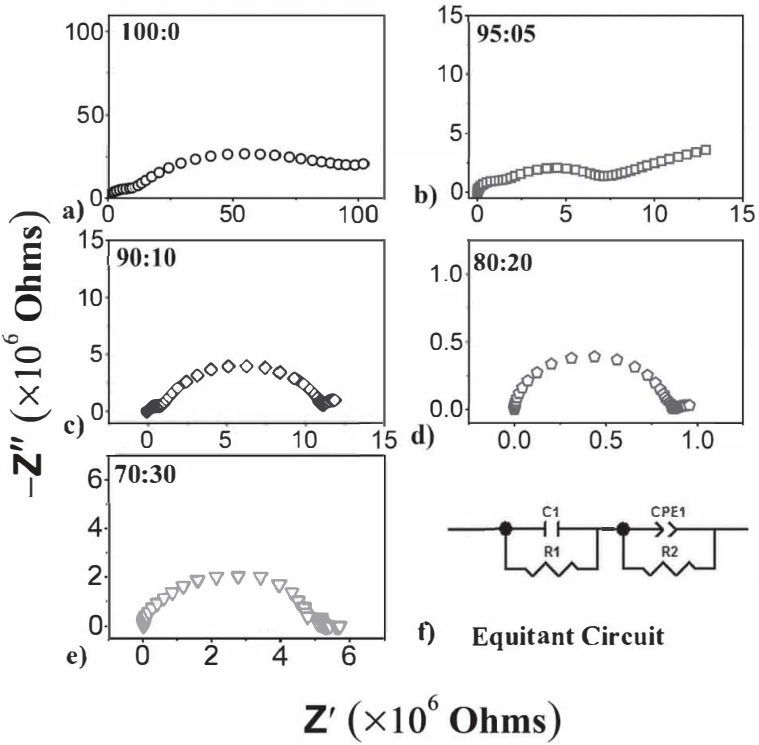

Figure 45. Nyquist Plot obtained at room temperature (303K) for PVA/[EMIM] [SCN] SPE membranes a) 100:0 b) 95:05 c) 90:10 d) 80:20 e) 70:30 f) equitant circuit.

The impedance behavior of the ionogels was fitted using Zview software with an equivalent circuit as shown in the inset scheme in Figure 45. For PMMA/[BMPyr] [TFSI], one tank circuit with additional pseudocapacitance in the series was used; at the same time, two tan circuits in series were used for PVA/[EMIM] [SCN] ionogel membrane. The respective models were in good agreement with the experimental values and were shown as an inset in Figure 44 and Figure 45. From the fit parameters, the pseudocapacitance values for PMMA/[BMPyr] [TFSI] and PVA/[EMIM] [SCN] were calculated and tabulated in Table 17, in which CPE is a constant phase element in the equivalent circuit, CPE-T is the pseudocapacitance which is called Q and CPE-P related to the depressed semicircle in the Nyquist plot depicted as *n*; then the pseudocapacitance

(148) can be calculated in the order of 10^{-6} Fcm^{-2} from the equation (149).

$$C = R^{\frac{1-n}{n}} Q^{\frac{1}{n}}$$

Table 18. The fit parameter obtained from the equivalent model circuit using Zview software for ionogel membranes.

PMMA/[BMPyr][TFSI] wt/wt%	R1 (MΩ)	CPE1-T (μF)	CPE1-P (μF)	CPE2-T (μF)	CPE2-P (μF)	$C = R^{\frac{1-n}{n}} Q^{\frac{1}{n}}$ (μF)
100:0	0.68574	0.001378	0.93809	0.001302	0.96964	**0.00087**
90:10	0.011415	0.08594	0.92789	0.16075	0.95871	**0.050166**
80:20	0.003183	0.065557	1.273	0.25098	0.88824	**0.403583**
70:30	0.006376	0.16845	0.91583	0.34732	0.94338	**0.089868**

PVA/[EMIM][SCN] wt/wt%	R1(MΩ)	C1(F)	R2(MΩ)	CPE2 (F)	n	$C = R^{\frac{1-n}{n}} Q^{\frac{1}{n}}$ (μF)
100:00	0.873	1.734E-11	83.6	3.604E-10	0.8	**0.00015**
95:05	1.68	1.218E-11	9.28	5.387E-8	0.62	**0.0352**
90:10	0.841	1.436E-11	10.22	3.97E-10	0.87	**0.000173**
80:20	0.848	1.341E-11	1.18	3.07E-6	0.8	**4.24**
70:30	0.049	4.52E-11	4.41	5.867E-11	0.92	**0.000028**

From the fit parameters and calculated pseudocapacitance, a similar behavior of capacitance was observed for two sets of ionogel membranes. Maximum capacitance is observed for the ionogel membrane with 20% ionic liquid. Further increase of ionic liquid decreases the movement of ions due to agglomeration that may restrict the hopping of ions.

6.3. Cole–Cole Plot

Robert Cole contributed a universally powerful tool to the present dielectric relaxation results through the Cole-Cole plot. The Cole-Cole plot is an Argand diagram or complex locus diagram of the complex dielectric constant, where $\varepsilon''(\omega)$ plot as a function of $\varepsilon'(\omega)$ (150). The complex

dielectric in the applied ac field can be written as follows:

$$\varepsilon^*(\omega) = \varepsilon'(\omega) - j\varepsilon''(\omega)$$

where ω is frequency as a parameter.

The dielectric constant can be expressed in terms of decay time for the materials that retain their polarization even after stopping the applied electric field. This may cause it to have a decay time to attain the equilibrium, a phenomenon called the Debye relaxation. The Cole-Cole plot can effectively be used for a complete understanding of the electrical properties of the ionogel membranes. For a dielectric sample, the Cole--Cole plot is a semi-circle for single relaxation time, but for conducting samples, there will be a spike or line the closer it is to the line parallel to the y-axis that the sample is conducting most.

The Cole--Cole plot for PMMA/[BMPyr] [TFSI] ionogel membrane was shown in Figure 46. Through close examination, it will be understood that the PMMA membrane is a pure dielectric sample with a single semi-circle and a small spike. The radius of the semi-circle determines their dielectric strength; on the addition of IL, it is found that the radius of the semi-circle decreases while the length of the spike increases and tends to be parallel to the y-axis until 20 % of IL; beyond that, the sample showed a unique nature. This emphasizes that the entrapment of [BMPyr] [TFSI] increases the ionic conductivity of the membrane.

Similar behavior is observed for PVA/[EMIM] [SCN] ionogel membranes as shown in Figure 47; the only difference is that the neat PVA itself shows a spike after the semi-circle. In addition, in ILs, the radius of the semicircle is found to decrease, and the spike is found to be most parallel to the Y-axis.

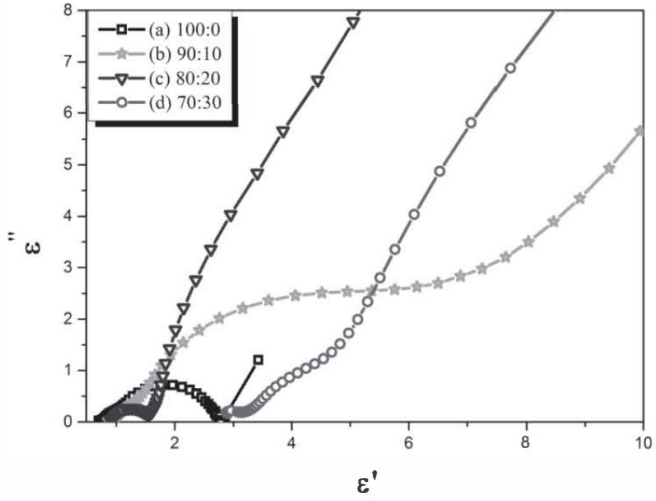

Figure 46. The Cole–Cole plot for PMMA/[BMPyr] [TFSI] ionogel membrane with different weight ratios.

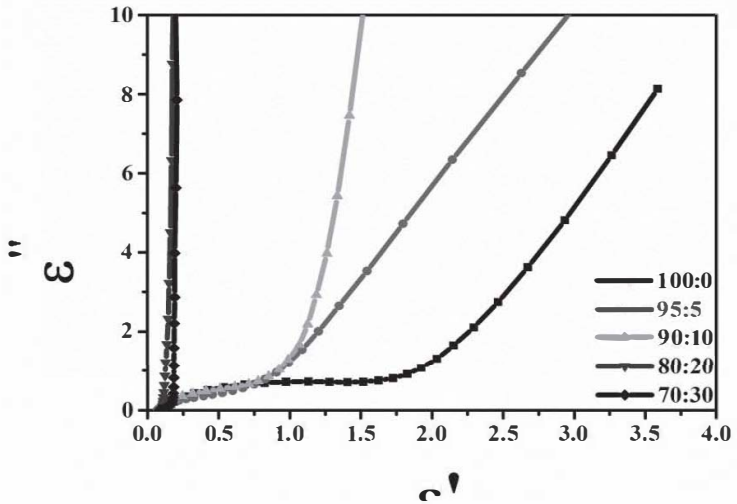

Figure 47. The Cole–Cole plot for PVA/[EMIM] [SCN] ionogel membrane with different weight ratios.

6.4. Transport properties

It is necessary to measure the electrical conductivity of ionogel membranes with varying wt ratio of ILs close to room temperature in a wide frequency window (10^{-1} to 10^{7}), in order to have a better understanding of the charge transport mechanism of the films. Even though the dopant in the matrix is the same, there is a possibility of chaotic behavior in varying the weight concentration of the dopants. Thus, the complex conductivity of all ionogel membranes with varying concentrations of IL has been measured to have an insight into the charge transport mechanism of the ions in the matrix.

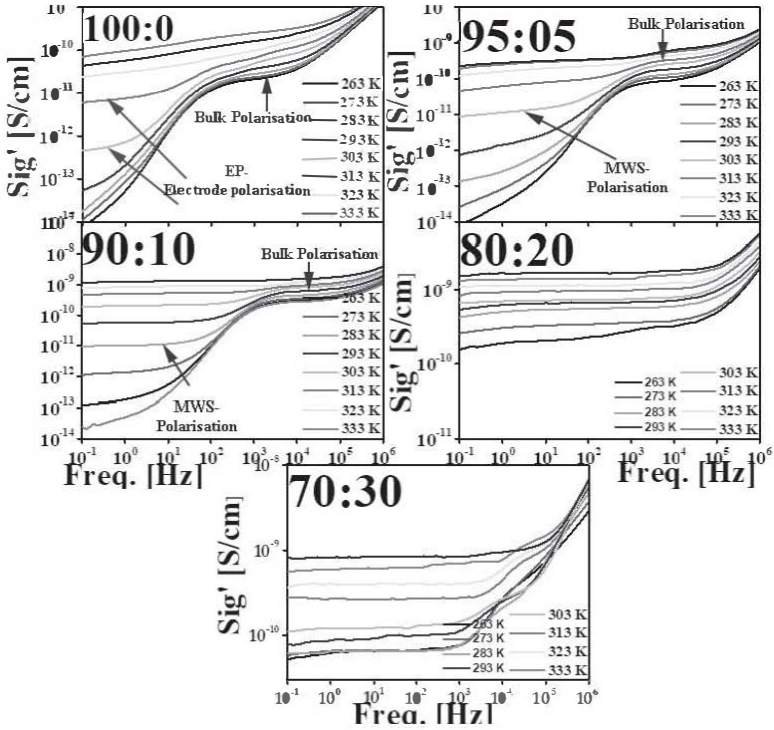

Figure 48. Frequency dependence of the real part of complex conductivity for selected temperatures of PVA/[EMIM] [SCN] ionogel membrane wt/wt% a) 100:0 b) 95:05 c) 90:10 d) 80:20 e) 70:30.

Figure 48 shows the variation of electrical conductivity with [EMIM] [SCN] loading in the temperature range of 263 K to 343 K in a wide

frequency window. At high temperatures, the frequency independent dc plateau was very evidently observed in all ionogel membranes. This conduction of ions may be attributed to bulk polarization mechanisms since it starts right from high frequencies, where the charge carriers are independent of the applied frequencies since they fail because of the rapid changes caused due to frequency oscillations in the electrical field. As the temperature decreases additional relaxation is visible; this is because, at lower temperatures, the exchange of charge carriers takes place through different channels present in the ionogel membrane. The frequency dependence of the real part of bulk ac conductivity σ'(ω) is adequately described by Jonscher's power law (JPL) (98)

$$\sigma_{ac} = \sigma_0 + A(T)\omega^S$$

where $\sigma_{ac}$is the ac conductivity, σ_0 is the limiting zero frequency conductivity σ_{dc}, A(T) is the temperature-dependent parameter, ω = 2πf is the angular frequency, and s (0 < s < 1) is the power law. However, at a lower temperature, considering two processes separately with JPL will be enough to elucidate information regarding the frequency independent plateau of two hopping, i.e., σ_{dc}.

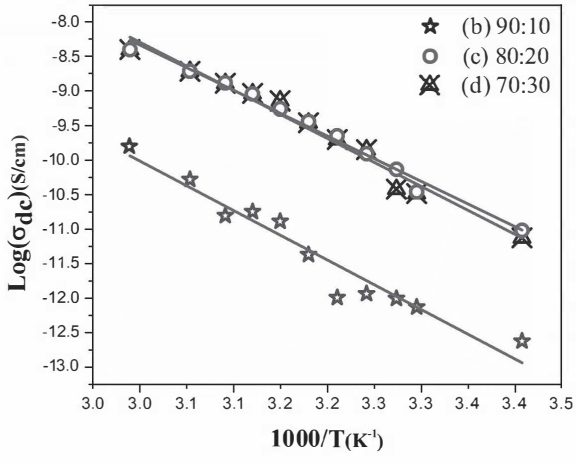

Figure 49. Temperature dependence of dc conductivity of PMMA/[BMPyr] [TFSI] ionogel membrane PMMA/[BMPyr] [TFSI] wt/wt% a) 100:0 b) 90:10 c) 80:20 d) 70:30.

However, in the case of electrical conductivity of PMMA/[BMPyr] [TFSI] the ionogel membrane consists of three distinct regions: a low-frequency dispersion due to electrode electrolyte or the space charge polarization effect (151, 152), an intermediate plateau that is almost frequency independent and can be considered as dc conductivity σ_{dc} and, finally, frequency dependent conductivity. But it is observed that PMMA is a lack of the intermediate plateau of dc conductivity, it showed only the electrode electrolyte polarization as well as frequency dependent conductivity. The temperature dependence of the dc conductivity is shown in Figure 49.

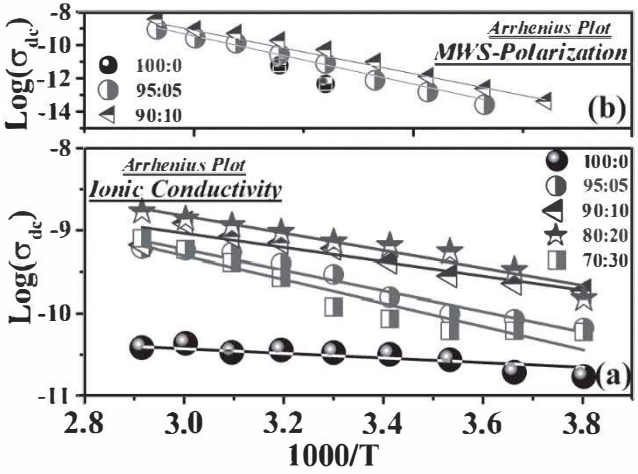

Figure 50. Temperature dependence of ionic conductivity b) temperature dependence of ionic conductivity arose due to interfacial polarization or Maxwell-Wagner-Sillars polarization.

Since the two cases are contrary in terms of charge transport phenomena, the addition of [BMPyr] [TFSI] in the PMMA matrix just increases the temperature dependence of the conductivity relaxation due to bulk polarization and increases their stability and fragility, but the addition of [EMIM] [SCN] in the PVA matrix formed one additional relaxation due to interfacial polarization. This awkward behavior arose due to the nature of bonding between the IL and the polymer matrix. In PMMA/[BMPyr] [TFSI] ionogel membrane, IL is entrapped in the matrix using additional hydrogen bonding; this chemical bonding made the film more flexible and will attain a tendency to act as one bond in the presence of the ac field.

However, in the PVA/[EMIM] [SCN] ionogel, the IL is just entrapped in the matrix without any additional bond formation and bond breakage, causing a dielectric boundary between the soft and hard regions. The conductivity of all ionogel membranes was found to increase with temperature. The conductivity of PVA was found to be insignificant since the dc conductivity is restricted to the small frequency area and is solely due to bulk polarization. However, at two specific temperatures, 303 and 313 K, it shows additional dc conductivity in the lower frequency region, which may be ascribed to the sample electrode interface. The addition of [EMIM] [SCN] has produced two conduction mechanisms; one due to bulk polarization mechanisms and the second due to hopping of charge carriers within a microscopic distance and due to their being trapped at inner dielectric boundary layers generating interfacial polarization (IP) or Maxwell-Wagner-Sillars polarization (MWS) at low-frequency range (153). IP appears in the samples exhibiting heterogeneity since the ionogel membranes are made up of semiconducting lakes (usually represented as "semiconducting islands" for dopants in solid form (154), here ours is a liquid) in an insulating matrix. Such charge carriers attempt to follow an alteration to the applied field at lower frequencies than the time scale of typical dipolar relaxation. Thus, IP arises from the ionic polarization occurring at the interface of soft (trapped [EMIM] [SCN]) and hard (Polymer matrix) (83, 84, 86, 155–57) as well as from variations of the morphology between amorphous and semi-crystalline segments. The ionic conductivity due to IP increases initially with an increase in the concentration of IL then found to merge with the bulk polarization effect due to the plasticizing nature of [EMIM] [SCN].

It is visible that the conductivity increases with an increase in weight ratios of IL till 20%, a further increase, and a decrease in the conductivity, which indicates the reducing degree of freedom due to the bulky nature of ILs. Further, it is noticed that the dc conductivity and temperature relationship between (log σ and 1000/T) obey Arrhenius law.

$$\sigma_{dc} = \sigma_0 \exp\left(\frac{-Ea}{KT}\right)$$

where σ_0 is a re-exponential factor, Ea is the conduction activation energy, K is the Boltzmann constant, and T is the temperature in Kelvin (calculated and tabulated in Table 18).

Table 19. Activation energy, Ea, and Log (σ_0) for various weight ratios of prepared ionogel membranes PMMA/[BMPyr][TFSIand PVA/[EMIM] [SCN] ionogel membrane

PMMA/[BMPyr] [TFSI] wt/wt%	Log (σ_0)	EA(eV)
90:10	11.53	1.43
80:20	12.55	1.38
70:30	11.37	1.30

Samples PVA/[EMIM] [SCN]	Ionic conductivity bulk polarization		Ionic conductivity interfacial polarization	
	Log (σ_0)	Ea (eV)	Log (σ_0)	Ea (eV)
100:00	-9.5833	1.90		
95:05	-5.51604	1.10	7.95848	1.15
90:10	-6.46637	1.28	6.54665	1.04
80:20	-5.68015	1.13		
70:30	-5.97923	1.90		

Remarkably, the incorporation of IL into the polymer membranes results in a considerable increase in the ionic conductivities of the membranes with an increase in the amount of IL at all the temperatures examined; however, it abruptly decreases with the addition of excess IL.

The addition of IL distributed homogeneously through the PVA matrix in a composite electrolyte membrane creates a high degree of continuous transfer channels for ionic hopping, thereby resulting in higher conductivity. However, with a further increase in IL, the blocking effect starts to predominate due to the agglomeration of ions in the matrix, thus reducing the conductivity of the composite membrane (149).

Figure 50 clearly shows that the incorporation of [EMIM] [SCN] can yield higher conductivity with decreased activation energy until 20% of IL, whereas a higher amount of IL demands more energy to make the ions free enough for hopping, as shown in the schematic diagram in Figure 51.

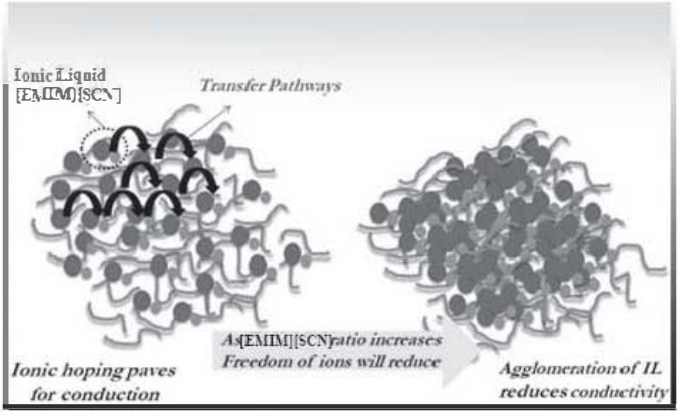

Figure 51. Schematic diagram showing the transfer pathways in lower concentration and blockage of pathways due to agglomeraton in a higher concentration of IL in the polymer matrix.

6.5. I-V Characteristics

The leakage current characteristics of all ionogel membranes were studied using a Keithley instrument. The corresponding J-V curve of PMMA/[BMPyr] [TFSI] and PVA/[EMIM] [SCN] membranes were depicted in Figure 52 and Figure 53. No hysteresis was found in the J-V characteristics because the forward and reverse sweep direction eliminates the possibility of deep traps in the PMMA and PVA films (158).

It is observed that the leakage current increases with an increase in the concentration of [BMPyr] [TFSI] in the PMMA matrix. The maximum obtained leakage current for PMMA/[BMPyr] [TFSI] ionogel membrane is 5.05×10^{-6} A/cm^2 for 30% doped ionic liquid, while that of the pure PMMA film is 7.50×10^{-9} A/cm^2 at 4 KV/cm. This may be attributed from the hopping mechanism of ions in the ionogel membranes, causing the membranes to have sufficient energy to push against hydrostatic pressure and create a space for a molecular motion to occur. The asymmetric modulation at 0 V may be due to contact charging between the polymer film and the metal surfaces.

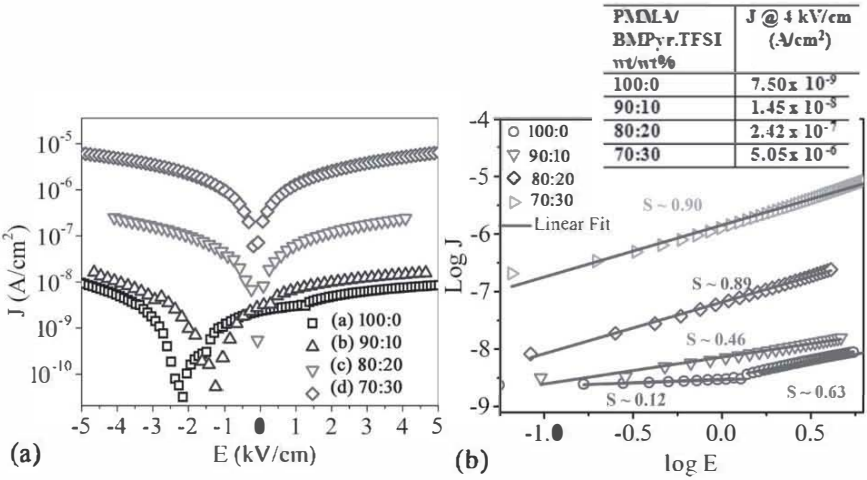

PMMA/ BMPyr.TFSI wt/wt%	J @ 4 kV/cm (A/cm²)
100:0	7.50×10^{-9}
90:10	1.45×10^{-8}
80:20	2.42×10^{-7}
70:30	5.05×10^{-6}

Figure 52. a) The leakage current characteristics of prepared ionogel membranes PMMA/[BMPyr] [TFSI] wt/wt% a) 100:0 b) 90:10 c) 80:20 d) 70:30 measured at room temperature. (b) Leakage current density for ionogel membranes PMMA/[BMPyr] [TFSI] wt/wt% a) 100:0 b) 90:10 c) 80:20 d) 70:30 fitted by space charge limited conduction (SCLC) mechanism.

The leakage current characteristics of PVA and when doped with ionic liquid are shown in Figure 53. Similar behavior is observed for the J-V characteristics of the PVA/[EMIM] [SCN] ionogel membranes. The leakage current increases with the concentration of ionic liquids from 1.59×10^{-8} A/cm^2 at 5 KV/cm to 1.10×10^{-3} A/cm^2 leakage current at 5 KV/cm for 70:30 weight ratio of PVA/[EMIM] [SCN]. The same hopping mechanism as mentioned for PMMA membranes is responsible for the increase in the leakage current and consequently attained sufficient energy to push against hydrostatic pressure and create a space for a molecular motion to occur. The PVA film doped with 30% IL could not sustain a higher electric field and leads to burning, so we have to measure it at a low field only due to the aggregation of [EMIM] [SCN] in the PVA matrix (78).

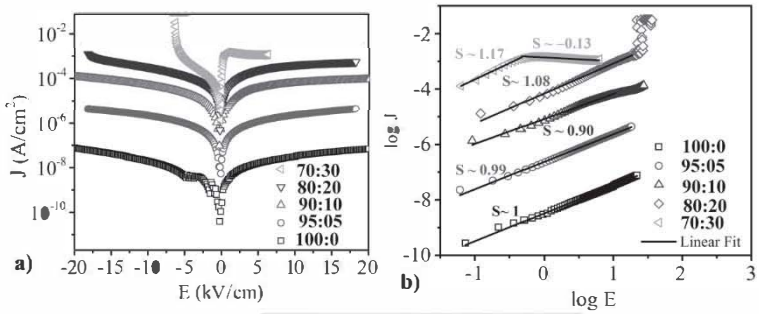

c)

Samples PVA/EMISCN	J@ 5 kV/cm (A/cm²)
100:00	1.59×10^{-8}
95:05	1.17×10^{-6}
90:10	3.82×10^{-5}
80:20	2.41×10^{-4}
70:30	1.10×10^{-3}

Figure 53. The leakage current characteristics of PVA and ionic liquid doped PVA films measured at room temperature. b) Leakage current density for PVA and PVA-IL films fitted by space charge limited conduction (SCLC) mechanism.

Figure 53 depicts the log (J) versus log (E) plots at the lower electric field, which represents the SCLC mechanism. The slopes are approximately one at low electric fields, indicating Ohmic conduction behavior. Pure PVA and 5% IL-doped PVA films show an Ohmic conduction mechanism. As the concentration of ionic liquid increases to 10% and higher, the slope is no longer linear and does not exhibit an SCLC mechanism. This is due to the translational hopping of [EMIM] and [SCN] ions through the polymer matrix. For PVA with 20% IL, the current sharply increases at high electric fields due to an increase in the free ions for conduction, while for PVA with 30% IL shows a negative slope at a higher field, which means the current decreases with the increase in the field. This may be due to the blocking effect of ions on the sample electrode interface.

6.6. Conclusion

This chapter describes the charge transport mechanism of developed ionogel membranes using broadband dielectric spectroscopy and J-V characteristics. In particular, the integration of ionic liquids in the non-conducting polymers increased the ionic conductivity of the matrix substantially. The use of ionically conducting ionic liquids in the polymers

alleviates problems in the PVA and PMMA by increasing the conductivity and flexibility of the film. The high degree of compatibility between the matrix and doped IL makes them particularly interesting for making new transfer pathways for the ionic hopping. The diverse morphology of IL as well as the matrices significantly affected the mode of the transport mechanism. The parameters of ionic hopping depend upon the interaction of IL with the polymer matrix and specific morphological order of the IL molecules. Comparing the results obtained the miscible PMMA/[BMPyr] [TFSI] membranes, which showed an increase in the temperature dependence of the conductivity while that of PVA/[EMIM] [SCN] with a wrinkled pattern exhibited one additional dc conductivity at a lower frequency region due to interfacial polarization caused upon crossing the boundary between the trapped IL and PVA. It can be concluded that the dynamic dielectric response of the membranes was sensitive to the fine structure of the membranes. This provides a new possibility to separately determine the correlation between morphology and ionic mobility. The same strategy can be employed to unravel charge transportation in a different class of polymer composites and blends. The ionogel membrane with its high value of conductivity along with better thermal and mechanical properties is desirable for its possible use in devices.

CHAPTER 7

APPLICATION

7.1. Introduction

The unique chemical and physical properties of ionic liquids include non-volatility, high thermal stability, high ionic conductivity that enables transport of charge, reduced toxicity, good solvents for both organics and inorganics, non-flammability that reduces the risk of ignition, wide electrochemical window up to seven volts that allows stability towards oxidation and reduction processes, and high thermal stability, up to 300–400°C, which makes them interesting to employ as prominent candidate electrolytes (159, 160). A standout among the most imperative application research areas for IL usage is undoubtedly their energy application. There is an increasing demand for clean and sustainable energy, especially for energy storage and conversion materials and gadgets. Ordinary precedents are lithium batteries and fuel cells, which have commercial application in hybrid, electric, and fuel cell vehicles as well as for stationary use in homes and buildings, up to large power grid-scales that has already commenced (160). However, at the same time, its liquid nature— molten salts having melting points lower than 200 °C, and most of them having leakage problems—reduces their application. Nowadays solid state devices received great interest since they have unconventional physical properties that are superior, in many respects, to those of ILs. In addition to ILs, remarkable features, ionogel membranes also typically have reasonable conductivities, thermal stabilities and a wide electrochemical window contributing to their potential as solid-state electrolytes for electrochemical capacitors, sensors, separations, and organic synthesis. They are also being developed for energy devices such as batteries, fuel cells, and photoelectrochemical solar cells, etc.

The present themed issue demonstrates the potentialities of the developed two ionogel membranes namely PMMA/[BMPyr] [TFSI] and PVA/[EMIM] [SCN] in electrochemical applications such as capacitors, optoelectronic devices, sensors, etc.

7.2. Capacitor applications

An electrochemical capacitor is an attractive energy storage device used to store energy in the form of an electrical charge producing a potential difference (static voltage) across their plates (161). Thus, a capacitor is an energy storage device with high power density, fast charging and discharging, long cycle life, excellent reversibility, and good safety. A standard capacitor is made up of two or more parallel conductive (metal) plates electrically separated either by air or any other dielectric. The conductive metal plates of a capacitor can be of any shape, such as circular, square, or rectangular, or they can be of a cylindrical or spherical shape with the general shape, size, and construction of a parallel plate capacitor depending on their application and voltage rating (161).

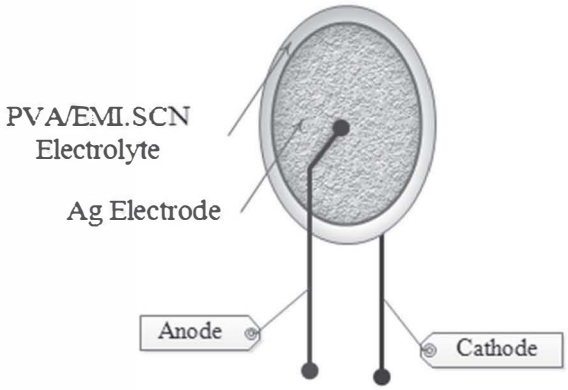

Figure 54. The schematic diagram of a PVA/[EMIM] [SCN] solid electrolyte capacitor.

The capacitance and electrochemical stability window of the IL-based solid-state polymer electrolyte were estimated using cyclic voltammetry (CV) performed on an Ag| PVA/[EMIM] [SCN] | Ag cell using an electrochemical analyzer (model 608C, CH Instruments, USA). The schematic representation of the cell is shown in Figure 54. All the measurements were performed in a two-electrode system in the potential range between -1 to 1 V with a scan rate of 20mV/s at room temperature.

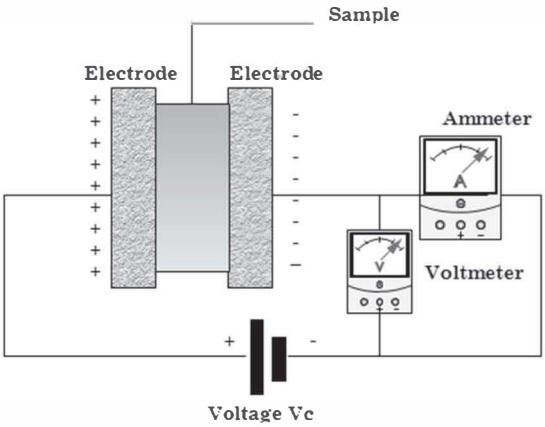

Figure 55. The typical diagram showing the measurement set up for IV-characteristics.

Cyclic voltammetry (CV) gives information about the nature of charge storage at the individual interfaces of the membrane in the anodic and cathodic regions. A CV can also be performed in a two-electrode configuration, particularly, in solid state-like capacitors, double-layer capacitors, and supercapacitors from which the overall behavior of the membrane can be characterized. In this work, CV was used to measure the electrical capacitance of the PVA/[EMIM] [SCN] membranes with Ag electrodes, which depends solely on the accessible surface area and ion concentration of the solid polymer electrolyte films (162). The profiles obtained for Ag|PVA/[EMIM] [SCN] |Ag are shown in Figure 56. As the concentration of IL increases to 20%, the shape of the CV approaches a rectangular shape; at a further increase of [EMIM] [SCN], the shape is no longer rectangular, it becomes fish-shaped, indicating it has diffusion problems due to aggregation of the [EMIM] [SCN].

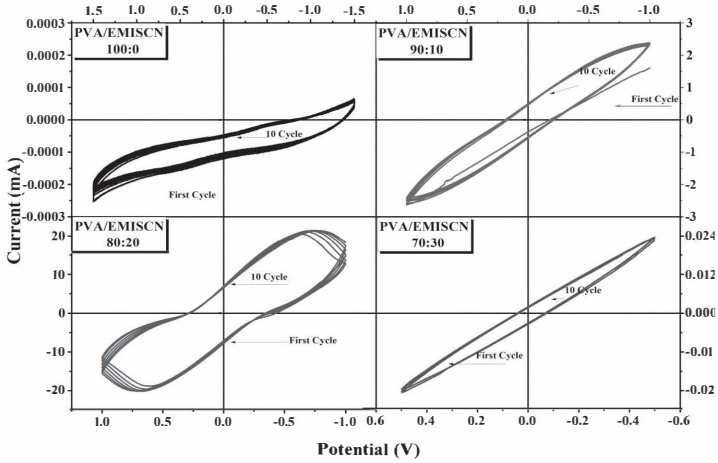

Figure 56. Cycle voltammetry of Ag|PVA/[EMIM] [SCN]|Ag capacitor with a different weight ratio of PVA/[EMIM] [SCN] at room temperature.

There were no faradic peaks or other peaks suggesting adsorption/desorption effects, and only the capacitive current due to the electrode–electrolyte interface and the onset of oxygen reduction were observed for all membranes (163). The amount of charge stored in the membrane can be calculated from the area under the profiles obtained from CV using the following equation.

$$C = \frac{A}{2k(E_2 - E_1)}$$

where C is the capacitance of the membrane, A is the area under the profile, K is the scanning rate, E_2 is the final voltage, and E_1 is the initial voltage. The estimated capacitances were tabulated in Table 19.

Table 20. The estimated capacitances for various weight ratios of SPE membranes

Samples PVA/[EMIM] [SCN]	Area	E_2 (V)	E_1 (V)	Capacitance C/g
100:00	1.87E-07	1.5	-1.5	1.56E-06
90:10	0.002842	1	-1	0.035521491
80:20	0.021325	1	-1	0.266567384
70:30	1.90E-05	0.5	-0.5	0.000475367

It is fascinating to note that the area under the profile increases with increasing concentration of [EMIM] [SCN] till an 80:20 weight ratio, which in tum increases the capacitance of the membrane and attains a maximum of 0.26 C/g for 80:20 PVA/[EMIM] [SCN] membrane and also inhibits the conduction through the polymer chain. This is due to the translational hopping of EMIM and SCN ions through the polymer matrix. The diminished area swept, the low capacitance, and then the arrow electrochemical window of PVA/[EMIM] [SCN] film with a weight ratio 70:30 may be due to a diffusion problem of ions through the PVA matrix.

7.3. Gas-sensing application

In modern society, the hoisted increment in the level of CO_2 can be considered as a noteworthy environmental problem. According to the report of the international climate observing body, CO_2 concentration has increased by around 3.3 parts per million (ppm) each year and reached 403.3 ppm in 2016. Compared to the Ice Age, the rate of increase of CO_2 is almost 100 times higher (164). The most recent assessment of the Global Carbon Project shows that growing population and a record level of human exercises, increases in land use and deforestation, intensified agricultural practices, industrialization and associated energy use from fossil fuel sources, and so on are responsible for this rapid increase in the greenhouse gas in the atmosphere (164). In this scenario, research upon CO_2 monitoring in the atmosphere and problems associated with it demands the preservation of the clean environment in an airtight chamber or in underground geological sites. In this scenario, periodic monitoring and capturing of CO_2 waste from large point sources, such as fossil fuel power plants, and carrying it to storage sites where it will not enter the atmosphere are the need of the hour. One of the proposed solutions is carbon capture and storage to lessen anthropogenic CO_2 emissions. Carbon capture and storage (CCS) is the way towards capturing carbon dioxide (CO_2) waste from large point sources, such as fossil fuel power plants, transporting it to a storage site, and dumping it where it will not enter the atmosphere, typically in an underground geological formation. Though CO_2 has been injected into geological formations for several decades for various purposes, including enhanced oil recovery, the long term storage of CO_2 is a relatively new concept. The first commercial example was the Weybum-Middle Carbon Dioxide Project in 2000 (165). Another example is SaskPower's, Boundary Dam. "CCS" can also be used to describe the scrubbing of CO_2 from ambient air as a climate engineering technique (166). The integrated pilot-scale CCS power plant estimates that the

economic potential of CCS could be between 10% and 55% of the total carbon mitigation effort until the year 2100 (167).

To achieve this, different classes of materials have been explored viz. absorbents, adsorbents, permeable membranes, etc. Among them, polymer-based membranes, including hybrid polymer-organic membranes, and polymer-inorganic membranes are considered as most efficient for CO_2 separation (168). Of all the membrane materials, polymer-based membrane materials are of particular commercial interest due to their low cost and ease of large-scale manufacture (169, 170). Polymers with high permeability, gas condensability, affinity between the gas molecule and the matrix, and increased void space in the polymer matrix are preferred for CO_2 capture and storage.

The PVA/ [EMIM] [SCN] ionogel membrane can be used as a promising permeable membrane for CO_2 sensing, capturing, and storage, since the IL [EMIM] [SCN] plays a crucial role in capturing the CO_2, while PVA provides a mediocre platform to store the captured CO_2 (171). The features of [EMIM] [SCN] including high CO_2 solubility and selectivity, low volatility, high conductivity, and unique structures, making it a better option as a dopant in a PVA matrix for CO_2 gas capturing. These features of [EMIM] [SCN] surely overcome the hindrance of PVA due to their semi-crystalline nature and lack of sites; consequently, there has been much interest in incorporating [EMIM] [SCN] as a particular component in a PVA membrane (172–74).

7.2.1. Fabrication of SPE CO_2 Sensor

Simple inter-digitated Ag electrodes were used as a cost-effective approach for CO_2 gas-sensing experiments and for their electrical impedance measurements. The schematic diagram showing the interdigitated Ag electrodes were used on the PVA/[EMIM] [SCN] films as shown in Figure 57, in which one side is fully exposed to the CO_2 gas.

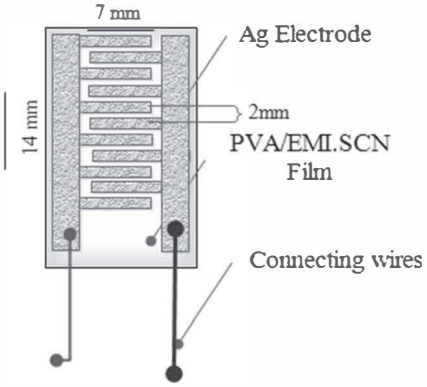

Figure 57. Schematic diagram of interdigitated electrodes on the PVA/[EMIM][SCN] CO_2 sensor.

The CO_2 sensing system consists of a homemade gas chamber with an inlet at a lower end connected to the CO_2 cylinder. The measurement system is shown in Figure 58. The concentration and pressure of the CO_2 gas were controlled by a mass flow controller (MFC). To measure the response of the developed sensing material, a high-precision multimeter (6.5 digits, Tektronics, Model No: DMM 4050) was used in series with a programmable DC power supply (Tektronix Model No. PWS4000). The current was recorded in DC mode with a wide voltage range.

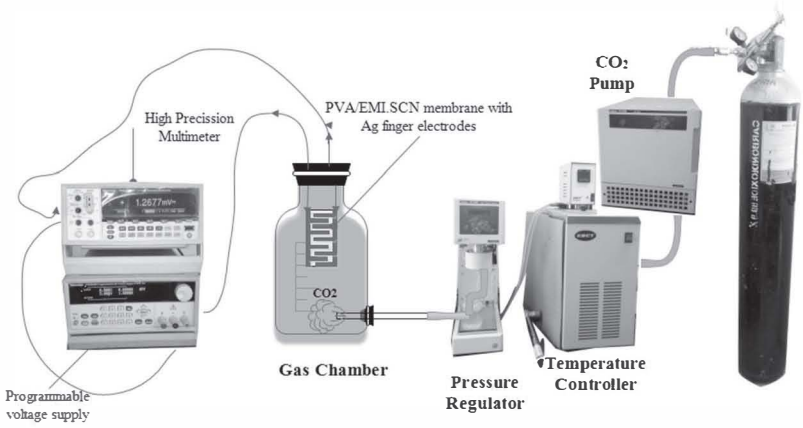

Figure 58. Schematic diagram of the CO_2 sensing setup.

A low-cost chemical resistive sensor for CO_2 detection by coating PVA: [EMIM] [SCN] on interdigitated Ag electrodes was used to study the influence of [EMIM] [SCN] in a PVA matrix on CO_2 capturing and storage. The ionogel membranes with interdigitated electrodes on one side were exposed to 500 ppm CO_2 in a closed chamber with a total volume of 100 ml for 20 minutes.

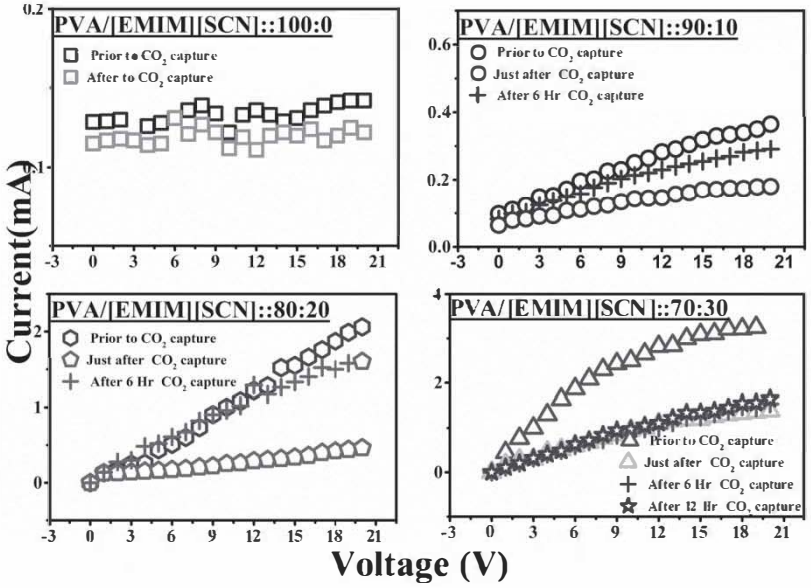

Figure 59. The I-V response of the ionogel membrane with different weight ratios before and after CO_2 exposure.

The net gas flow rate was maintained at 5 ml/min and controlled by a mass flow meter. The sensor apparatus is shown in Figure 58, and the responses of each film before and after exposure to CO_2 gas were shown in Figure 59. The responsive resistance of the films before and after CO_2 exposure is tabulated in Table 20.

Table 21. The calculated responsive resistance of the films before and after CO_2 exposure.

PVA/[EMIM][SCN] wt/wt%	The resistance of the sensor before CO_2 exposure, R_0(KΩ)	The resistance of the sensor after CO_2 exposure, R_{CO_2} (KΩ)
100:0	1416.03	4556.24
90:10	73.31	170.64
80:20	9.32	51.81
70:30	6.14	14.56

From Table 20, it is clear that the resistance of the ionogel membrane reduces with the increase in the concentration of [EMIM] [SCN], which in turn points out that as the concentration of IL increases, the conductivity of the film increases. The addition of IL in PVA resulted in an increase in the degree of amorphicity and number of mobile ions ($[EMIM]^+$ and $[SCN]^-$), which in turn gave rise to an abrupt increase in the conductivity of the membranes (78). It was fascinating to note that the resistance of each film was found to increase as CO_2 gas was introduced, as shown in Table 1. This controversial increase in the resistance may be due to the presence of [EMIM] [SCN] in the membranes, as thiocyanate anion $[SCN]^-$ plays a key role in gas capture in IL. The captured CO_2 interacts with $[SCN]^-$ easily to form a carbamate and may make the anion more complex. This complexity may adversely affect the hopping of $[EMIM]^+$ and $[SCN]^-$ in the PVA matrix of the membrane, which in turn reduces the conductivity (171). This strong spatial correlation between the carbon atom of CO_2 and the nitrogen atom of the $[SCN]^-$ is dependent on the concentration of [EMIM] [SCN] ionic liquid in the ionogel membrane. As the concentration increases the higher the CO_2 capture will be.

The response of the sensor (S) was evaluated by the following formula:

$$S(\%) = \frac{I_g - I_a}{I_a} \times 100\%$$

where I_g is the responsive current of the sensing film upon exposure of CO_2 gas and I_a is the responsive current of the sensing film without CO_2 gas (175).

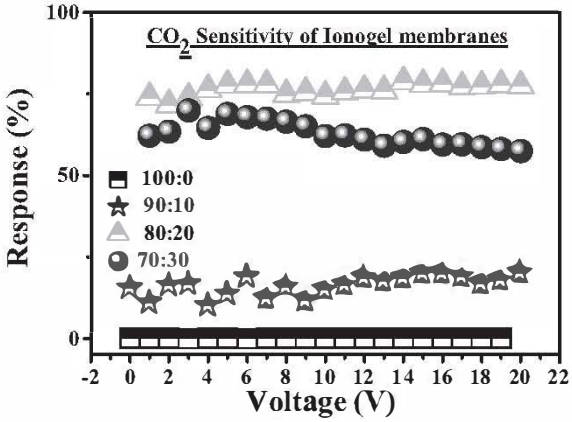

Figure 60. Voltage depended on the CO_2 response curve of PVA/[EMIM] [SCN] ionogel membranes.

The CO_2 response curve of PVA/[EMIM] [SCN] ionogel membranes with different wt/wt% for varying voltages is shown in Figure 60. The ionogel membrane with 20% [EMIM] [SCN] exhibited higher sensitivity to the CO_2 gas. The average value of the CO_2 response was shown in Figure 61.

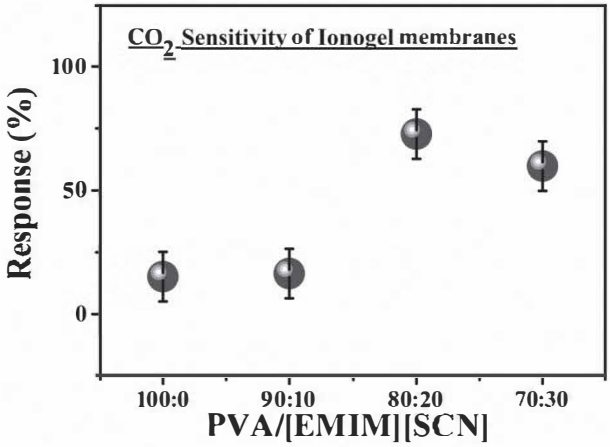

Figure 61. The response of PVA/[EMIM] [SCN] films with interdigitated electrodes to CO_2 at room temperature.

The result emphasizes that PVA/[EMIM] [SCN] films interact with CO_2 and transport CO_2 gas through their membrane reversibly due to the presence of $[SCN]^-$ anion in the IL. However, although the incorporation of [EMIM] [SCN] increased the amorphicity, and some mobile carriers, it also tuned the cavity size and free volume of the PVA matrix. The sizeable free volume created by [EMIM] [SCN], as shown as the wrinkled pattern in the SEM image being reported by Safna et al., is due to the incorporation of IL-endowed membranes with a synergistic enhancement of permeability, which is reflected in the conductivity mechanism (78). Anyhow, the overall decrease in the conductivity after CO_2 exposure gave a clear picture about CO_2 detection signal with a response, although the ionogel membrane with 20% IL exhibited the highest sensitivity to the gas. It may be due to its superior characteristics with a fairly smooth surface, increased flexibility, enhanced thermal stability, and highest ionic conductivity with low activation energy; beyond this concentration, the availability of the charge carriers is reduced due to agglomeration of ions in the PVA matrix. Detailed discussions on the excellent performance of 80:20 PVA/[EMIM]SCN] ionogels have already been reported by Safna et al. (78). The reason why the amount of [EMIM] [SCN] incorporated in PVA films played a key role in the performance of the sensor may be related to the interaction between the CO_2 and the incorporated IL, will be discussed in the coming section.

The periodic measurement after the CO_2 exposure was recorded to monitor the storage capacity of the membrane and depicted those data too in Figure 61. The results revealed that though an ionogel membrane with 20% [EMIM] [SCN] exhibited a higher response rate, the storage time of CO_2 in the membrane is much less, and the ionogel membrane with 20% [EMIM] [SCN] returned to its initial phase within 6 hours. A detailed investigation has to be done to trace the time-decay process of this film. A controversial ionogel membrane with 30% [EMIM] [SCN] exhibited higher storage time for CO_2 in the membrane and trapped the CO_2 molecule for 12 hours. The polymer membrane exhibiting CO_2 capturing and storage for 12 hours will be a great contribution in the R & D area of carbon dioxide capturing and storage. The reason behind this chaotic behavior on increasing the concentration of IL has to be explored and discussed in the upcoming section.

7.4. Optoelectronic applications

7.4.1. Transparency

The transmittance of the prepared ionogel membranes was examined using UV-visible spectroscopy and shown in Figure 62. Even though the transparency of PMMA was retained in all the membranes, the addition of IL decreases the transparency while retaining it in the range of 80–90% (176). It demonstrates the most astounding transparency around 90% for 80:20 wt% of PMMA/[BMPyr] [TFSI] blend, which might be because of the miscibility of [BMPyr] [TFSI] in PMMA. All the films show low transparency in the range between 200 to 350 nm, which may be due to high energy absorption assigned to the $\pi - \pi^*$ bond (176) present in the polymer as shown in Figure 62.

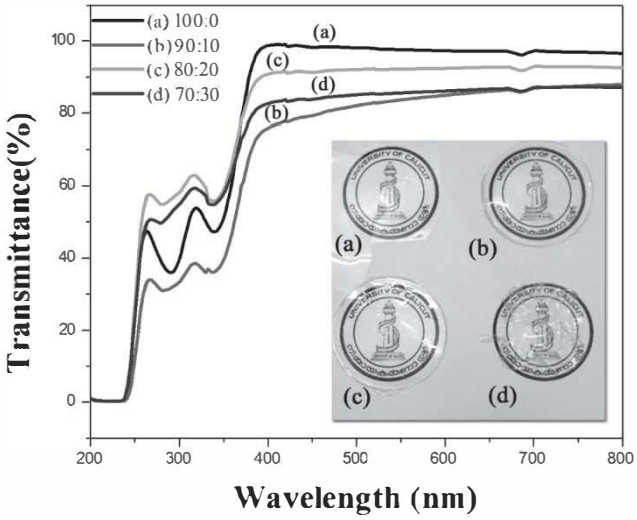

Figure 62. UV-Vis transmittance spectrum of prepared ionogel membranes PMMA/[BMPyr] [TFSI] wt/wt% a) 100:0 b) 90:10 c) 80:20 d) 70:30 showing transparency of the film.

7.4.2. Absorbance

The optical constants—like energy band structure, refractive index, optical conductivity, etc.—of solids, are important parameters that determine

their aptness for optical devices. Figure 63 shows room-temperature absorption spectra for the prepared PMMA/ [BMPyr] [TFSI] wt/wt% ionogel membranes in the range 200–800 nm. In the UV region, all the samples retain the characteristics of PMMA by exhibiting three absorption bands at the position 223, 288, and 333 nm. The strong band seen at 223 nm for all samples might be assigned to n $\rightarrow\pi^*$ transition due to the presence of C=O group; meanwhile, the other two absorptions may be assigned to $\pi \rightarrow \pi^*$ transition due to the unsaturated groups (176) (C=O, C=C) in the polymer (177).

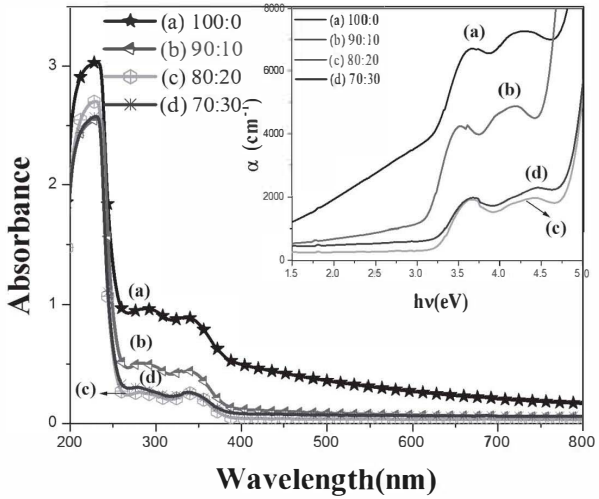

Figure 63. The optical absorbance of prepared ionogel membranes PMMA/[BMPyr] [TFSI] wt/wt% a) 100:0 b) 90:10 c) 80:20 d) 70:30 as a function of wavelength. (Inset shows an absorption coefficient of prepared ionogel membranes PMMA/[BMPyr] [TFSI] wt/wt% a) 100:0 b) 90:10 c) 80:20 d) 70:30 as a function of photon energy.

The absorption coefficient of each ionogel membrane with a different weight ratio of IL was calculated using the equation shown below:

$$\alpha = \frac{(2.303) \times A}{t}$$

where α is the absorption coefficient, and A is the optical absorbance of the film and the thickness of the film. The disparity of the absorption edge of PMMA/ [BMPyr] [TFSI] with a varying weight ratio of IL content was

depicted in the inset of Figure 64. The slight doping of IL especially 90:10 wt ratio in PMMA/ [BMPyr] [TFSI] polymer composites inhibits a shift on the absorption edge towards low energy values owing to transfer of charge.

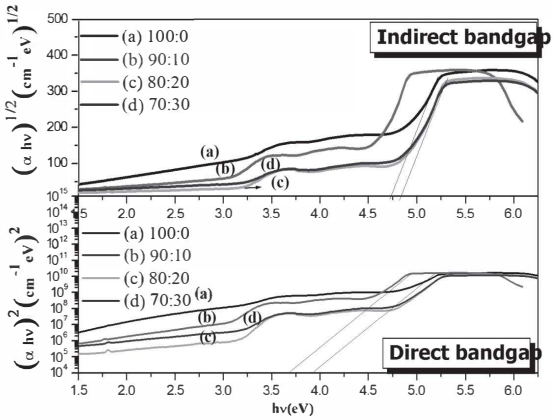

Figure 64. Direct and indirect band gaps of prepared ionogel membranes PMMA/[BMPyr] [TFSI] wt/wt% a) 100:0 b) 90:10 c) 80:20 d) 70:30.

The band gap of the solid film plays an important role in optoelectronic devices since it determines the energy required to transfer an electron from the highest occupied molecular orbital (HOMO) to the lowest unoccupied molecular orbital (LUMO) in order to make the film optically active. The smaller the band gap, the higher will be their charge conduction (178). The optical band gap can be determined from the photonic absorbance values obtained from the UV-visible spectral studies as well as some theoretical calculations using density function theory. The optical band gaps of PMMA/ [BMPyr] [TFSI] composite films involving both direct and indirect electronic transitions are depicted in Figure 64, and corresponding values are tabulated in Table 21.

Table 22. The absorption coefficient, direct and indirect band gap of prepared ionogel membranes PMMA/ [BMPyr] [TFSI] wt/wt% a) 100:0 b) 90:10 c) 80:20 d) 70:30.

PMMA/[BMPyr] [TFSI] wt/wt%	α (cm^{-1})	Direct Eg (eV)	Indirect Eg (eV)
100:0	7056	3.92	4.74
90:10	4451	3.68	4.41
80:20	1881	4.03	4.84
70:30	2321	4.03	4.84

Here it is more optimistic to consider an indirect bandgap not as directly due to the absence of valence and a conduction band as seen in metal-doped membranes. It is very interesting to note the anomalous behavior upon IL doping, it is found that a 90:10 wt ratio of PMMA//[BMPyr] [TFSI] film shows a reduced band gap of 4.41 eV compared to all other films, which reflects the role of /[BMPyr] [TFSI] IL in modifying the electronic structures of PMMA films through IL-induced polaronic and defect effects (178). The decrease in the optical band gap also reflects the increase in the degree of disorder in the film. The IL-induced structural defects may lead to the creation of a localized metastable state leading to the decreased band-gap energy for the 90: 10 wt ratio of PMMA/[BMPyr] [TFSI] film, as the wt ratio increases the ion hopping in the polymer matrix and might be decreased due to spatial freedom.

7.4.3. Photoluminescence

In the emission spectrum, two fixed wavelengths were used to excite the molecules in the prepared ionogel membranes since all the samples showed absorptions at two wavelengths in the UV range as discussed in Sec. 3.6.2 and shown in Figure 65. It is observed that for each excitation frequency, it has two emission spectra, one for fluorescence and the other for phosphorescence. Since the adjustment in the energy for fluorescent emission is by and large not as much as that for absorption, the membrane's fluorescence spectrum is moved to higher wavelengths than their absorption range (179) as shown in Figure 64.

The intensity of fluorescence is proportional to the amount of radiation absorbed by the sample, $P_0 - P_T$; the fluorescence quantum yield is given as follows (179):

$$I_f = K\varphi_f(P_0 - P_T)$$

where k is a constant related to the efficiency of collecting and detecting the fluorescent emission, and Φ_f is the fraction of excited state molecules returning to the ground state by fluorescence. The intensity of the emission increases when 10% IL then decreases by increasing the concentration of IL, which is in great concurrence with the power of absorption radiation. The addition of IL may decrease the molecular gap and allow molecules to interact, subsequently resulting in the lowering of the energy levels. It is quite possible that emission from the higher excited state may get quenched due to cross relaxation.

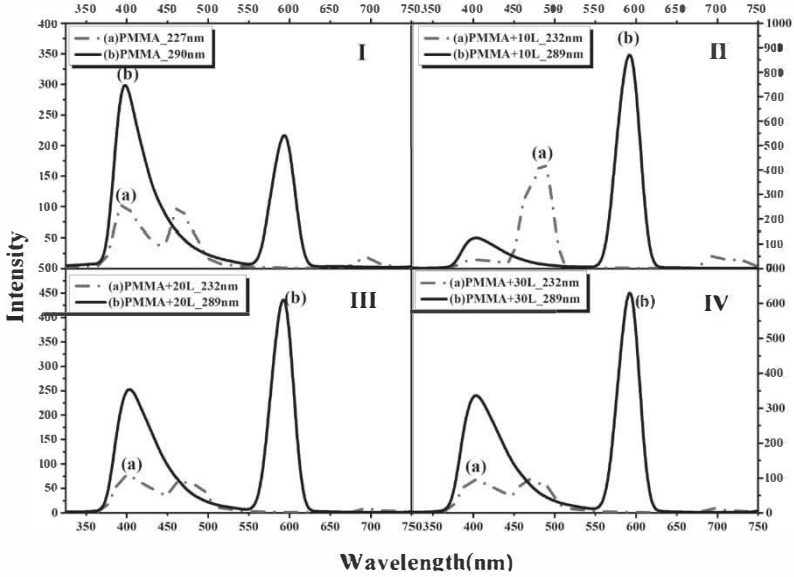

Figure 65. Fluorescence emission spectrum obtained for prepared ionogel membranes. prepared ionogel membranes PMMA/[BMPyr] [TFSI] wt/wt% I) 100:0 II) 90:10 III) 80:20 IV) 70:30.

The observed fluorescence may be due to the molecule's lowest energy absorption assigned to $\pi \rightarrow \pi^*$ transition due to the unsaturated groups (C=O, C=C) in the polymer, although some due to $n \rightarrow \pi^*$ transition due to the presence of C=O group show weak fluorescence (177). It is very evidently seen from the HOMO-LUMO structures obtained from the ONIOM calculation. The geometrical structures obtained for the HOMO-

LUMO orbitals are shown in Figure 66.

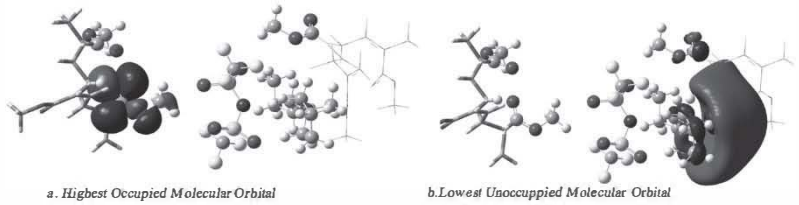

Figure 66. HOMO-LUMO orbitals of ionogel model obtained from the ONIOM Calculation using Gaussian 09.

In short, a very strong orange emission was observed in the PMMA/[BMPyr] [TFSI] ionogel polymer electrolyte membrane, which is somewhat comparable to the task-specific ionogel formed by doping europium in the PMMA matrix (71).

7.5. Conclusion

Research work becomes meaningful if it has applications in real life. The advent of the ionogel membranes will be one of the important industrial revolutions since it owes a path for solid-state gadgets. For more than two to three decades, researchers all over the world have shown that ionic liquids exhibit substantial properties to replace conventional inorganic electrolytes. However, the leakage and gas formation problems of ILs limit their application widely. These newly developed ionogel membranes will not only replace conventional and liquid electrolytes in many areas but also infiltrate our day-to-day life with a wide range of flexible solid-state products from most common consumer gadgets like capacitors, supercapacitors, batteries, sensors, fuel cells, etc. to specialized applications in space and aeronautics.

To suggest any material to be used as a potential candidate for technological applications, it is essential to undertake basic studies governing the electrical, sensing, and response properties of such materials. In this chapter, different applications of the ionogel membranes were investigated. The outcomes show that, among the prepared ionogel membranes, PMMA/[BMPyr][TFSI] is an excellent candidate for optoelectronic gadgets, since it can absorb UV light and is capable of emitting light in the visible region. Second, the PVA/[EMIM] [SCN] membrane can be used as a solid polymer electrolyte in solid-state devices.

Moreover, it can be used for the fabrication of CO_2 sensors as well as for CO_2 capturing membranes.

SUMMARY

In this concluding chapter, we summarize the contributions and efforts towards knowledge upliftment in the area of ionogel membranes and the possible impact of future technologies as we perceive it. An extensive literature review suggests that considerable efforts have been made by researchers all over the world in immobilizing ILs while retaining their unique properties including conductivity and thermal stability. It has also been noted through the literature survey that studies on dielectric and sensing properties of ionogel membranes are meager. To suggest any material to be used as a potential candidate for technological applications, it is essential to undertake thorough basic studies to understand the governing electrical and sensing properties.

We started our studies by selecting two ionic liquids and a couple of non-conducting polymers, one hydrophobic and the other hydrophilic, to immobilize the IL and overcome all the limitations of it being a liquid; it thus attributes conductivity in the polymer and, further, catches the general trends of their interactions. A novel hybrid quantum mechanical approach, "ONIOM" was used for optimizing the structures by calculating the potential energy maps of the proposed four bulk ionogel membranes, by using Gaussian software. These calculations allowed us to explore the thermochemical properties, global descriptors, and nonlinear optical properties of the membranes. Though we focused on examining the compatibility of the ILs with polymer matrices, we could extend the study of the interaction between the trapped IL and the host polymer matrix by these theoretical calculations. The two best combinations from the possible four ionogels with two distinct polymer matrices could be traced out from the activity and chemical stability of ionogel membranes favored by their structural interactions. Subsequently, we have successfully developed the two ionogel membranes by immobilizing IL via the solution casting on glass method. Once the IL is immobilized in the host matrix, its morphology and physicochemical properties play a crucial role in specifying its task.

The work narrated in this book, hopefully, reveals some very general and fundamental aspects of ionogel membranes like the necessary and sufficient conditions needed for film evolution and the procedures for finding the threshold concentration for superior performance. We

continued to explore the influence of miscibility between the IL and the polymer matrix on the ion-conduction behavior. It is worth pointing out that the morphologies have a great impression on determining their characteristics and their impact on their performance and applications. The study further gave clear evidence of the advantages of incorporating IL in non-conducting polymer matrices, resulting in enhanced thermal stability, impressive improvements in ionic conductivity, and high retention in mechanical strength, which are important qualities to consider in the applicability to electrochemical gadgets.

Two novel ionogel membranes with interesting properties such as flexibility, transparency, conductivity, and thermal stability were developed. Though the fabrication of such an ionogel is fairly simple, yet it creates highly modular membranes. Further, we successfully explored a wide variety of applications in electrochemical, electronics, and optoelectronic regimes. Only a few were mentioned here, yet there is still much to explore by keeping in mind that over the last couple of years ionogel membranes have been extensively used in electrochemical gadgets, fuel cells, solid state batteries, dye-sensitized solar cells, pharmaceuticals, etc.

One feels that the concept of ionogel opens unlimited possibilities for applications and should inspire innovation and, likely, unexpected developments in future technologies. It would seem that this work could equally be applied to a diverse and broad range of materials, including polymer composites, blends, nanocomposites, rubbers, and so on and so forth.

BIBLIOGRAPHY

1. Macfarlane DR, Tachikawa N, Forsyth M, Pringle JM, Howlett PC, Elliott GD, et al. Energy applications of ionic liquids. Energy Environ Sci. 2014; 7(1): 232–50.
2. Vioux A, Viau L, Volland S, Le Bideau J. Use of ionic liquids in sol-gel; ionogels and applications. Comptes Rendus Chim. 2010; 13(1–2): 242–55.
3. Weidlich T, Stočes M, Švancara I. Possibilities and Limitations of Ionic Liquids in Electrochemical and Electroanalytical Measurements (A Review). Sens Electroanal. 2010; 5: 33–56.
4. Ghandi K. A Review of Ionic Liquids, Their Limits and Applications. Green Sustain Chem. 2014; 4(1): 44–53.
5. Shamsuri AA, Abdullah DK. Ionic Liquids: Preparations and Limitations. Makara. 2010; 14(2): 101–6.
6. Kadokawa J. Ionic liquids—new aspects for the future. 2013. 1–356 pp.
7. Liaw BY. Electrochemical Aspects of Ionic Solids. Ohno H, editor. Vols. 125–26, Key Engineering Materials. Wiley; 1997. 133–62 pp.
8. Quartarone E, Mustarelli P. Electrolytes for solid-state lithium rechargeable batteries: recent advances and perspectives. Chem Soc Rev. 2011; 40(40): 2525–40.
9. Ionic Liquids for Electrochemical Applications. Aldrich ChemFiles [Internet]. 2005; 5(6):10. Available from: https://www.sigmaaldrich.com/technical-documents/articles/chemfiles/ionic-liquids-electrochemical.html.
10. Park J, Ueno K, Tachikawa N, Dokko K, Watanabe M. Ionic Liquid Electrolytes for Lithium—Sulfur Batteries. J Phys Chem C. 2013; 117: 20531–41.
11. Sun G hua, Li K xi, Sun C gong. Application of 1-ethyl-3-methylimidazolium thiocyanate to the electrolyte of electrochemical double layer capacitors. J Power Sources. 2006; 162 (2 SPEC. ISS.): 1444–50.
12. Sánchez-Ramírez N, Assresahegn BD, Bélanger D, Torresi RM. A Comparison among Viscosity, Density, Conductivity, and Electrochemical Windows of N-n-Butyl-N-methylpyrrolidinium and Triethyl-n-pentylphosphonium Bis(fluorosulfonyl imide) Ionic Liquids and Their Analogues Containing Bis(trifluoromethylsulfonyl) Imide Anion. J Chem Eng Data. 2017;

62(10): 3437–44.
13. Valkenberg MH, deCastro C, Hölderich WF. Immobilisation of ionic liquids on solid supports. Green Chem. 2002; 4(2): 88–93.
14. Safna Hussan KP, Mohamed Shahin T, Deshpande SK, Jinitha T V, Kolte J. Development of ion conducting ionic liquid-based gel polymer electrolyte membrane PMMA/BMPyr.TFSI—With improved electrical, optical, thermal and structural properties. Solid State Ionics. 2017; 310(May): 166–75.
15. Carvalho TIS. Development of Ion Jelly thin films for electrochemical devices. Faculdade de Ciência e Tecnologia da Universidade Nova de Lisboa; 2013.
16. Fukaya Y, Iizuka Y, Sekikawa K, Ohno H. Bio ionic liquids: room temperature ionic liquids composed wholly of biomaterials. Green Chem. 2007; 9(11): 1155–7.
17. The removal of the voltage and the illuminated light [Internet]. 20-feb-2019. Available from: https://www.coursehero.com/file/p7f0r66/the-removal-of-the-voltage-and-the-illuminated-light-has-illustrated-its/.
18. Zai-Lai X, Jeličić A, Fei-Peng Wang, Pierre Rabu, Alwin Friedrich, Sabine Beuermann, et al. Transparent, flexible, and paramagnetic ionogels based on PMMA and the iron-based ionic liquid 1-butyl-3-methylimidazolium tetrachloroferrate(iii) [Bmim][FeCl4]. J Mater Chem. 2010; 20(42): 9543–9.
19. Hussan KPS, Thayyil MS, Rajan VK, Jinitha T V. Experimental and Hybrid Quantum Chemical Investigation on PMMA Based Ionogel Membrane for Optoelectronic Devices. (Il).
20. Lu J, Yan F, Texter J. Advanced applications of ionic liquids in polymer science. Prog Polym Sci. 2009; 34(5): 431–48.
21. Lu J, Yan F, Texter J. Advanced applications of ionic liquids in polymer science. Prog Polym Sci. 2009; 34(5): 431–48.
22. Safna Hussan KP, Mohamed Shahin T, Deshpande SK. Studies of Ionogel Structure and its Electronic and Optical Characterization by ONIOM and other Hybrid Computational Approaches. Mater Today Proc. 2018; 5(8): 16272–9.
23. Polyvinyl Alcohol—An Overview [Internet]. Sciencedirect. Available from: https://www.sciencedirect.com/topics/engineering/polyvinyl-alcohol.
24. Poly vinyl Achohol. Natl Cent Biotechnol Information PubChem Compd Database; CID=11199, (accessed Nov 26, 2018) [Internet]. Available from:

https://pubchem.ncbi.nlm.nih.gov/compound/11199.
25. Le Bideau J, Viau L, Vioux A. Ionogels, ionic liquid based hybrid materials. Chem Soc Rev. 2011; 40(2): 907–25.
26. Le Bideau J, Viau L, Vioux A. Ionogels, ionic liquid based hybrid materials. Chem Soc Rev. 2011; 40(2): 907–25.
27. Ananikov VP, Musaev DG, Morokuma K. Real size of ligands, reactants and catalysts: Studies of structure, reactivity and selectivity by ONIOM and other hybrid computational approaches. J Mol Catal A Chem. 2010; 324(1–2): 104–19.
28. Safna Hussan KP, Thayyil MS, Rajan VK, Muraleedharan K. Experimental and density functional theory studies on benzalkonium ibuprofenate, a double active pharmaceutical ingredient. Comput Biol Chem. 2018; 72: 113–21.
29. Monomer MD, Liao Y, Feng J, Yang L, Ren A, Zhang H. Theoretical Study on the Electronic Structure and Optical Properties of Mercury-Containing Diethynylfluorene Monomer, Oligomer, and Polymer. 2005; 385–94.
30. Thanthiriwatte KS, Nalin de Silva K. Non-linear optical properties of novel fluorenyl derivatives—ab initio quantum chemical calculations. J Mol Struct THEOCHEM. 2002; 617(1): 169–75.
31. Wang WY, Du XF, Ma NN, Sun SL, Qiu YQ. Theoretical investigation on switchable second-order nonlinear optical (NLO) properties of novel cyclopentadienylcobalt linear [4]phenylene complexes. J Mol Model. 2013; 19(4): 1779–87.
32. Do H, Besley NA. Structural optimization of molecular clusters with density functional theory combined with basin hopping. J Chem Phys. 2012; 137(13): 134106-1–9.
33. Zhang C, Bevan DR, Barone JR. Molecular Design and Mechanistic Characterization of Glycoside Hydrolases using Computational and Experimental Techniques. Somayesadat Badieyan; 2012.
34. De Souza GLC, de Oliveira LMF, Vicari RG, Brown A. A DFT investigation on the structural and antioxidant properties of new isolated interglycosidic O-(1 → 3) linkage flavonols. J Mol Model. 2016; 22(4).
35. Kosar B, Albayrak C. Spectroscopic investigations and quantum chemical computational study of (E)-4-methoxy-2-[(p-tolylimino)methyl]phenol. Spectrochim Acta Part A Mol Biomol Spectrosc. 2011; 78(1): 160–7.
36. Tamafo Fouegue AD, Ghogomu JN, Desire Bikele M, Nkungli NK, Younang E. Structural and Antioxidant Properties of Compounds

●btained from Fe2+Chelation by Juglone and Two of Its Derivatives: DFT, ●TAIM, and NB● Studies. Bioinorg Chem Appl. 2●16; 2●16(6): 1–13.

37. Adevailton Bernardo dos S, Silva DHS, Bolzani V da S, Santos LA, Schmidt TM, Baffa ●. Antioxidant properties of plant extracts: An EPR and DFT comparative study of the reaction with DPPH, TEMP●L and spin trap DMP●. J Braz Chem Soc. 2●●9; 2●(8): 1483–92.
38. Ghammamy S, Yousefi F. Structural properties,theory functional calculations (dft), natural bond orbital and energies for the n-(3-chloro-1h- indazol-5-yl)-4-methoxybenzenesulfonamide. 2●14; 1(1): 26–34.
39. Temel E, Alaşalvar C, Gökçe H, Güder A, Albayrak Ç, Alpaslan YB, et al. DFT calculations, spectroscopy and antioxidant activity studies on (E)-2-nitro-4-[(phenylimino)methyl]phenol. Spectrochim Acta—Part A Mol Biomol Spectrosc. 2●15; 136(PB): 534–46.
40. Li Y-N, Wang J-●, He L-N, Yang Z-Z, Liu A-H, Yu B, et al. Experimental and theoretical studies on imidazolium ionic liquid-promoted conversion of fructose to 5-hydroxymethylfurfural. Green Chem. 2●12; 14(1●): 2752.
41. Bayden A. Computational Chemistry, ●verview. ACS Div Comput Chem.
42. J. Williams, P. Stang PS. Physical ●rganic Chemistry: ●uantitative Conformational Analysis; Calculation Methods. Ann Rev Phys Chem. 1●68; 1●.
43. Buckingham RA. The Classical Equation of State of Gaseous Helium, Neon and Argon. Proc R Soc Lond A Math Phys Sci. 1●38; 168: 264–283.
44. Mason EA. Transport Properties of Gases ●beying a Modified Buckingham (Exp-Six) Potential. J Chem Phys. 1●54; 22: 16●–86.
45. Lung Wa Chung, W. M. C. Sameera, Romain Ramozzi, Alister J. Page, Miho Hatanaka, Galina P. Petrova, Travis V. Harris, Xin Li, Zhuofeng Ke, Fengyi Liu, Hai-Bei Li, Lina Ding and KM. The ●NI●M Method and Its Applications. Chem Rev. 2●15; 115(12): 5678–796.
46. Frisch MJ, Trucks GW, Schlegel HB, Scuseria GE, Robb MA, J.R. C, et al. GAUSSIAN ●9 (Revision A.2) Gaussian, Inc., Wallingford, CT,. D J Gaussian ●9. 1●98; B.●1; (Gaussian, Inc.:).
47. Bolton EE, Wang Y, Thiessen PA, Bryant SH. PubChem: integrated platform of small molecules and biological activities,.

Vol. 4, Annual Reports in Computational Chemistry. 2008.
48. O'Boyle NM, Banck M, James CA, Morley C, Vandermeersch T, Hutchison GR. Open Babel: An open chemical toolbox. J Chem Informatics. 2011; 3:33.
49. Wang X. An Introduction to Basis Set and ONIOM Technique. East Tennessee State University; 2012.
50. Tabti C, Benhalima N. Molecular Structure, Vibrational Assignments and Non-Linear Optical Properties of by DFT and ab Initio HF Calculations. Adv Mater Phys Chem. 2015; 5(July): 221–8.
51. Safna Hussan KP, Mohamed Shahin T, Deshpande SK, Jinitha T V, Vijisha KR, Ngai KL. Synthesis and molecular dynamics of double active pharmaceutical ingredient-benzalkonium ibuprofenate. J Mol Liq. 2016; 223: 1333–9.
52. Expanding the limits of computational chemistry [Internet]. 2018. Available from: http://gaussian.com/freq/.
53. Singh BN, Aliot E. Newer antiarrhythmic agents for maintaining sinus rhythm in atrial fibrillation: Simplicity or complexity? Eur Hear Journal, Suppl. 2007; 9(G): 17–25.
54. Md. Tanweer Alam and Rituraj KK Srivastava S. Theoretical studies on the site reactivity of picric acid. Int J Innov Appl Res. 2004; 2(1): 19–34.
55. Kar R, Chandrakumar KRS, Pal S. The Influence of Electric Field on the Global and Local Reactivity Descriptors: Reactivity and Stability of Weakly Bonded Complexes. J Phys Chem A. 2007; 111: 375–83.
56. Young DC. Computational chemistry: a practical guide for applying techniques to real-world problems. Vol. 9. 2001. 1–370 p.
57. KK Srivastava, ShubhaSrivastava, Tanweer Alam M, Rituraj. Theoretical studies on the site reactivity of picric acid. ISSN 2348–0319 Int J Innov Appl Res. 2014; 2(1): 19–34.
58. Sadasivam K, Kumaresan R. Antioxidant behavior of meamsetin and myricetin flavonoid compounds—A DFT study. Spectrochim Acta Part A Mol Biomol Spectrosc. 2011; 79(1): 282–93.
59. Vijisha KR, Muraleedharan K. A computational investigation on the structure, global parameters and antioxidant capacity of a polyphenol, Gallic acid. Food Chem. 2017; 220: 93–9.
60. Xavier S, Periandy S, Carthigayan K, Sebastian S. Molecular docking, TG/DTA, molecular structure, harmonic vibrational frequencies, natural bond orbital and TD-DFT analysis of diphenyl carbonate by DFT approach. J Mol Struct. 2016; 1125: 204–16.

61. Bahadur I, Momin MIK, Koorbanally NA, Sattari M, Ebenso EE, Katata-Seru LM, et al. Interactions of polyvinylpyrrolidone with imidazolium based ionic liquids: Spectroscopic and Density Functional Theory studies. J Mol Liq. 2016; 213(January): 13–6.
62. Bobo C, Jiuyao D, Shuangyue L, Xiao Z, Xuejun S, Haitao, Sun. Hui F. Carbon dioxide capture by amino-functionalized ionic liquids: DFT based theoretical analysis substantiated by FT-IR investigation. RSC Adv. 2016; 6: 10462–70.
63. Bobo C, Jiuyao D, Dongmei D, Haitao S, Xiao Z, Hui F. Cellobiose as a model system to reveal cellulose dissolution mechanism in acetate-based ionic liquids : Density functional theory study substantiated by NMR spectra. Carbohydr Polym. 2016; 149: 348–56.
64. Safna Hussan KP, Mohamed Shahin T, Deshpande SK, Jinitha TV, Jayant K. Development of ion conducting ionic liquid-based gel polymer electrolyte membrane PMMA/BMPyr.TFSI—With improved electrical, optical, thermal and structural properties. Solid State Ionics. 2017; 310: 166–75.
65. Safna Hussan KP, Mohamed Shahin Thayyil, SK Deshpande JT V. Photoluminescent behavior of propylene carbonate and poly (methylmethacrylate) blend for transparent optoelectronic devices. 2017; 02012: 02012.
66. Sangeetha KG, Aravindakshan KK, Safna Hussan KP. Insight into the theoretical and experimental studies of 1-phenyl-3-methyl-4-benzoyl-5-pyrazolone N(4)-methyl-N(4)-phenylthiosemicarbazone—A potential NLO material. J Mol Struct. 2017 Dec; 1150: 135–45.
67. Wazzan NA, Al-Qurashi OS, Faidallah HM. DFT/ and TD-DFT/PCM calculations of molecular structure, spectroscopic characterization, NLO and NBO analyses of 4-(4-chlorophenyl) and 4-[4-(dimethylamino) phenyl]-2-oxo-1,2,5,6-tetrahydrobenzo[h]quinoline-3-carbonitrile dyes. J Mol Liq. 2016; 223: 29–47.
68. Attia G, El-kader MFHA. Structural, Optical and Thermal Characterization of PVA / 2HEC Polyblend Films. Int J Electrochem Sci. 2013; 8: 5672–87.
69. Bonzanini R, Dias DT, Girotto EM, Muniz EC, Baesso ML, Caiut JMA, et al. Spectroscopic properties of polycarbonate and poly(methyl methacrylate) blends doped with europium (III) acetylacetonate. J Lumin. 2006; 117(1): 61–7.
70. Lunstroot K, Driesen K, Nockemann P, Viau L, Mutin PH, Vioux

A, et al. Ionic liquid as plasticizer for europium(III)-doped luminescent poly(methyl methacrylate) film. Phys Chem Chem Phys. 2010; 12(8): 1879–85.

71. Liu HG, Lee YI, Park S, Jang K, Kim SS. Photoluminescent behaviors of several kinds of europium ternary complexes doped in PMMA. J Lumin. 2004; 110(1–2): 11–6.
72. Bonzanini R, Girotto EM, Gonçalves MC, Radovanovic E, Muniz EC, Rubira AF. Effects of europium (III) acetylacetonate doping on the miscibility and photoluminescent properties of polycarbonate and poly(methyl methacrylate) blends. Polym J. 2005; 46(1): 253–9.
73. Tanak H, Pawlus K, Marchewka MK. Molecular structure, vibrational spectra and DFT computational studies of melaminium N-acetylglycinate dihydrate. J Mol Struct. 2016; 1121: 142–55.
74. Scanning Electron Microscope [Internet]. Available from: https://en.wikipedia.org/wiki/Scanning_electron_microscope.
75. Gemini SEM [Internet]. Available from: https://www.google.com/imgres?imgurl=https%3A%2F%2Fwww.zeiss.com%2Fcontent%2Fdam%2FMicroscopy%2FProducts%2Felectron-microscopes%2FGemini%2520SEM%2Fgemini_objective_lens.png&imgrefurl=https%3A%2F%2Fwww.zeiss.com%2Fmicroscopy%2Fint%2Fproducts%2Fscanning-electron-microscopes%2Fgeminisem.html&docid=pKLyl8-Er8o3eM&tbnid=bK-yp9BR_QDyWM%3A&vet=10ahUKEwjdxqDq9rzfAhUIpo8KHZNnDo4QMwg-KAAwAA..i&w=562&h=700&bih=626&biw=1366&q=sem gemini 30 schematic diagram&ved=0ahUKEwjdxqDq9rzfAhUIpo8KHZNnDo4QMwg-KAAwAA&iact=mrc&uact=8.
76. Li Z, Deen MJ, Kumar S SP. Raman spectroscopy for in-line water quality monitoring—instrumentation and potential. Sensors. 2014.
77. Guirguis OW, Moselhey MTH. Thermal and structural studies of poly (vinyl alcohol) and hydroxypropyl cellulose blends. Nat Sci. 2012; 4(1): 57–67.
78. Safna Hussan KP, Thayyil MS, Jinitha T V., Kolte J. Development of an ionogel membrane PVA/[EMIM] [SCN] with enhanced thermal stability and ionic conductivity for electrochemical application. J Mol Liq. 2019; 274: 402–13.
79. Chapter III Molecular Structure Analysis by FT-IR, FT-Raman and

FT-NMR.
80. Attenuated_total_reflectance [Internet]. Available from: https://en.wikipedia.org/wiki/Attenuated_total_reflectance.
81. El-Sayed S, Mahmoud KH, Fatah AA, Hassen A. DSC, TGA and dielectric properties of carboxymethyl cellulose/polyvinyl alcohol blends. Phys B Condens Matter. 2011; 406(21): 4068–76.
82. Satterwhite J. Differential scanning calorimetry [Internet]. 2019. Available from: https://www.pinterest.com/pin/492018328016708610/.
83. Agrawal SL, Awadhia A. DSC and conductivity studies on PVA based proton conducting gel electrolytes. Bull Mater Sci. 2004; 27(6): 523–7.
84. Saroj AL, Singh RK. Thermal, dielectric and conductivity studies on PVA / Ionic liquid [EMIM] [EtSO 4] based polymer electrolytes. J Phys Chem Solids. 2012; 73(2): 162–8.
85. Liew C, Ramesh S, Arof AK. Characterization of ionic liquid added poly(vinyl alcohol)-based proton conducting polymer electrolytes and electrochemical studies on the supercapacitors. Int J Hydrogen Energy. 2014; 40(1): 852–62.
86. Çavuş S, Durgun E. Poly(vinyl alcohol)-based polymer gel electrolytes: Investigation on their conductivity and characterization. Acta Phys Pol A. 2016; 129(4): 621–4.
87. Brostow W, Chiu R, Kalogeras IM, Vassilikou-Dova A. Prediction of glass transition temperatures: Binary blends and copolymers. Mater Lett. 2008; 62(17–18): 3152–5.
88. Flory TGFPJ. The glass temperature and related properties of polystyrene. Influence of molecular weight. J Polym Sci barmer. 1954.
89. Gordon, M.; Taylor J. Ideal copolymers and the second-order transitions of synthetic rubbers. J Appl Chem. 1952; 2:493–500.
90. Couchman, PR; Karasz FE. A classical thermodynamic discussion of the effect of composition on glass transition temperatures. Macromolecules. 1978; 11: 117–9.
91. Suknuntha K, Jones DS, Tantishaiyakul V. Properties of felodipine-poly(vinylpyrrolidone) solid dispersion films and the impact of solvents. ScienceAsia. 2012; 38(2): 188–95.
92. Couchman PR KF. A classical thermodynamic discussion of the effect of composition on glass-transition temperatures. Macromolecules. 1978; 11(9): 117.
93. Jenkel, E.; Heusch R. Die Erniedrigung der Einfriertemperatur organischer Glaser durch Losungsmittel. Colloid. Polym Sci. 1953;

130: 89–105.
94. Kwei T. The effect of hydrogen bonding on the glass transiton temperature of polymer mixtures. J Polym Sci. 1984; 22: 307–13.
95. Barkoula NM, Alcock B, Cabrera NO, Peijs T. Fatigue properties of highly oriented polypropylene tapes and all-polypropylene composites. Polym Polym Compos. 2008; 16(2): 101–13.
96. Turnkey Broadband Dielectric/Impedance Spectrometers [Internet]. Novocontrol Technologies 2018. Available from: https://www.novocontrol.de/php/index.php.
97. National AV, National IMK. Dielectric analysis (DEA). 2017.
98. Joncher AK. The "universal" dielectric response. Nature. 1977; 256: 673.
99. Hodge IM, Ngai KL, Moynihan CT. Comments on the electric modulus function. J Non Cryst Solids. 2005; 351(2): 104–15.
100. Köhler M, Lunkenheimer P, Loidl A. Dielectric and conductivity relaxation in mixtures of glycerol with LiCl. Eur Phys J E. 2008; 27(2): 115–22.
101. Ahmed RM. Electrical Conductivity and Dielectric Relaxation Study of Polyvinyl Acetate/Poly Methyl Methacrylate Blends. Int J Mod Phys B. 2012; 26(29): 1250159.
102. Schro K, Reissig S, Hempel E, Beiner M. From small molecules to polymers : Relaxation behavior of n-butyl methacrylate based systems. 2007.
103. Günther Hartwig DE. Noometallic Materials and Composites at Low Temperatures 2. 1st ed. A. F. Clark, R. P. Reed and GH, editor. Plenum Press; 1982.
104. Sangoro JR, Serghei A, Naumov S, Galvosas P, Kärger J, Wespe C, et al. Charge transport and mass transport in imidazolium-based ionic liquids. Phys Rev E—Stat Nonlinear, Soft Matter Phys. 2008; 77(5): 4–7.
105. Rivera A, Blochowicz T, Gainaru C, Rössler EA. Spectral response from modulus time domain data of disordered materials. J Appl Phys. 2004; 96(10): 5607.
106. Wojnarowska Z, Swiety-Pospiech A, Grzybowska K, Hawelek L, Paluch M, Ngai KL. Fundamentals of ionic conductivity relaxation gained from study of procaine hydrochloride and procainamide hydrochloride at ambient and elevated pressure. J Chem Phys. 2012; 136(16).
107. Colby R. Dynamic scaling approach to glass formation. Phys Rev E Stat Phys Plasmas Fluids Relat Interdiscip Topics. 2000; 61(2): 1783–92.

108. Wojnarowska Z, Paluch M, Grzybowski A, Adrjanowicz K, Grzybowska K, Kaminski K, et al. Study of molecular dynamics of pharmaceutically important protic ionic liquid-verapamil hydrochloride. I. Test of thermodynamic scaling. J Chem Phys. 2009; 131(10): 104505–14.
109. Kumar NSK, Shahid TS, Govindaraj G. Analysis of conductivity and dielectric spectra of Mn0.5Zn0.5Fe2O4 with coupled Cole–Cole type anomalous relaxations. Phys B Condens Matter. 2016; 488: 99–107.
110. Jakobsen B, Niss K, Olsen NB. Dielectric and shear mechanical alpha and beta relaxations in seven glass-forming liquids. J Chem Phys. 2005; 123(23): 1–9.
111. Kremer F, Schönhals A. Broadband Dielectric Spectroscopy. Springer. 2003.
112. Richert R. The dielectric modulus: relaxation versus retardation. Solid State Ionics. 1998; 105(1–4): 167–73.
113. Macedo PB, Moynihan CT, Bose R. The Role of Ionic Diffusion in Polarization in Vitreous Ionic Conductors. Phys Chem Glas. 1972; 13: 171–9.
114. Jadhav N, Gaikwad V, Nair K, Kadam H. Glass transition temperature: Basics and application in pharmaceutical sector. Asian J Pharm. 2009; 3(2): 82.
115. Jarosz G, Mierzwa M, Zioło J, Paluch M, Shirota H, Ngai KL. Glass transition dynamics of room-temperature ionic liquid 1-methyl-3-trimethylsilylmethylimidazolium tetrafluoroborate. J Phys Chem B. 2011; 115(44): 12709–16.
116. Rivera A, Rössler EA. Evidence of secondary relaxations in the dielectric spectra of ionic liquids. Phys Rev B—Condens Matter Mater Phys. 2006; 73(21): 1–4.
117. Dam T, Karan NK, Thomas R, Pradhan DK, Katiyar RS. Observation of ionic transport and ion-coordinated segmental motions in composite (polymer-salt-clay) solid polymer electrolyte. Ionics (Kiel). 2014; 21(2): 401–10.
118. Adrjanowicz K, Kaminski K, Paluch M, Wlodarczyk P, Grzybowska K, Wojnarowska Z, et al. Dielectric relaxation studies and dissolution behavior of amorphous verapamil hydrochloride. J Pharm Sci. 2010; 99(2): 828–39.
119. Agrebi F, Ghorbel N, Ladhar A, Bresson S, Kallel A. Enhanced dielectric properties induced by loading cellulosic nanowhiskers in natural rubber: Modeling and analysis of electrode polarization. Mater Chem Phys. 2017; 200(June): 155–63.

120. Ye Y-S, Tseng C-Y, Shen W-C, Wang J-S, Chen K-J, Cheng M-Y, et al. A new graphene-modified protic ionic liquid-based composite membrane for solid polymer electrolytes. J Mater Chem. 2011; 21(28): 10448.
121. Johari GP, Andersson O. On the nonlinear variation of dc conductivity with dielectric relaxation time. J Chem Phys. 2006; 125(12).
122. Jarosz G, Mierzwa M, Zioło J, Paluch M, Shirota H, Ngai KL. Glass transition dynamics of room-temperature ionic liquid 1-methyl-3-trimethylsilylmethylimidazolium tetrafluoroborate. J Phys Chem B. 2011; 115(44): 12709–16.
123. Tuskaev VA, Gagieva SC, Kurmaev DA, Zubkevich SV, Kolosov NA, Bulychev BM, et al. Novel titanium(IV) complexes stabilized by 2-hydroxybenzyl alcohol derivatives as catalysts for UHMWPE production. Journal of Organometallic Chemistry. 2018.
124. Aidoud D, Etiemble A, Guy-Bouyssou D, Maire E, Le Bideau J, Guyomard D, et al. Interfacial stability and electrochemical behavior of Li/LiFePO4 batteries using novel soft and weakly adhesive photo-ionogel electrolytes. J Power Sources. 2016; 330: 92–103.
125. Safna Hussan KP, Mohamed Shahin T, Binesh M, Deshpande SK, K. Rajan V. Molecular dynamics in amorphous pharmaceutically important protic ionic liquid–benzalkonium chloride. J Mol Liq. 2017; 251: 487–91.
126. Rivera A, Santamaría J, León C, Blochowicz T, Gainaru C, Rössler E. Temperature dependence of the ionic conductivity in Li[sub 3x]La[sub 2/3−x]TiO[sub 3]: Arrhenius versus non-Arrhenius. Appl Phys Lett. 2003; 82(15): 2425.
127. Pimenov A, Lunkenheimer P, Rall H, Kohlhaas R, Loidl A, Böhmer R. Ion transport in the fragile glass former 3KNO3-2Ca(NO3)2. Phys Rev E. 1996; 54(1): 676–84.
128. Oh J, Seo J, Kook H, Hwang Y. The secondary relaxation in the dielectric loss of glucose—water mixtures. J Non Cryst Solids. 2006; 352: 4679–84.
129. Minoguchi A, Kaneko T, Sotokawa H, Nozaki R. Dielectric relaxation processes in supercooled polyhydric alcohols and their mixtures. J Non Cryst Solids. 2006; 352(42–49 SPEC. ISS.): 4742–5.
130. Kubo E, Minoguchi A, Sotokawa H, Nozaki R. Nearly constant dielectric loss of polyhydric alcohols. J Non Cryst Solids. 2006; 352(42–49 SPEC. ISS.): 4724–8.

131. Kaminska E, Kaminski K, Hensel-Bielowka S, Paluch M, Ngai KL. Characterization and identification of the nature of two different kinds of secondary relaxation in one glass-former. J Non Cryst Solids. 2006; 352(42–49 SPEC. ISS.): 4672–8.
132. Capaccioli S, Kessairi K, Prevosto D, Lucchesi M, Ngai KL. Genuine Johari-Goldstein β-relaxations in glass-forming binary mixtures. J Non Cryst Solids. 2006; 352(42–49 SPEC. ISS.): 4643–8.
133. Ngai KL, Capaccioli S, NS, Thayyil MS. Recent progress in understanding relaxation in complex systems. J Non Cryst Solids. 2010; 356(11–17): 535–41.
134. Prevosto D, Capaccioli S, Rolla PA, Paluch M, Pawlus S, Hensel-Bielowka S, et al. Secondary dielectric relaxation in decahydroisoquinoline-cyclohexane mixture. J Non Cryst Solids. 2006; 352(42–49 SPEC. ISS.): 4685–9.
135. Hayashi Y, Puzenko A, Feldman Y. Slow and fast dynamics in glycerol–water mixtures. J Non Cryst Solids. 2006; 352(August): 4696–703.
136. Habasaki J, Ngai KL. Molecular dynamics simulation of ion dynamics in glassy ionic conductors: Evidence of the primitive ion hopping process. J Non Cryst Solids. 2006; 352(42–49 SPEC. ISS.): 5170–7.
137. Ngai KL, Capaccioli S, Shinyashiki N, Thayyil MS. Recent progress in understanding relaxation in complex systems. J Non Cryst Solids. 2010; 356(11–17): 535–41.
138. Sanz A. Complex nature of the b relaxation and fragility in aromatic polyesters. J Non Cryst Solids. 2007; 353: 3989–95.
139. Rosner P, Samwer K, Lunkenheimer P. Indications for an excess wing in metallic glasses from the mechanical loss modulus in Zr65A17.5Cu27.5. Europhys Lett. 2004; 68(2): 226–32.
140. Papathanassiou AN. Electric properties of carbon nano-onion/polyaniline composites: a combined electric modulus and ac conductivity study. In p. 1–23.
141. Liu J, Duan CG, Yin WG, Mei WN, Smith RW, Hardy JR. Dielectric permittivity and electric modulus in Bi2Ti4O11. J Chem Phys. 2003; 119(5): 2812–9.
142. Wehn R, Lunkenheimer P, Loidl A. Broadband dielectric spectroscopy and aging of glass formers. J Non Cryst Solids. 2007; 353(41–43): 3862–70.
143. Ngai KL. Johari-Goldstein relaxation as the origin of the excess wing observed in metallic glasses. J Non Cryst Solids. 2006;

352(5): 404–8.
144. Jakobsen B, Maggi C, Christensen T, Dyre JC. Investigation of the shear-mechanical and dielectric relaxation processes in two monoalcohols close to the glass transition. J Chem Phys. 2008; 129(18).
145. Psarras GC, Gatos KG, Karahaliou PK, Georga SN, Krontiras CA. Relaxation phenomena in rubber / layered silicate nanocomposites. eXPRESS Polym Lett. 2007; 1(12): 837–45.
146. Kannan Kottummal T, Pilathottathil S, Thayyil MS, Mahadevan Perumal P, Nagarajan Sreekala KK, Guruswamy G, et al. Dielectric relaxation and electrochemical studies on trihexyl tetradecyl phosphonium chloride [P14,6,6,6][Cl] ionic liquid. J Mol Liq. 2018; 252: 488–94.
147. Sangoro J, Iacob C, Serghei A, Naumov S, Galvosas P, Sangoro J, et al. Electrical conductivity and translational diffusion in the 1-butyl-3- methylimidazolium tetrafluoroborate ionic liquid. J Chem Phys. 2008; 128(214509): 1–5.
148. Narendar N, Mather GC, Dias PAN, Fagg DP. The importance of phase purity in Ni-BaZr0.85Y0.15O3- novel nitrate-free combustion route and electrochemical study. RSC Adv. 2013; 3(3): 859–69.
149. Tafur JP, Fernández Romero AJ. Electrical and spectroscopic characterization of PVdF-HFP and TFSI-ionic liquids-based gel polymer electrolyte membranes. Influence of ZnTf2 salt. J Memb Sci. 2014; 469(1): 499–506.
150. Powles JG. Cole–Cole Plots as they should be. J Mol Liq. 1993; 56(2): 3–7.
151. Ahad N, Saion E, Gharibshahi E. Structural, thermal, and electrical properties of PVA-sodium salicylate solid composite polymer electrolyte. J Nanomater. 2012; 2012: 1–8.
152. Muralidharan P. Synthesis, characterization and transport studies of lithium based superionic conductors for solid state battery applications. In 2010.
153. Cheruku R, Govindaraj G, Vijayan L. Super-linear frequency dependence of ac conductivity in nanocrystalline lithium ferrite. Mater Chem Phys. 2014; 146(3): 389–98.
154. Hemalatha KS, Sriprakash G, Prasad MVNA, Damle R, Rukmani K. Temperature dependent dielectric and conductivity studies of polyvinyl alcohol-ZnO nanocomposite films by impedance spectroscopy. J Appl Phys. 2015; 118(154103): 1–14.
155. Merle G, Hosseiny SS, Wessling M, Nijmeijer K. New cross-linked

PVA based polymer electrolyte membranes for alkaline fuel cells. J Memb Sci. 2012; 409–10: 191–9.
156. Liew C-W, Ramesh S, Arof AK. A novel approach on ionic liquid-based poly(vinyl alcohol) proton conductive polymer electrolytes for fuel cell applications. Int J Hydrogen Energy. 2014; 39(6): 2917–28.
157. Seok Jang H, Justin Raj C, Lee W-G, Chul Kim B, Hyun Yu K. Enhanced supercapacitive performances of functionalized activated carbon in novel gel polymer electrolytes with ionic liquid redox-mediated poly(vinyl alcohol)/phosphoric acid. RSC Adv. 2016; 6(79): 75376–83.
158. Sathish S, Shekar BC. Preparation and characterization of nano scale PMMA thin films. Indian J Pure Appl Phys. 2014; 52(January): 64–7.
159. Zein El Abedin S, Ryder KS, Höfft O, Farag HK. Ionic Liquids: Potential Electrolytes for Electrochemical Applications. Int J Electrochem. 2012; 2012: 1–2.
160. Watanabe M, Thomas ML, Zhang S, Ueno K, Yasuda T, Dokko K. Application of Ionic Liquids to Energy Storage and Conversion Materials and Devices. Chem Rev. 2017; 117(10): 7190–239.
161. Introduction to Capacitors [Internet]. Available from: https://www.electronics-tutorials.ws/capacitor/cap_1.html.
162. Pandey GP, Kumar Y, Hashmi SA. Ionic liquid incorporated polymer electrolytes for supercapacitor application. Indian J Chem—Sect A Inorganic, Phys Theor Anal Chem. 2010; 49(5–6): 743–51.
163. Li G, Miao P. Theoretical Background of Electrochemical Analysis. In: Electrochemical Analysis of Proteins and Cells. 2013. pp. 5–18.
164. Organization WM. Wmo Greenhouse Gas Bulletin. 2017.
165. Burying the problem. Canadian Geographic Magazine.
166. Carbon capture and storage [Internet]. Available from: https://en.wikipedia.org/wiki/Carbon_capture_and_storage#cite_note-4.
167. Metz, B, O Davidson, HC de Coninck, M Loos and LAM. IPCC special report on Carbon Dioxide Capture and Storage. Prepared by working group III of the Intergovernmental Panel on Climate Change. Cambridge University Press, Cambridge.
168. Wang S, Li X, Wu H, Tian Z, Xin Q, He G, et al. Advances in high permeability polymer-based membrane materials for CO 2 separations. Energy Environ Sci. 2016; 9(6): 1863–90.

169. Gainaru C, Stacy EW, Bocharova V, Gobet M, Holt AP, Saito T, et al. Mechanism of conductivity relaxation in liquid and polymeric electrolytes: Direct link between conductivity and diffusivity. J Phys Chem B. 2016; 120(42): 11074–83.
170. Kar GP, Biswas S, Bose S. Simultaneous enhancement in mechanical strength, electrical conductivity, and electromagnetic shielding properties in PVDF-ABS blends containing PMMA wrapped multiwall carbon nanotubes. Phys Chem Chem Phys. 2015; 17(22): 14856–65.
171. Chaban V. The thiocyanate anion is a primary driver of carbon dioxide capture by ionic liquids. Chem Phys Lett. 2015; 618: 89–93.
172. Song D, Xu C, Chen Y, He J, Zhao Y, Li P, et al. Enhanced thermal and electrochemical properties of PVDF-HFP/PMMA polymer electrolyte by TiO2 nanoparticles. Solid State Ionics. 2015; 282: 31–6.
173. Shalu, V.K. Singh, Singh RK. Development of ion conducting polymer gel electrolyte membranes based on polymer PVdF-HFP, BMIMTFSI ionic liquid and the Li-salt with improved electrical, thermal and structural properties. J Mater Chem C. 2015; 3(28): 7305–18.
174. Fuller J, Breda AC, Carlin RT. Ionic liquid-polymer gel electrolytes. J Electrochem Soc. 1997; 144(4): L67–70.
175. Chiang C, Tsai K, Lee Y, Lin H, Yang Y, Shih C, et al. Microelectronic Engineering in situ fabrication of conducting polymer composite film as a chemical resistive CO 2 gas sensor. Microelectron Eng. 2013; 111: 409–15.
176. Hatika Kaaco, Sarani Zakaria, Chin Hua Chia LZ. com Transparent and Printable Regenerated Kenaf Cellulose/PVA Film. J Bioresour. 2014; 9(1999): 2167–78.
177. El-kader KAMA, Hamied SFA. Preparation of Poly(vinyl alcohol) Films with Promising Polyethylen e Film. J Appl Polym Sci. 2002; 86: 1219–1226.
178. Gunaid MQA Al, Saeed AMN, Subramani NK, Siddaramaiah BSM. Optical parameters , electrical permittivity and I –V characteristics of PVA / Cs 2 CuO 2 nanocomposite films for opto-electronic applications. J Mater Sci Mater Electron. 2017; 28(11): 8074–86.
179. Chemwiki UCD, Alike CCA, License US. Photoluminescence Spectroscopy 10.6: Photoluminescence Spectroscopy. In pp. 1–16. Available from:

https://chem.libretexts.org/Textbook_Maps/Analytical_Chemistry_Textbook_Maps/Map%3A_Analytical_Chemistry_2.0_(Harvey)/10_Spectroscopic_Methods/10.6%3A_Photoluminescence_Spectroscopy.